UNIVERSITEIT VAN PRETORIA
UNIVERSITY OF PRETORIA
YUNIBESITHI YA PRETORIA

Development of a vibration isolation system for a rotary wing unmanned aerial vehicle

by

Gerardus Franciscus Knijnenburg

submitted in fulfilment of the requirements for the degree

MEng (Mechanical Engineering)

in the Faculty of Engineering, Built Environment and Information Technology

University of Pretoria

Pretoria

July 2017

Development of a vibration isolation system for a rotary wing unmanned aerial vehicle

by

Gerardus Franciscus Knijnenburg

Supervisor : Prof. NJ Theron

Department : Mechanical and Aeronautical Engineering

Degree : MEng

Abstract

Antiresonance vibration isolation has long been a well known, studied and applied method for alleviating vibrations in stiff structures where small static deflection and a low transmissibility is needed, making it ideal for use in the rotor-craft industry. Most prior arts focus on passive single frequency antiresonance vibration isolation, while some, most notably liquid inertia vibration isolators, are adapted to actively isolate vibrations at more than one frequency. Very little literature is found on the adaptation of mechanical pendulum antiresonance vibration isolators for in-flight tunable multiple frequency isolation, and although these systems predate the more modern liquid inertia type isolator, there is merit in their further development and use as low cost, robust and low maintenance isolators. A feasibility study on the performance of changing each fundamental design variable to achieve antiresonance tuning concludes, that for the antiresonance frequency shift range of interest in this dissertation, no specific design variable change quantifiably outperforms another with respect to tuning the antiresonance. Concept designs are created and investigated, finding the superior method of tuning the vibration isolator based on other criteria like overall weight, design simplicity, practicality, robustness and reliability. Shifting the tuning mass on the pendulum arm is deemed to be the superior concept, with respect to the helicopter being developed, and a tunable multi-frequency pendulum antiresonance vibration isolation system with a sliding concentrated mass is developed with ADAMS multi-body dynamics software and SolidWorks. The isolation system along with a full scale dummy fuselage and transmission-rotor assembly is manufactured and experimentally tested. Initial experimental results show antiresonance frequencies $10Hz$ higher than the design targets, this phenomenon is later discovered to be related to friction in the pin joints of the pendulum hinges, increasing the system overall stiffness. Needle roller bearings are inserted to eliminate the friction, and experimental and ADAMS model results are again compared showing good correlation, with experimental results isolating close to the three target frequencies within 3% error. An astonishing level of vibration isolation is observed with the largest transmissibility obtained at the three frequencies being 0.5%. This dissertation proves the concept of a tunable mechanical pendulum vibration isolator, and its design methodology, particularly with respect to shifting the position of the tuning mass. Suggestions for further work are: to implement this system with an actuation mechanism, further research on the effects of friction in isolators and the use of said phenomenon as a tuning method, development of isolators implementing the other concept of changing the design variables and a comparison between the effect of normal damping and friction damping on vibration isolation.

Acknowledgements

I would like to thank:

- Prof NJ Theron for his guidance
- Mr. G Breintenbach for his help around the test facility
- Mr. H Booysen for his help with the instrumentation
- My family and wife for their unwavering love and support
- All the staff at the C-AIM labs for their help with the experiments

Contents

List of Figures

List of Tables

Nomenclature

$\bar{x}$	A vector of design variables
ω_a	Antiresonance frequency of system configuration a
ω_b	Antiresonance frequency of system configuration b
a	Front and rear concrete block side length
b	Left and right concrete block side length
c	Bottom concrete block side length
CG	Center of gravity
$F(\bar{x})$	A function of the design variable vector $\bar{x}$
F_I, F_L	Inertial reaction force
F_K	Spring reaction force
F_x	Vibration force in the x-direction
F_y	Vibration force in the y-direction
F_z	Vibration force in the z-direction
I_{FX}	Fuselage mass moment of inertia around the roll axis
I_{FY}	Fuselage mass moment of inertia around the pitch axis
I_{HX}	Rotor mast mass moment of inertia around the roll axis
I_{HY}	Rotor mast mass moment of inertia around the pitch axis
K, K_D	Absorber spring stiffness
$K_{\theta X}$	Torsional spring stiffness between the rotor mast and the fuselage about the x-axis
$K_{\theta Y}$	Torsional spring stiffness between the rotor mast and the fuselage about the y-axis
K_a	Isolator stiffness of system configuration a
K_B	Vertical stiffness at pendulum hinge B
K_b	Isolator stiffness of system configuration b
K_D	Second harmonic sub system spring stiffness
K_E	Vertical diaphragm plate stiffness
K_M	Pressurizing-spring stiffness
L_{AB}	Distance between pendulum hinge A and B
L_{EF}	Vertical diistance between the vibration isolation deck and the fuselage center of gravity

L_{EG} Vertical distance between the vibration isolation deck and the rotor hub

L_{EH} Vertical diistance between the vibration isolation deck and the rotor mast center of gravity

L_m Distance between the pendulum hinge and the pendulum concentrated mass

L_p Distance between the pendulum hinge and the pendulum arm center of mass

$m1$ Floating mass number one

$m2$ Floating mass number two

$m3$ Floating mass number three

m_2, M_D Tuning mass

m_a Tuning mass of system configuration a

m_b Tuning mass of system configuration b

M_C First harmonic tuning mass

M_D Second harmonic tuning mass

M_F Fuselage mass

M_H Rotor mast and hub assembly mass

m_m Pendulum concentrated mass

m_p Pendulum arm mass

m_t Pendulum total mass

N Number of rotor blades

pN p^{th} multiple of rotor blade quantity

Q_{R1} Pendulum arm ratio of system configuration 1 or a

Q_{R2} Pendulum arm ratio of system configuration 2 or b

Q_{Rh1} Pendulum arm length ratio for first harmonic mass

Q_{Rh2} Pendulum arm length ratio for second harmonic mass

Q_R Pendulum arm ratio, ratio of total pendulum length (R) and length between pendulum hinges (r)

R Distance between first pendulum arm hinge to pendulum center of gravity

r Distance between pendulum arm hinges

R_a System configuration a distance from first hinge to pendulum center of gravity

r_a System configuration a distance between pendulum hinges

R_b System configuration b distance from first hinge to pendulum center of gravity

r_b System configuration b distance between pendulum hinges

R_f Antiresonance frequency ratio of system configuration b to a

R_K Ratio of isolator stiffness in system a to system b

R_{mf} Mass fraction of pendulum concentrated mass to the total pendulum mass

R_m Mass ratio of system configuration b to system configuration a

R_Q Ratio of pendulum arm ratios of system configuration 1 to 2

R_R Ratio of pendulum arm length of system configuration a to b

R_r Ratio of distance between pendulum hinges of system configuration a to b

rev Revolution

S_N The nth scalar value

x Forward facing beam length

x_O Distance from the start of the hydraulic piston to the hydraulic liquid center of mass

x_T Distance from the start of the hydraulic piston to the center of mass of the entire hydralic cylinder and piston assembly

x_W Distance from the start of the hydraulic piston to the center of mass of the piston

y Sideways facing beam length

z Downwards facing beam length

Mx Moment around the roll axis

My Moment around the pitch axis

List of Abbreviations

VIS : Vibration Isolation System

FEA : Finite Element Analysis

FEM : Finite Element Model

VIA : Vibration Isolation Assembly

ARVIS : Anti-Resonance Vibration Isolation System

IRIS : Improved Rotor Isolation System

DAVI : Dynamic Antiresonance Vibration Isolator

LIVE : Liquid Inertia Vibration Eliminator

TVAI : Tunable Vibration Absorbing Isolator

DOF : Degrees of Freedom

ADAMS : Automatic Dynamic Analysis of Mechanical Systems

1 Introduction

Conventionally helicopters are designed to have a single primary rotor speed where thrust is generated by changing the angle of attack of the rotor blades to the airflow and not by varying rotor speed. The fuselage is excited by the rotor blades primarily at a single blade passing frequency and harmonics thereof, their vibration isolators are designed for attenuation at only the main blade passing frequency.

The objective of this dissertation is to develop a vibration isolator for a rotary wing unmanned aerial vehicle that can isolate a minimum of three distinct main rotor blade excitation frequencies, where the slowest and fastest rotor speed excitations are spaced 10% around a mean rotor speed. The need for an in-flight tunable isolator stems from the concept of the mentioned rotor-craft having three distinct rotor speeds instead of just the conventional single primary rotor speed of most helicopters. Studies done by the developer of the helicopter shows a theoretical increase in the flight range and fuel efficiency, as different rotor speeds are more efficient at delivering the required thrust at different forward flight speeds. The slowest rotor speed also has practical use as a "stealth" mode during surveillance, where the rotors generate considerably less noise than when the rotor speed is running at maximum speed for optimal power and flight manoeuvrability.

Helicopters have long been plagued by excessive vibration forces generated by dynamic and asymmetric aerodynamic effects on the rotor blades during forward flight. A stiff suspension, with small static deflection, between the rotor-transmission assembly and the fuselage is desired for optimal control and flight dynamics, whilst the transmission of vibrations or transmissibility is desired to be as low as possible. In conventional vibration absorber theory these objectives are conflicting, as small static deflection calls for a high stiffness system whilst low transmissibility calls for a low stiffness system. However, if the excitation is deterministic and at a single frequency the principles of antiresonance can be applied, where the system is tuned to have an antiresonance at the specific excitation frequency, theoretically completely isolating the suspended body from the vibrations of the excited body whilst allowing stiff coupling between them. The deterministic single frequency vibration characteristics of conventional helicopters lend themselves to the use of antiresonance vibration isolators for attenuation of cyclic loads.

A literature review covering some fundamental concepts of vibration, sources of helicopter vibrations and existing concepts, patents, designs and implementations of known antiresonance vibration isolators, show that the concept is well understood, and especially widely used in the rotor-craft industry. Apart from the underlining principles and concepts, the literature review has a sharp focus on the mechanical design of the different implementations as to conclude which base concept best lends itself to the needs of the rotor-craft that is the subject of this dissertation.

On conclusion of the literature review, a feasibility study on the performance of altering each fundamental design variable of the chosen base system concludes that for the antiresonance frequency shift range of interest in this dissertation, no specific design variable change quantifiably outperforms another with respect to tuning the antiresonance.

Therefore, finding the superior method of tuning the vibration isolator becomes a more complex exercise encompassing the consideration of many other criteria like overall weight, design simplicity, practicality, robustness, and reliability to name but a few. Concept designs for the different methods of tuning the vibration isolator are created, discussed and scrutinised on the bases of the mentioned criteria. A single design concept is chosen that is developed further for this dissertation.

Chapter 5 focuses on the design and fabrication of the first and second prototypes of the chosen design, with focus on using inexpensive and readily available materials and resources.

After the design and fabrication of the prototypes, the experimental setup and test procedures are discussed after which a multi-body dynamics ADAMS model of the experiment is created. The experimental results are compared to the analytical results of the ADAMS simulations, and their correlation discussed and concluded. The first prototype fuselage adversely affected the test frequency range with unexpected low frequency dynamics ,prompting

the design and development of a simpler second prototype fuselage. Photographic images are used at the end of the experimental evaluation chapter showing visual confirmation of vibration isolation.

Lastly the experimental results and the dissertation as a whole is concluded with recommendations for future work, followed by the Appendices.

2 Literature study

2.1 Vibration principles

2.1.1 Resonance

Resonance is the natural phenomenon which occurs when an external force excites a system at one of its natural frequencies, causing large and violent oscillations. Resonance is seldom desired in any system, more so on helicopters, as stresses caused by resonance quickly exceed the low safety-factor design imposed on aerial vehicles.

2.1.2 Antiresonance

Antiresonance is as much a natural phenomenon as resonance, and as the name suggests has qualities opposite to that of resonance. At an anti-resonant frequency a system or subsystems shows no motion at one or more points in the structure.

Both resonance and antiresonance are location specific phenomenon, at any given excitation frequency there might be resonances and antiresonances simultaneously depending on the location being observed. Therefore, it is important to distinguish between two types of antiresonances, driving point- and transfer antiresonance. Driving point antiresonance occurs at the excitation point and transfer antiresonance occurs at any location other than the excitation point.[17]

Some of the oldest anti-resonant systems are based on driving point antiresonance, whilst more modern systems, dating from the 60's, are based on transfer antiresonance.[17]

2.2 Sources of helicopter vibrations

Vibrations in helicopters come from many sources like the engine, drivetrain, transmission and fuselage aerodynamic effects to name but a few, and although these sources of vibration are important for helicopter design, the focus of this dissertation is the alleviation of the cyclic vibrations coming from the main rotor. In steady-state forward flight, helicopter vibration predominantly consist of periodic responses to periodic forces at the rotor blade root caused by rotor blade dynamic and aerodynamic interaction with the environment. Helicopters in general operate at a single rotor speed making the vibrations deterministic and harmonic in nature, the two main excitation frequencies experienced in helicopters are the $1/rev$ and N/rev vibrations, where N is the number of rotor blades on the main rotor. The $1/rev$ vibrations come from mass or aerodynamic unbalance between rotor blades and the N/rev excitations come predominantly from aerodynamic interaction of the rotor blades during forward flight.

One of the main causes of the cyclic loading on the blade roots are due to the asymmetric aerodynamic loading of the rotor blades during forward flight. During forward flight half of rotor blades, at any given instance, are moving against the motion of the air moving relative to the helicopter, whilst the other half are moving in the same direction as the relative air motion. This causes the blades on the one half of the rotor, at a specific time, to have much larger lift and drag forces than blades on the opposing side, and as the blade then transitions from moving against the relative air flow to moving with it, so do the applicable forces. This is the predominant driving force behind the N/rev vibration excitation, as each blade transitions this change in aerodynamic loading within a single rotation of the rotor blades.

Table 1 shows the type and frequency of vibration in the non-rotating frame (the fuselage) and how the rotating frame (the rotor blade assembly) causes said vibrations. As each rotor blade generates varying thrust, depending on its relative motion to that of the air flow during a revolution, causes a thrust vibration at the N/rev frequency.

Nonrotating Frame		Rotating Frame
thrust at pN/rev	from	vertical shear at pN/rev
torque at pN/rev	from	lagwise moment at pN/rev
rotor drag and side forces at pN/rev	from	in-plane shears at $pN \pm 1$/rev
pitch and roll moments at pN/rev	from	flapwise moment at $pN \pm 1$/rev
collective control system forces at pN/rev	from	feathering moments at pN/rev
cyclic control system forces at pN/rev	from	feathering moments at $pN \pm 1$/rev

Table 1: Vibrations in the fuselage and their sources[15, pp. 696]

Furthermore, as rotor blades rotate through a revolution they transition from a high drag or lag-wise moment to a lower drag or lead-wise moment as they transition from high wind loading to low wind loading, causing torsional vibrations at the N/rev frequency. Drag and side forces are caused by the unbalance of the rotor blades with a $1/rev$ frequency and also in planes shears at the N/rev frequency. As rotor blades generate more lift, and as a result flex more, during half of it cycle in comparison to the other half generates a flapping motion of the blades which in turn generates pitch and roll moments on the non-rotating frame. Lastly, feathering moment from the control system cause varying cyclic and collective pitch forces as the control system actuates the angle of attack of each blade to the wind flow.[15, pp. 694-698]

2.3 Antiresonance vibration isolation systems

Two seemingly conflicting design ideologies are at hand when developing helicopter structures, the first being small static displacements for payloads which is indicative of designing stiff structures with high natural resonance frequencies, the other is that of small response or transmissibility to vibration loading which is indicative of low stiffness structures with low natural frequencies. Both goals can be met when the payloads are attached to nodal points of high stiffness structures, this ensures small responses to vibration excitation, whilst ensuring a stiff small deflection under static loading. This is the appeal of antiresonance vibration isolators, the systems can be stiff whilst delivering a low transmissibility.

2.3.1 Focal point isolation system

The Focal Isolation System was the first concept of an antiresonance vibration isolation system, developed in the 1960's this system uses pin joint kinematic linkages directed at a desired focal axis to create an antiresonance for vibrations in that axis.[1] Elastomeric and/or metal mounts are used between the fuselage and transmission-rotor assembly for the required spring back forces. Figure 1 shows a diagram of the focused pylon isolation system, "focusing" links with spherical bearings are attached to the transmission at such an angle that their projections intersect the centre of gravity of the rotor and transmission which is also the focal point.

Figure 2 shows an illustration of such a focus pylon system used on the Bell 206/OH-58 military helicopter. Notice how projection of the focal bi-pods intersect the roll axis of the helicopter whilst the transmission to focal bi-pod interfaces intersects the pitch axis of the helicopter, shown in the bottom right of Figure 2. The kinematic links are

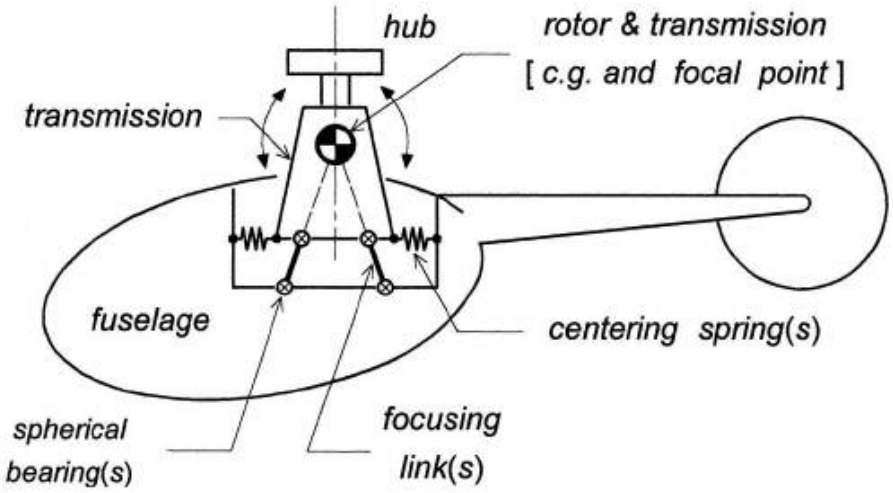

Figure 1: Diagram of a focused pylon vibration isolator[3, pp. 270]

spherical bearings that cannot transfer moments, and because they intersect the the pitch and roll axes, no cyclic pitch and roll moments can be transmitted to the fuselage, except those coming from other mounts between the fuselage and transmission.[3]

Focal Pylon systems permit the rigid transfer of thrust forces whilst isolating angular pitch and roll excitation to in-plane shears. Figure 3 shows the theoretical angular frequency response of a helicopter with a up focused Focus Pylon Isolation System. Perfect rotational isolation is theoretically obtained at the 2/rev frequency, which for a two rotor helicopter is the main blade passing frequency. Compared to the finite angular rigid body response , shown in dashed lines, the fuselage response is zero with the Focus Pylon Isolator which shows remarkable performance.

The focus pylon isolation system only eliminates vibratory moments, but transmits vibratory shears, which are known to form a large part of overall helicopter vibration. Therefore, other concepts were developed to alleviate vibratory shear loading.

2.3.2 Fuselage nodalization

Methods for determining in-flight fuselage nodal points by Kidd, et al. in 1970 paved the way for structural analysis and design of helicopter fuselages with nodal points deliberately placed at key locations within the structure, mainly the cabin area. With respect to large cabin areas this method is ineffective as large parts of the cabin is far removed from the designed nodal point, and might be prone to large vibration excitations. Furthermore, nodal points may shift with changing in-flight loading conditions further hampering the effectiveness of this system as the nodal points might shift away from the area of interest. Figure 4 shows the application of such a system on the Bell UH-1C and AH-1G helicopters.

One way of working around these problems would be to completely suspend the payloads from in flight nodal points, any changes to the payloads will not effect the natural frequencies of the fuselage as they are attached to static or zero response points during vibration. A patent submitted by Jan Drees[14] describes and illustrates the concept of fuselage nodalization, see Figure 5. The dashed lines labelled A and B are the mode shapes of the transmission and rotor supporting structure at the first blade passing frequency, with points labelled 41 and 40 being nodal points of this mode of vibration. The mentioned supporting structure is attached to the rest of the helicopter fuselage, at points 42 and 43, which correspond to nodal points of the supporting structure.

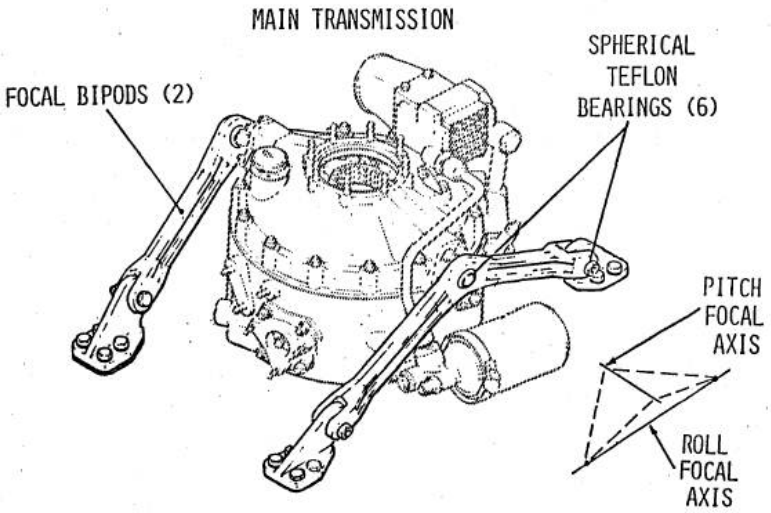

Figure 2: Illustration of 206/OH-58 focus pylon[1, pp. 59]

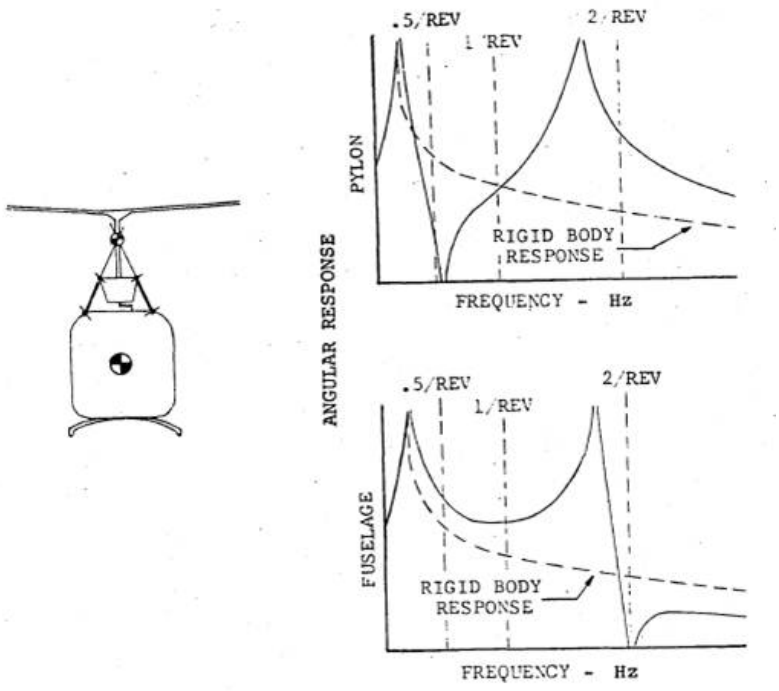

Figure 3: Focal pylon isolation system frequency response [1, pp. 54]

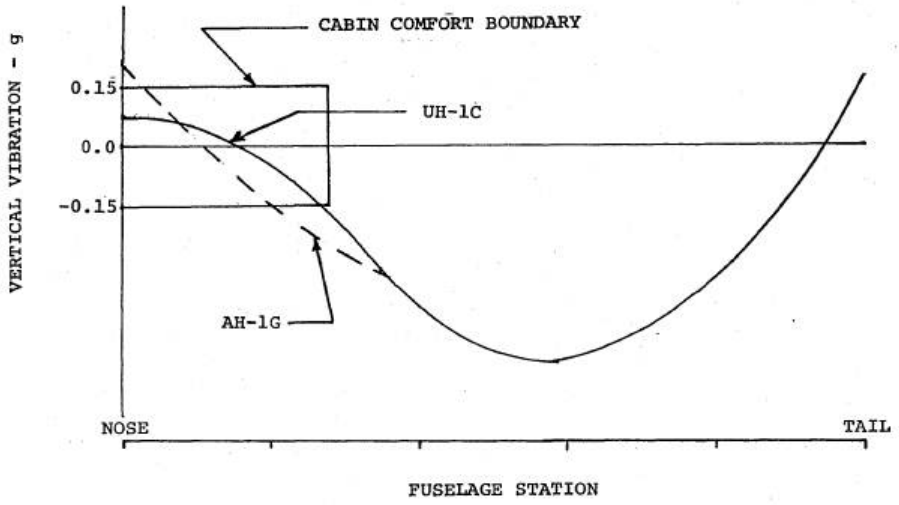

Figure 4: Fuselage modalization application[1, pp. 57]

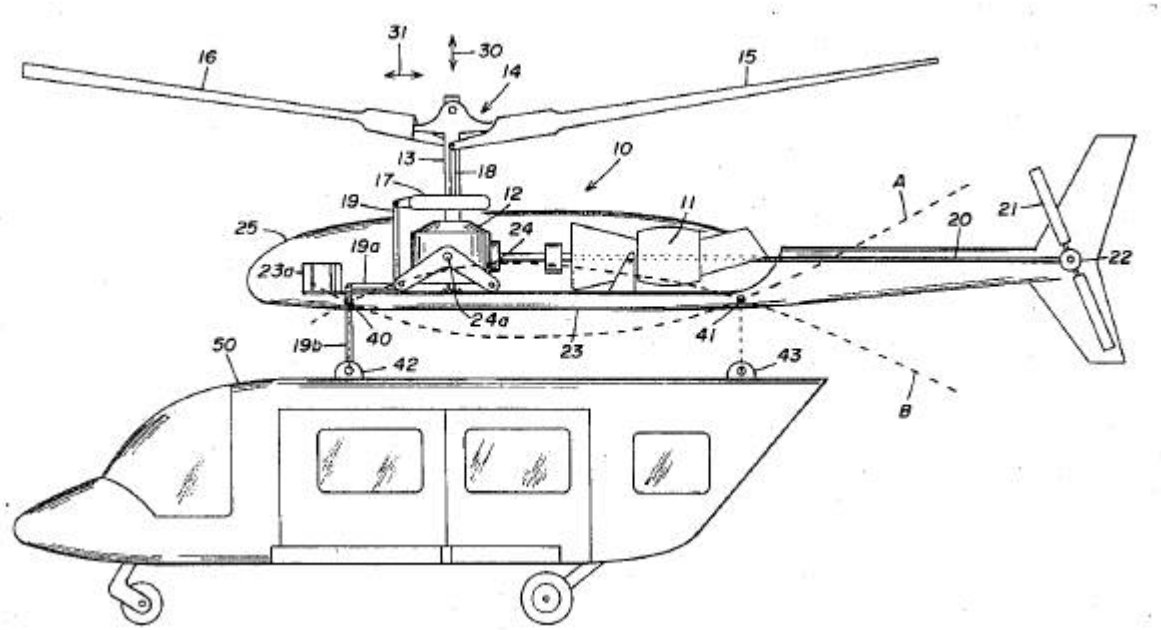

Figure 5: Fuselage nodalization[14]

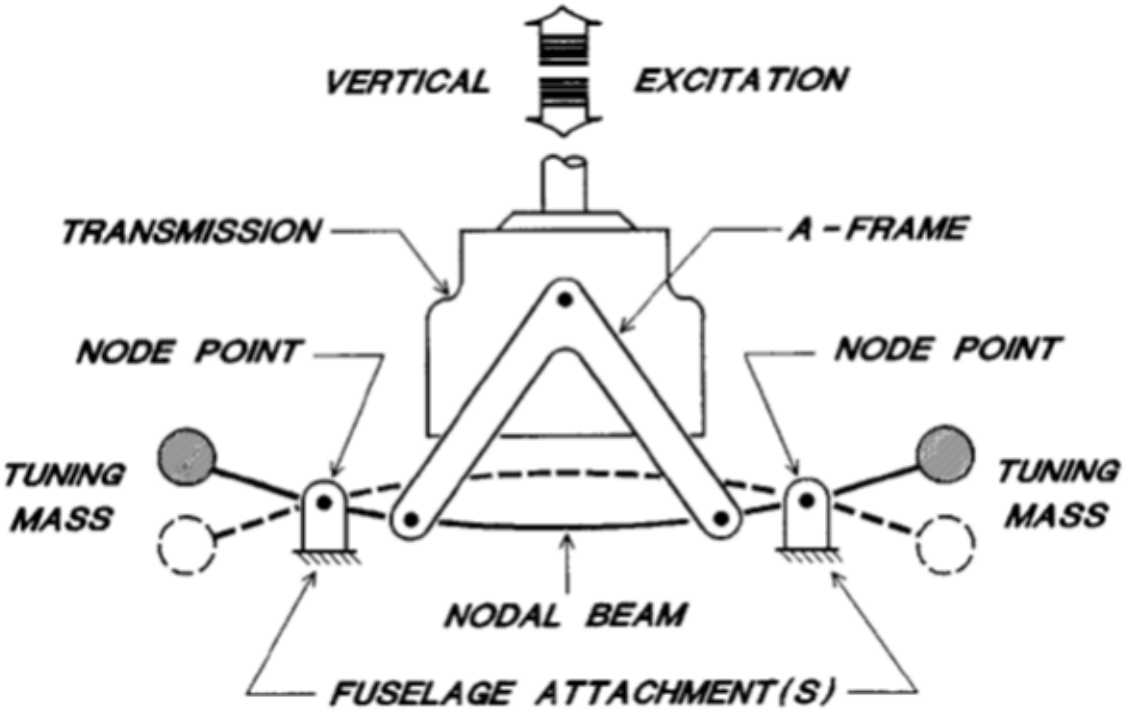

Figure 6: Nodamatic isolation system[3, pp.266]

The advantage of nodalization mounting in comparison to conventional soft mounting is that high structural stiffness is obtained whilst having low transmissibility.

2.3.3 Nodal point isolation

Fuselage nodalization discussed in Section 2.3.2 requires expensive and time consuming structural analysis to determine where the nodal points are. Because the majority of the excitations come from the rotor, the next logical step is to apply nodalization to the suspension mounts of the transmission-rotor assembly, nodal points location can easily be controlled through design without the need for structural analysis[14]. The transmission-rotor assembly is attached to a nodal beam that is itself attached to the fuselage at nodal points on the beam. Tuning masses are usually required to force the structure to have nodal points at the desired attachment locations.

Figure 6 shows an illustration of a nodal point isolation system developed by Bell Helicopter called the Nodamatic isolation system. This system works on the principle that the reaction forces at the nodes (locations of zero motion during vibration) of the beam, vibrating at the excitation frequency, are significantly reduced. An example of such a system on an existing helicopter can be seen in Figure 7, this system is actually a combined focal- (Section 2.3.1) and nodal point isolation system.

This quite simple and relatively effective vibration isolation system is known to be relatively heavy [3, pp. 265] and bulky, as is evident in Figure 7.

2.3.4 Dynamic Antiresonance Vibration Isolator

One of the first antiresonance vibration isolation systems is the Dynamic Antiresonance Vibration Isolator or DAVI for short, first reported on in 1966[9] and patented in 1967 by William G Flannelly[10], the fuselage and

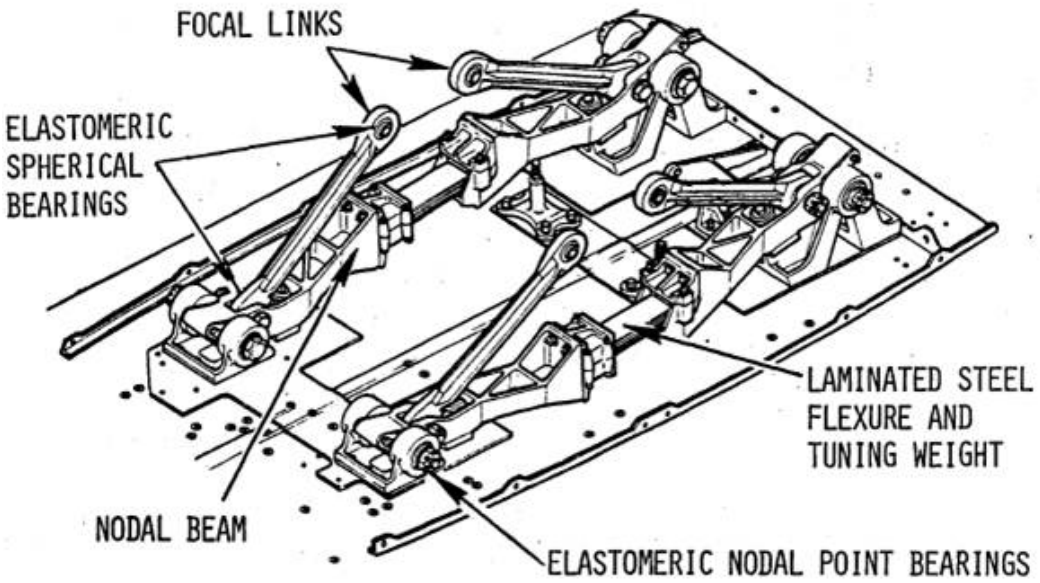

Figure 7: Nodal beam Isolators on the Bell 206l helicopter[1, pp. 59]

transmission-rotor assembly is connected by a spring and also by a pendulum with a tuning mass at the end.

Figure 8 shows the fundamental principles of such a system utilizing a nodal beam or pendulum. The system is designed that the inertial force is of equal magnitude but opposite phase to that of the spring force F_K at a specific excitation frequency of interest, theoretically completely cancelling the vibration excitation forces. The inertial force magnitude and phase is tuned by choosing the correct values of the lengths R, r and tuning mass m_2. The DAVI shown in Figure 8 can only alleviate vibrations in the vertical axis, which for a helicopter would be the heave direction. Flannelly designed and patents a three dimensional DAVI in 1971[11] that functions on the same principles of the original DAVI but alleviates vibrations in all three directions. Shown in Figure 9 is a schematic of the three dimensional DAVI, two pendulums are required to inertially counteract vibrations in all three directions. Vibrations F_x and F_y are counteracted by the vertical pendulum (shown as number30) because ball joints (shown as numbers 38 and 36) allow the vertical pendulum to pivot in both the XZ and YX planes, F_z vibrations are counteracted by the horizontal pendulum (shown as number29).

Throughout the aerospace industries countless DAVI or DAVI-like systems are designed and sometimes implemented. Desjardins, R.A., & Sankewitsch patent various DAVI type devices to isolate, seats, fuel tanks and helicopter floors from vibrations of the helicopter fuselage[7]. This shows that total rotor vibration isolation is not the only practical solution for antiresonance vibration isolators, and that the principle can be applied wherever isolation is required. However, isolating the entire fuselage from rotor induced vibrations does seem more cost effective than isolating individual sub systems. Localised vibration isolation does have merit on existing systems where redesigning the transmission-rotor to fuselage interface is impractical but isolation is sought on a specific subsystem.

2.3.5 Improved Rotor Isolation System

The Improved Rotor Isolation System or IRIS for short is somewhat of a combination of the DAVI and the Nodamatic vibration isolation systems. Figure 10 shows a schematic of the IRIS system, with a flexure beam with tuning

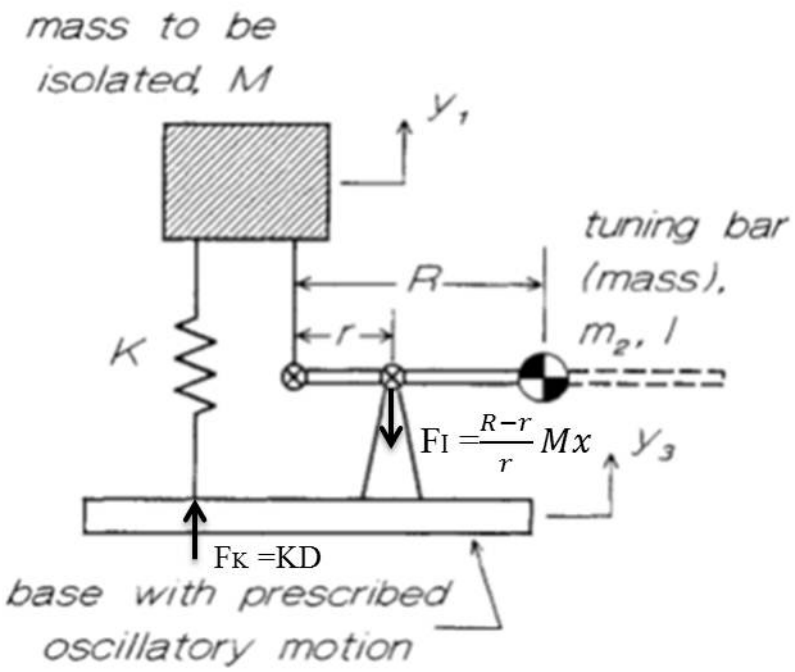

Figure 8: DAVI[3, pp. 267]

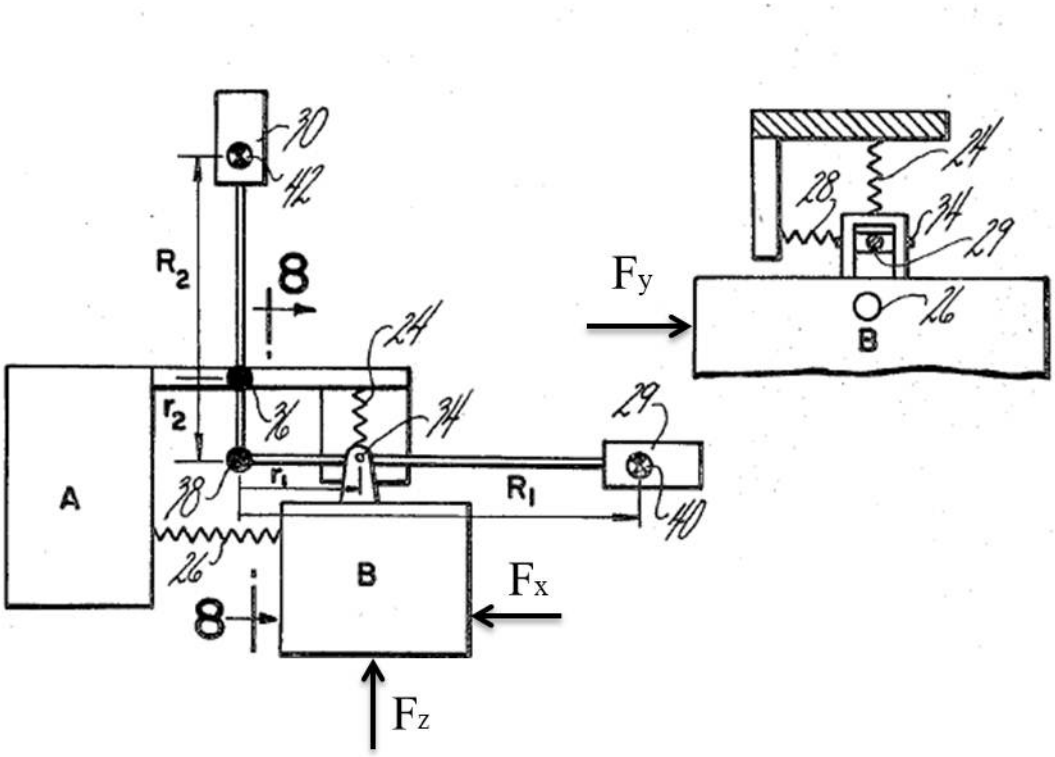

Figure 9: Three dimensional DAVI[11]

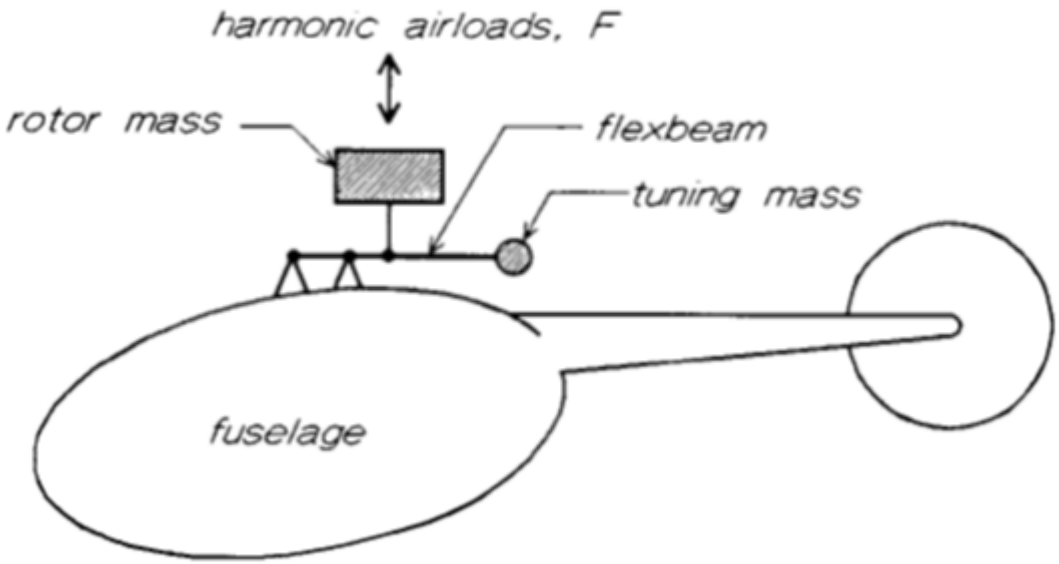

Figure 10: IRIS[3, pp. 269]

mass that doubles as the nodal isolation structure and an inertial compensating mass. IRIS has antiresonance characteristics similar to that of the DAVI without the need for low damping bearings, however, the IRIS also suffers from the weight penalties of a heavy and bulky nodal beam structure much like the Nodamatic system.[3, pp. 268]

The concept and invention is patented in 1978 by Rene A. Desjardins,Charles W. Ellis and Vladimir Sankewitsch with the basic design shown in Figure 11[6]. Because the modern, more refined, and implemented design is discussed later in this section, the patent concept will not be discussed further as it works on the same principles.

Shown in Figure 12 is a six axis installation of the IRIS system on the Messerschmitt-Bölkow-Blohm BO-105 light helicopter, as previously discussed this system does seem quite bulky and as a result heavy. Figure 13 shows a section view of a bidirectional IRIS isolator, to alleviate confusion the bottom of Figure 13 has a diagrammatic representation of the core functions of the IRIS unit.

The bell shaped pendulum and mass encloses the nodal beam structure that attaches the transmission-rotor assembly to the fuselage. Although the IRIS is heavier than the DAVI with similar weight penalties to that of the Nodamatic vibration isolator it has one unique advantage above the other systems, the IRIS is inherently bidirectional. Because there are no ball or hinge joints the nodal beam and pendulum are free to pivot in any direction and alleviate vibrations in all 6 degrees of freedom. This is advantageous because the Nodamatic vibration isolator only alleviate vibrations in vertical shear and angular vibrations for pitch and roll whilst the simple DAVI isolates only vertical shear vibrations.

2.3.6 Liquid Inertia Vibration Eliminator

The Liquid Inertia Vibration Eliminator or LIVE for short was developed by Dennis R. Halwes and William A. Simmons and patented in 1980 [12]. This novel vibration isolator works on the same inertial counteracting principles of the DAVI , but instead of a tuning mass on a pendulum, the inertial counteracting force is generated by displacing an inertial liquid from one chamber to another through a narrowing or “tuning tube”.

Figure 14 shows a diagram of how the LIVE system works, a tuning tube is attached to one of the two bodies between which vibration is to be eliminated. This tuning tube is attached between two chambers that are in turn

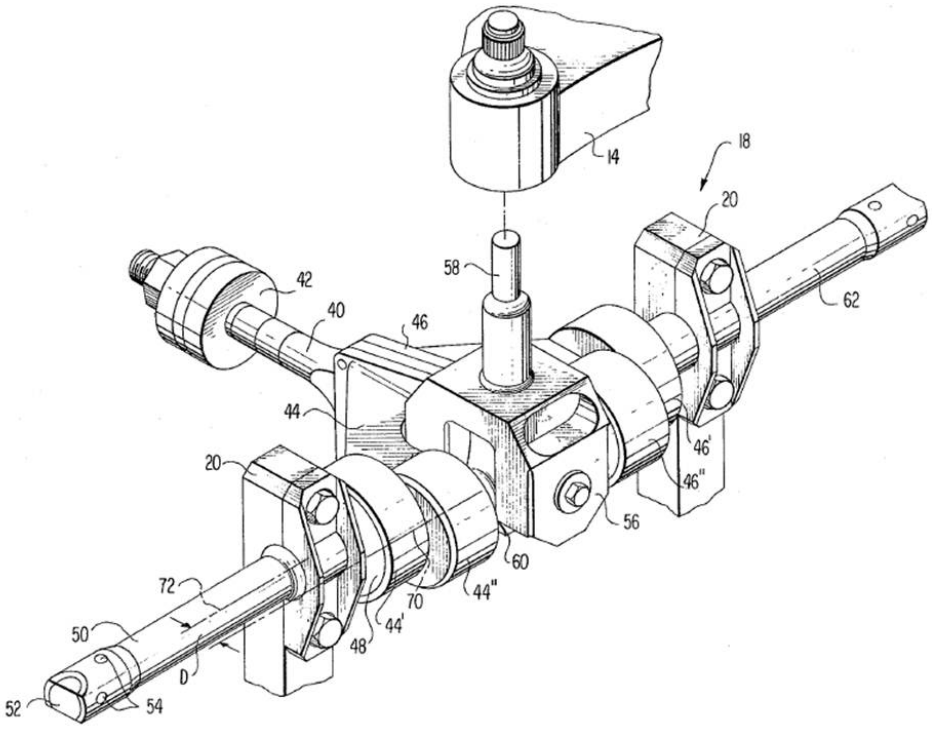

Figure 11: Improved Rotor Isolation System original patent[6]

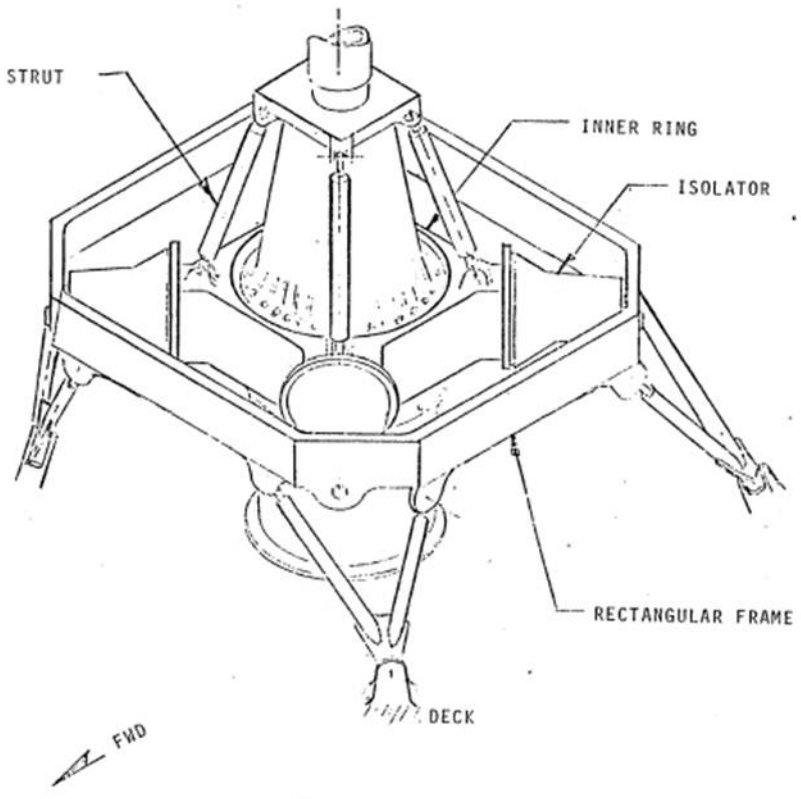

Figure 12: Six axis IRIS installation on BO-105[18, pp. 58]

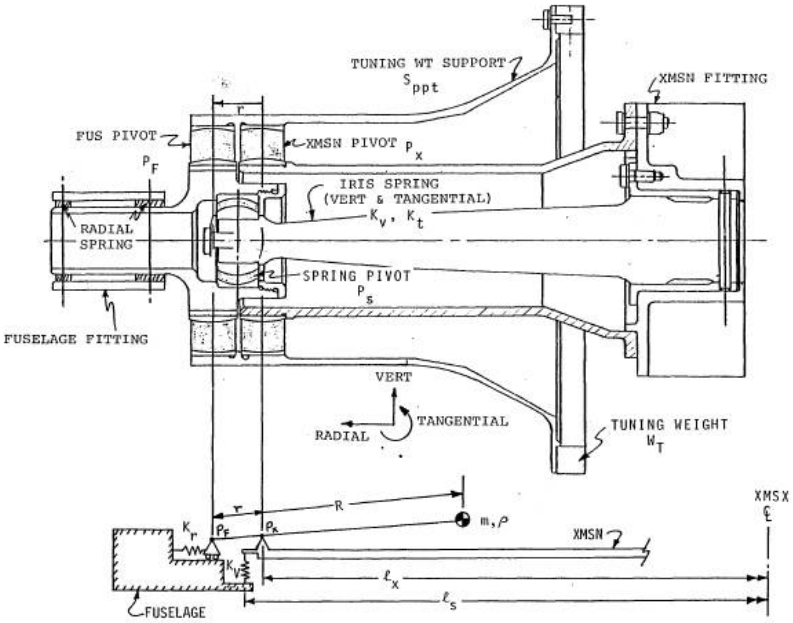

Figure 13: Bidirectional IRIS unit[18, pp. 60]

attached to the other body. The chambers are able to increase or decrease their respective volumes if the tuning tube is displaced, a spring between the bodies acts as a restoring force.

During a vibratory force input the tuning tube is forced into one direction contracting one chamber whilst expanding another, this contraction and expansion of the chambers pumps the inertial liquid from one to the other creating a inertial force F_L. By choosing the correct length, tuning tube neck diameter and the initial sizes of the chambers, this inertial force can be "tuned" to have the same magnitude but opposite phase to that of the spring reaction force F_K, effectively cancelling the vibration force.

The original invention shown in Figure 15 is physically very similar to the diagram shown in Figure 14 except that an elastomeric spring (number 32 in the figure) encased in an outer housing (18) functions as both the spring and the chambers (42 and 40) of the LIVE system. An incompressible high density low viscosity high surface tension liquid is recommended and ideal for the use in LIVE devices, liquid mercury or even slurries comprising of metallic shavings and hydraulic fluid are suitable candidates for the inertial liquid mass[12]. Mercury is highly corrosive and also toxic, making the use of slurries a much safer and environmentally friendly alternative but comes at the cost of having a much larger LIVE unit.

Even though a single LIVE unit only alleviates vibration in a single direction Halwes implements a total rotor isolation LIVE system comprising of a multitude of LIVE units configured in different axes connecting the transmission-rotor assembly to the fuselage, see Figure 16. Halwes reports an above 95% vibration isolation for all rotational and shear responses to rotor shears and moments.

2.3.7 Hydraulic "pendulum" vibration isolator

In 1982 D. Braun of the Messerschmitt-Bölkow-Blohm aerospace industry developed a antiresonance vibration isolation system that works on the same principles of the DAVI (see Section 2.3.4), but instead of a pendulum arm, a hydraulic "pendulum" is used[4]. Figure 17 shows a diagram of such a system, unlike the pendulum of DAVI this method utilizes two bellows, one large and one small, to create a hydraulic "pendulum" for inertial force generation.

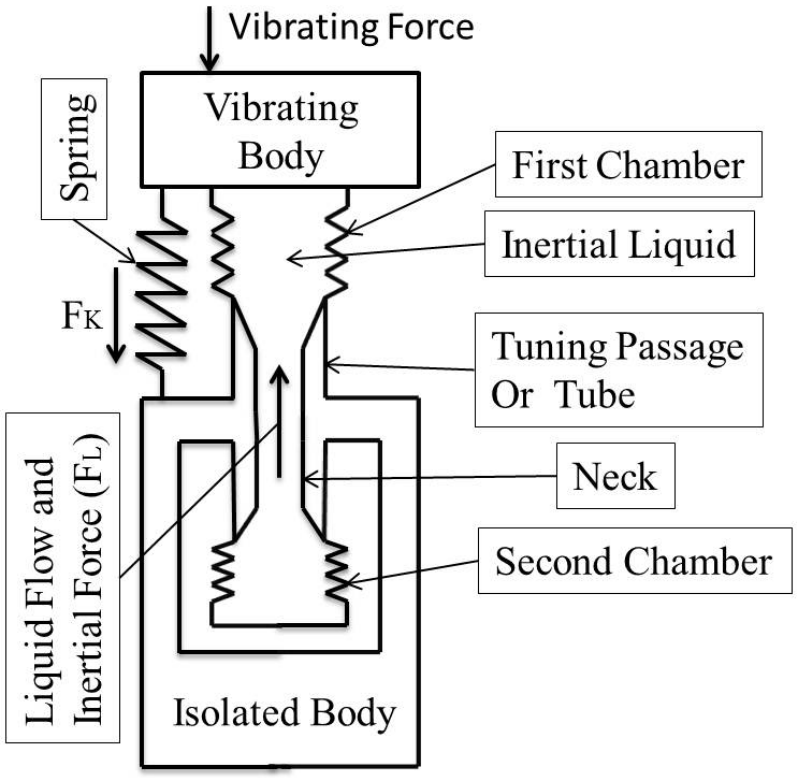

Figure 14: Liquid Inertia Vibration Eliminator diagram

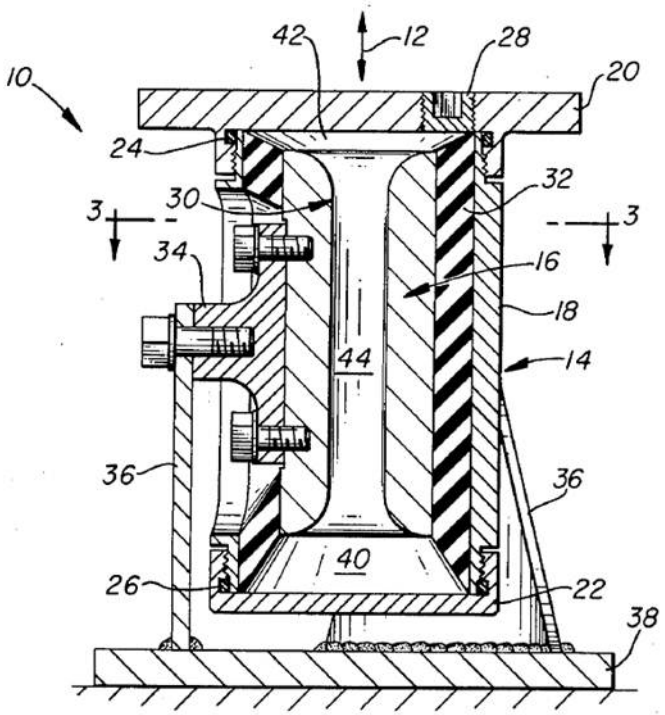

Figure 15: Liquid Inertia Vibration Eliminator patent diagram[12]

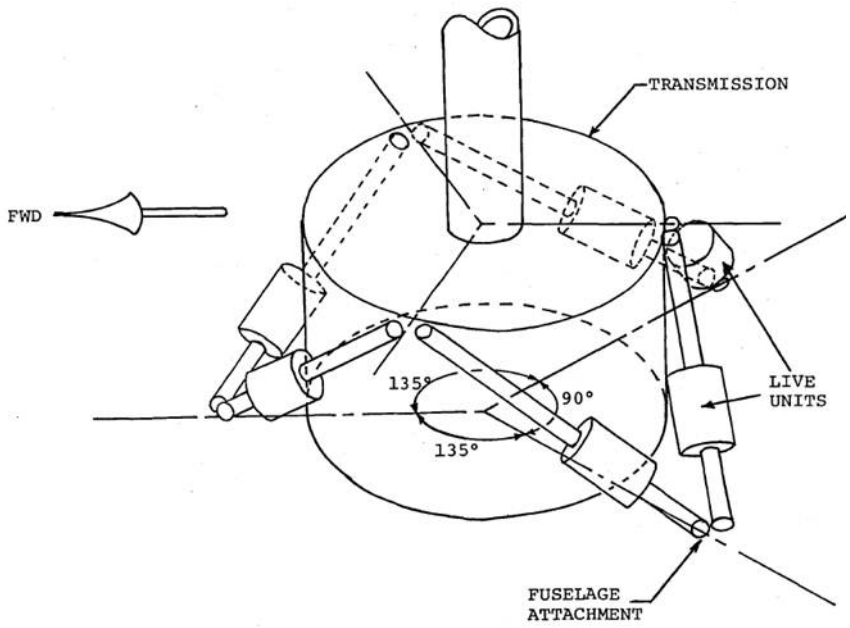

Figure 16: Total rotor isolation LIVE system[1, pp. 98]

A pressurizing spring K_M is used to keep the hydraulic liquid under pressure and ensures attachment of the tuning mass M_D to the hydraulic "pendulum", spring K_D generates the required restoring force. By choosing the sizes of the bellows and the tuning mass, the system can be tuned to alleviate vibration at a single frequency.

The design is later patented in 1988 after having numerous modifications and adjustments, Figure 18 shows this design, with a toroidal spring 2 that serves as the isolator spring, bellows 3 and 5, a tuning mass carriage 6 with an adjustable pendulum mass 9, a tension spring 7 to ensure that the bellows are kept under pressure, and a linear bearing 8. Unlike the LIVE system, the hydraulic fluid is not the primary inertial mass and does not require to be dense, the hydraulic fluid is still required to be incompressible and have low viscosity. Where the LIVE system uses a rubber spring this invention uses steel spring members giving it lower internal damping in comparison, which improve isolation performance.

Like the LIVE unit a single Hydraulic "Pendulum" isolator only alleviates vibration in a single axis, however, by using a multitude of Hydraulic "Pendulum" isolators in configurations like the one shown in Figure 16 a total vibration isolation system is achieved.

Having tested both a DAVI and the Hydraulic "Pendulum" isolators, some of the advantages of the hydraulic system reported by Braun is that it is lighter, smaller, symmetric around the attachment points, has less internal damping and therefore greater isolation effect (up to 99%) and the system is more linear because the mass moves in translation and not in an arc[4].

2.4 Tunable antiresonance vibration isolators

This is in reference to antiresonance vibration isolator that can be tuned in-flight to alleviate vibrations at more than one excitation frequency. Most in-flight tunable antiresonance vibration isolators seem to be modifications of the LIVE type isolator, it seems that the community deem liquid inertia vibration isolators or liquid "pendulum" type isolators superior to the previous arts, and therefore focus on advancing said isolators.

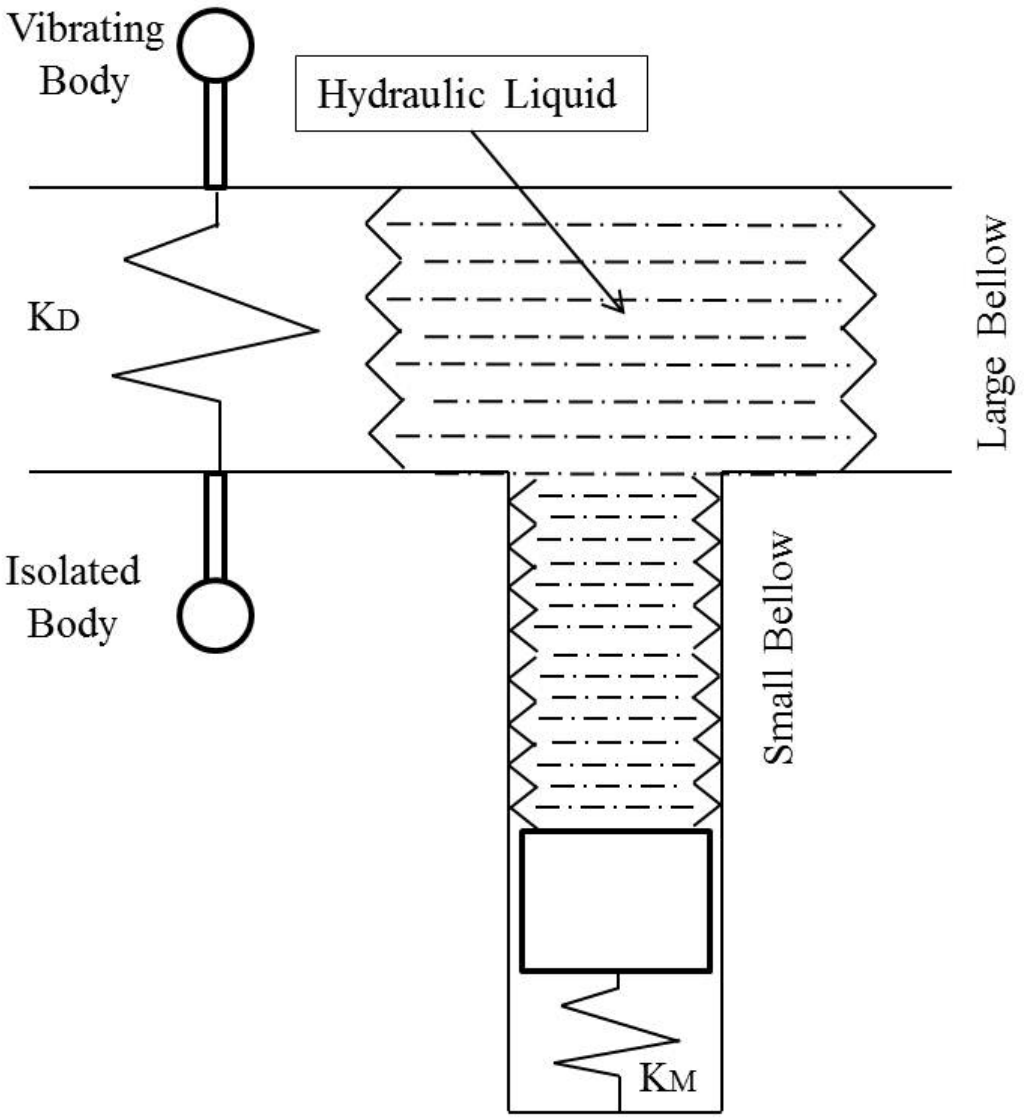

Figure 17: Hydraulic “pendulum” vibration isolator diagram

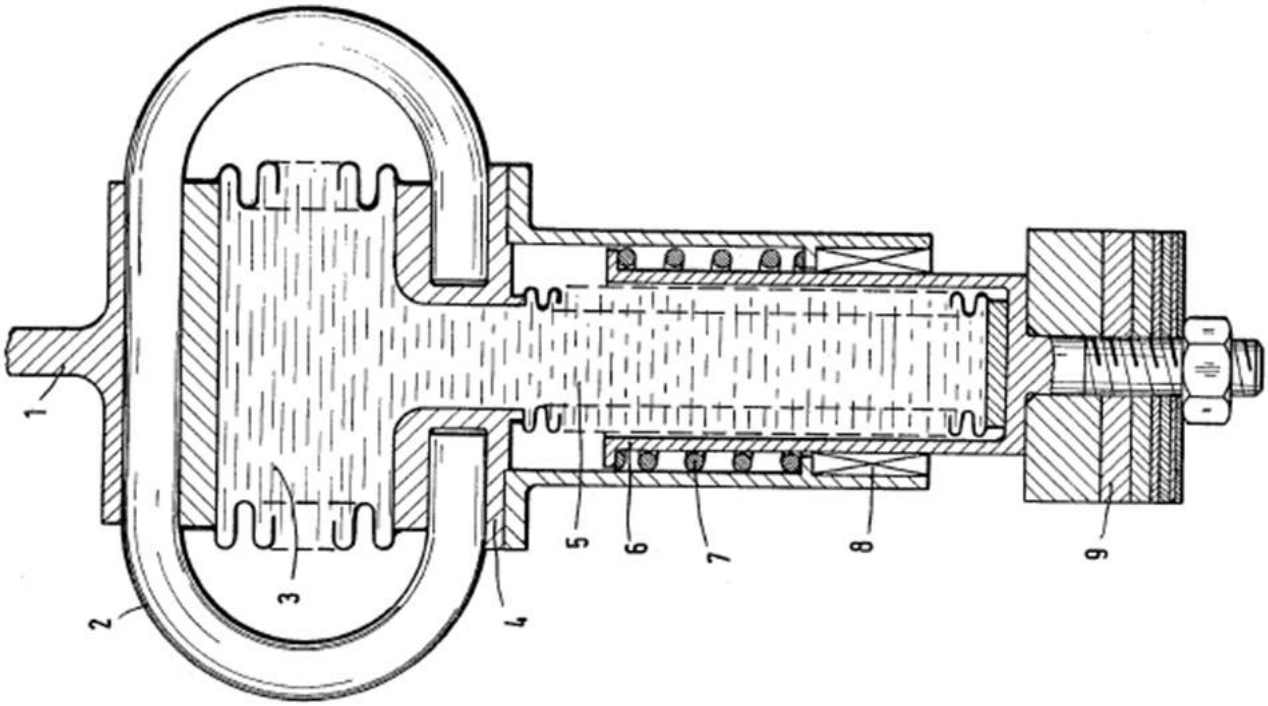

Figure 18: Hydraulic “pendulum” vibration isolator[5]

2.4.1 Adjustable tube liquid inertia vibration isolator

M.R Smith and F.B Stamps later patented a bi-directional tunable LIVE isolator[19], which is seen diagrammatically in Figure 19. This isolator has two LIVE units perpendicular to each other both sharing a common housing and each having an adjustable sleeve (shown as 83and 85) that form part of the inner wall of the tuning tube. By actuating the sleeves the tuning tubes can be either lengthened or shortened shifting the tuning frequency of either isolator independently to alleviate vibrations in a large range of frequencies. The patent describes using a rack and pinion enclosed the housing that actuates the sleeves, although any type of actuation method can be employed.

2.4.2 Tunable Vibration Absorbing Isolator

A tunable vibration isolator is developed by Du Plooy et al.[8] that uses pneumatic springs to tune the vibration isolation frequency. Figure 20 shows a diagram of the Tunable Vibration Absorbing Isolator or TVAI for short, it works on the same principles of the LIVE except that two pneumatic springs terminate the reservoirs at each side of the LIVE. Pressurising the pneumatic springs change the stiffness of the membranes, which controls the amount of fluid that is pumped through the tuning port, and this changes the tuning frequency of vibration isolation. This system claims to be robust and simple in design.

2.4.3 Induction motor liquid inertia vibration isolator

Lee et al. patented a linear induction motor liquid inertia vibration isolator as seen in Figure 21. It is a LIVE unit with a linear induction motor assembly (shown as number 535) around the tuning tube (529) that can be electrically

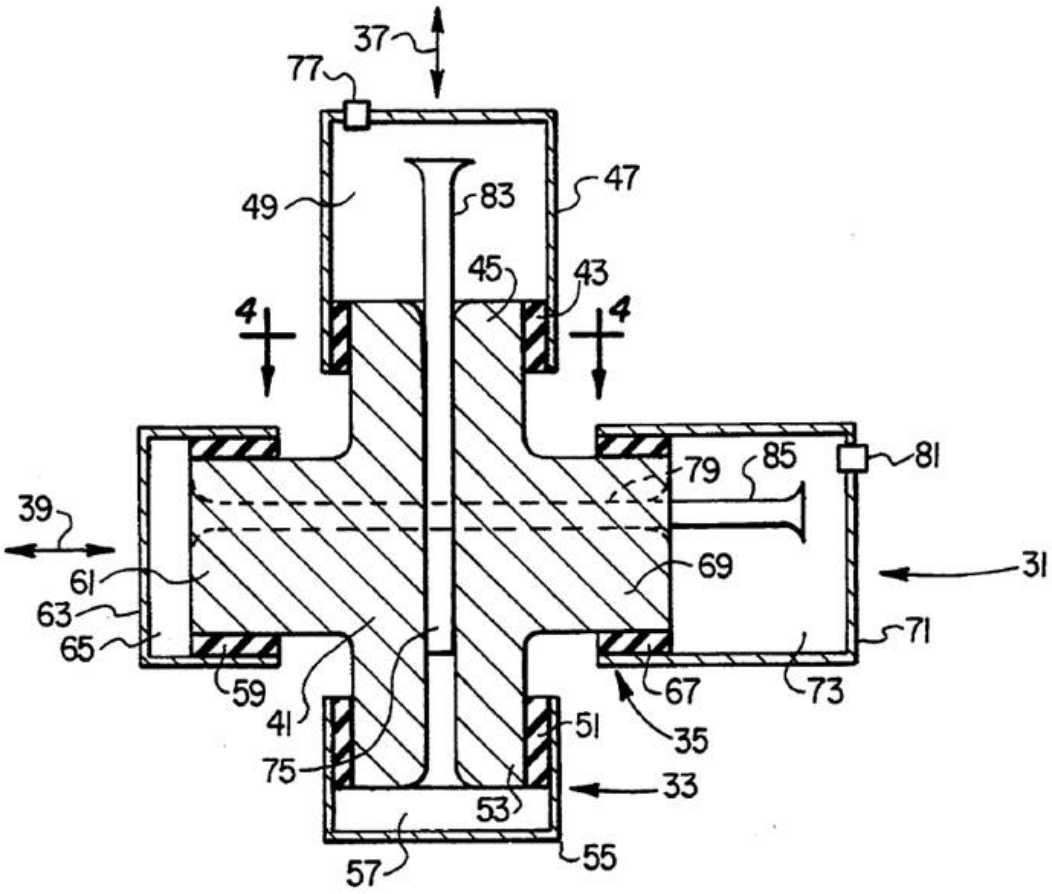

Figure 19: Bi-directional tunable LIVE [19]

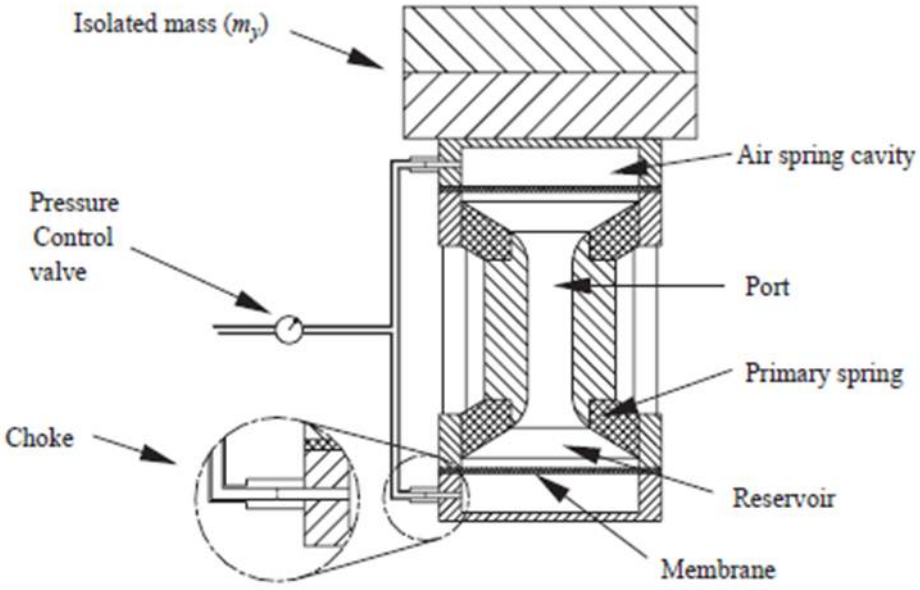

Figure 20: Tunable Vibration Absorbing Isolator[8]

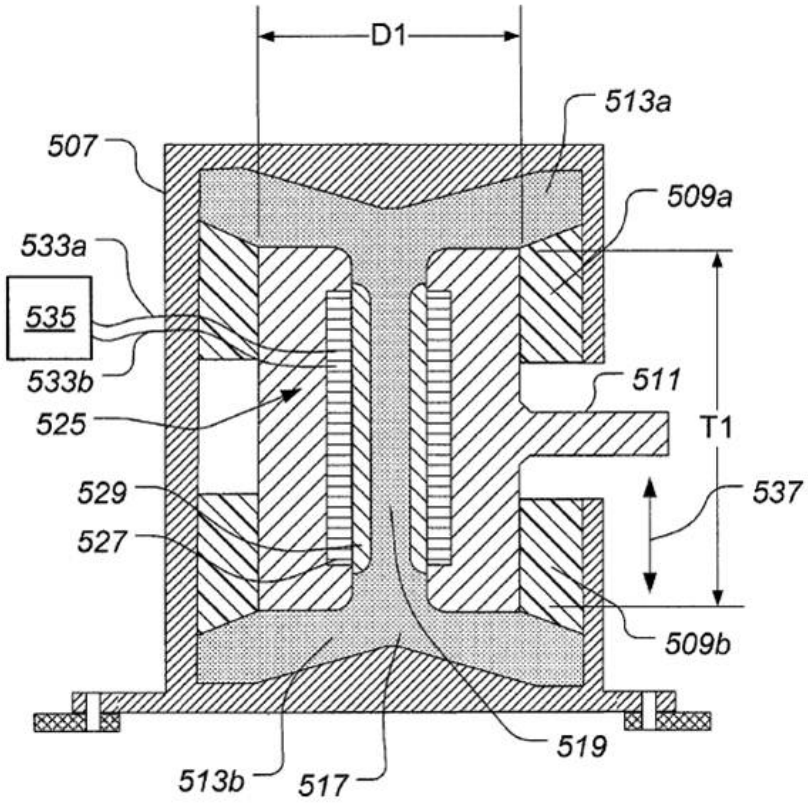

Figure 21: Inductance motor LIVE[16]

excited to generate a force on the magnetic inertial liquid (519) and therefore actively control the vibration isolation frequency[16].

2.5 Conclusion

Most prior arts, dating as far back as the 1960's, focus on passive single frequency antiresonance vibration isolation, whilst some systems are adapted, mostly liquid inertia vibration isolators, to actively isolate vibrations at more than one frequency. Very little literature is found on the adaptation of mechanical pendulum antiresonance vibration isolators for in-flight tunable multiple frequency isolation, and although these systems predate the more modern liquid inertia type isolator, there is merit in their further development and use as low cost, robust and low maintenance isolators for rotary wing unmanned aerial vehicles.

Rubber elastic springs, used on most LIVE systems, are susceptible to age and environmental hardening which can lead to crack formation and eventual brittle failure, giving them a finite lifespan where the units are replaced on regular intervals. In comparison, springs made from steels which are used in most mechanical pendulum vibration isolators can have theoretically infinite lifespans, if static and dynamic stresses remain below a fatigue limit stress. These are the main arguments for choosing the mechanical pendulum vibration isolator concept as the base design for the tunable isolator of this dissertation.

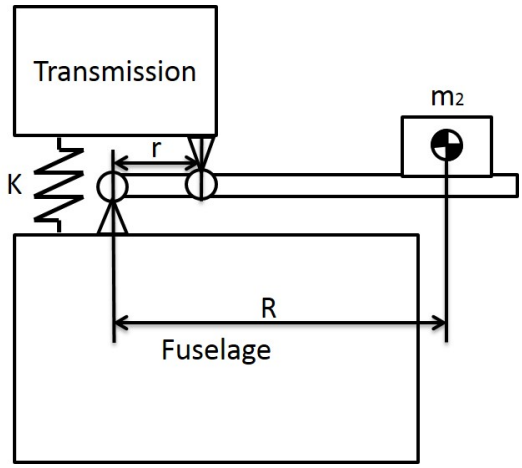

Figure 22: Vibration Isolation System Diagram

3 Feasibility studies

The literature review concludes that for this dissertation a mechanical pendulum antiresonance vibration isolator is chosen to be investigated further. As there are a multitude of different ways in tuning the said system the following feasibility studies aim to compare and quantify the efficiency of each method of tuning, to determining the best method for tuning the aforementioned system.

The first feasibility study investigates the alteration requirement of the design variables and their efficiency in shifting the vibration isolation frequency, to quantify the most effective method for in-flight tuning of the vibration isolator. A study on the feasibility of using ADAMS as a simulation tool for antiresonance vibration isolators then follows.

3.1 Changing of design variables to tune the isolator

The UAV's vibration isolation system is based on a modified inertial compensation system as discussed in Section 2.3.4, Figure 22 shows a diagram of the system with the design variables as discussed further in the feasibility study.

A method for re-tuning the antiresonance vibration system is required, consider the well known DAVI system tuning equation[10]:

$$\omega_a = \sqrt{\frac{K}{\frac{I}{r^2} - m_2 Q_R \times (1 - Q_R)}} \tag{1}$$

$$Q_R = \frac{R}{r} \tag{2}$$

with ω_a as the antiresonance frequency, K the overall system stiffness, I the moment of inertia of the tuning bar perpendicular to the length axis and into the page as seen on Figure 22 and Q_R the tuning bar length ratio. In most cases the $\frac{I}{r^2}$ term is significantly smaller than the $m_2 Q_R \times (1 - Q_R)$ term in the denominator of equation 1, therefore, the $\frac{I}{r^2}$ term is deemed negligible .

Notice that the antiresonance frequency is only a function of the tuning mass m_2, with neither the isolation mass M (fuselage) nor the base mass (transmission rotor assembly) having an influence. However, the isolation mass determine the position of the resonance frequency which should be sufficiently separated from the antiresonance frequency .

From equation 1 it is clear that the antiresonance frequency can be shifted by changing either the tuning mass m_2, the system stiffness K or the length ratio Q_R. The extent to which these parameters need to be changed in order to achieve vibration isolation over the UAV's working rotor speeds are investigated hereafter.

3.1.1 Varying the tuning bar mass m_2

Neglecting the $\frac{I}{r^2}$ term and rewriting equation 1 to solve for m_2 yields:

$$m_2 = \frac{K}{\omega_a^2 \times Q_R(1-Q_R)} \tag{3}$$

Defining two equations with m_a and m_b,where m_a and m_b are the masses required to achieve an antiresonance at ω_a and ω_b respectively

$$m_a = \frac{K}{\omega_a^2 \times Q_R(1-Q_R)} \tag{4}$$

$$m_b = \frac{K}{\omega_b^2 \times Q_R(1-Q_R)} \tag{5}$$

Dividing equation 4 by 5 whilst keeping K and Q_R constant:

$$\frac{m_a}{m_b} = \frac{\frac{K}{\omega_a^2 \times Q_R(1-Q_R)}}{\frac{K}{\omega_b^2 \times Q_R(1-Q_R)}} = \left(\frac{\omega_b}{\omega_a}\right)^2 \text{ or } \frac{m_b}{m_a} = \left(\frac{\omega_a}{\omega_b}\right)^2 \tag{6}$$

Defining mass and antiresonance frequency ratios:

$$R_m = \frac{m_b}{m_a}; R_f = \frac{\omega_b}{\omega_a}$$

equation 6 then becomes:

$$R_m = \frac{1}{R_f^2} \tag{7}$$

Plotting equation 7 shows this relationship; see figure 23.

Equation 7 is a dimensionless equation describing the generalised relationship between mass and antiresonance frequency. The mass ratio is inversely proportional to the antiresonance frequency ratio squared, therefore, increasing the antiresonance from ω_a to ω_b requires a decrease in the tuning mass and vice versa.

A rotor speed range of $\pm 10\%$ around a median rotor speed is defined for the UAV, the driving frequency is directly proportional to the rotor speed, therefore a tuning range of $\pm 10\%$ around the median antiresonance frequency is required to eliminate vibrations at all rotor speeds.

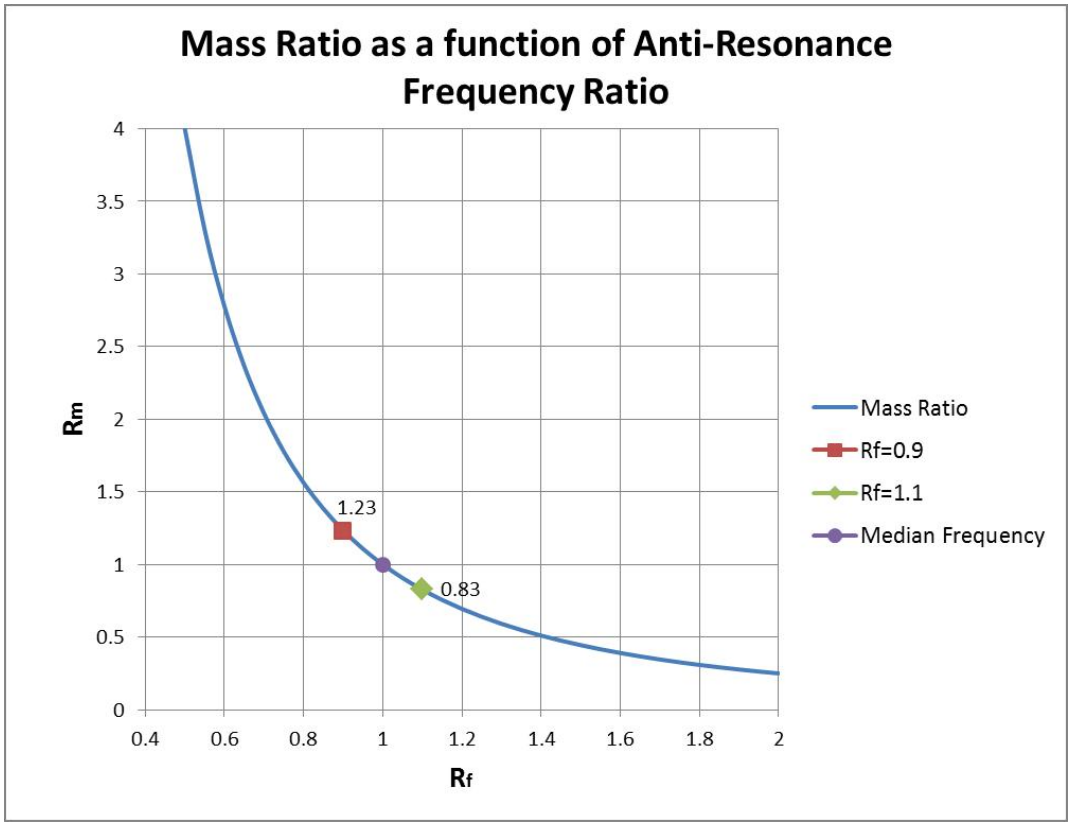

Figure 23: Mass ratio as a function of frequency ratio

Figure 23 shows the hyperbolic decay of the mass change required as a function of the desired frequency change ratio, therefore this method is more efficient at increasing the antiresonance than decreasing it. For example a 50% decrease in mass results in a 40% increase in antiresonance frequency, whereas a 50% increase in mass only corresponds to a 20% increase in antiresonance frequency.

This project is only concerned in a 10% increase ($R_f = 1.1$) and decrease ($R_f = 0.9$) around a median antiresonance frequency, Figure 23 shows that this corresponds to a 17% ($R_m = 0.83$) decrease and 23% ($R_m = 1.23$) increase in mass respectively. A total mass change of 40% is thus required to alleviate vibrations over the bandwidth of interest.

3.1.2 Varying the system stiffness K

Similarly as in section 3.1.1 on page 21 rewriting the tuning equation to solve for K yields:

$$K = \omega_a^2 \times Q_R\,(1 - Q_R) \times m_2 \tag{8}$$

Defining two states K_a and K_b:

$$K_a = \omega_a^2 \times Q_R\,(1 - Q_R) \times m_2 \tag{9}$$

$$K_b = \omega_b^2 \times Q_R\,(1 - Q_R) \times m_2 \tag{10}$$

Keeping Q_R and m_2 constant we divide equations 9 and 10:

$$\frac{K_a}{K_b} = \frac{\omega_a^2 \times Q_R\,(1 - Q_R) \times m_2}{\omega_b^2 \times Q_R\,(1 - Q_R) \times m_2} = \left(\frac{\omega_a}{\omega_b}\right)^2 \; or \; \frac{K_b}{K_a} = \left(\frac{\omega_b}{\omega_a}\right)^2 \tag{11}$$

Defining stiffness and antiresonance ratios as $R_K = \frac{K_b}{K_a}$ and $R_f = \frac{\omega_b}{\omega_a}$, Equation 11 becomes:

$$R_K = R_f^2 \tag{12}$$

Plotting Equation 12 gives insight to this relationship; see figure 24.

Equation 11 is a non-dimensionalised general relationship between stiffness and antiresonance. The stiffness ratio is directly proportional to the antiresonance frequency ratio squared. An increase in stiffness will increase the antiresonance frequency, and decreasing it will decrease the frequency.

In contrast to changing the mass, this method is more effective in lowering the antiresonance frequency than raising it around a mean antiresonance frequency. From Figure 24 a desired increase of 10% ($R_f = 1.1$) in antiresonance frequency requires a 21% increase in stiffness ($R_K = 1.21$) and a 10% decrease ($R_f = 0.9$) requires a 19% reduction in stiffness ($R_K = 0.081$). A total stiffness change of 40% is thus required to alleviate vibrations at all rotor speeds.

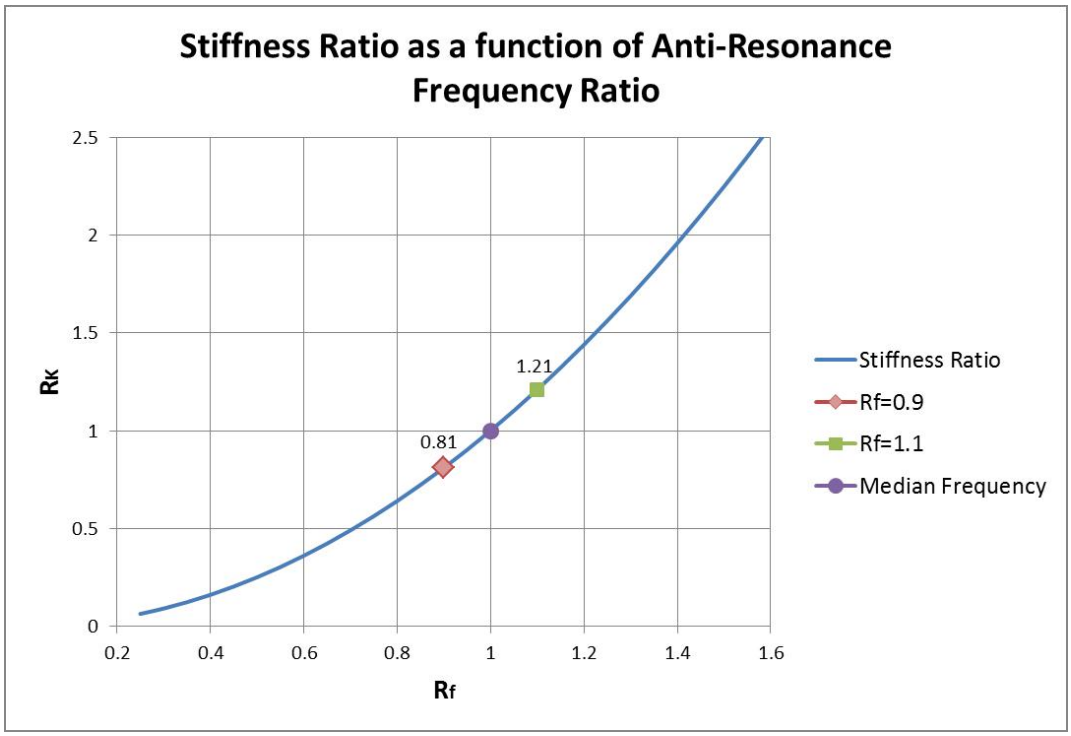

Figure 24: Stiffness ratio as a function of antiresonance frequency ratio

3.1.3 Varying tuning bar length ratio Q_R

The tuning equation is rewritten to solve for Q_R, by keeping stiffness and tuning mass constant:

$$Q_R\,(1-Q_R) = \frac{K}{\omega_a^2 \times m_2} \tag{13}$$

Defining two states Q_{R1} and Q_{R2} corresponding to ω_a and ω_b:

$$Q_{R1}\,(1-Q_{R1}) = \frac{K}{\omega_a^2 \times m_2}\;;\; Q_{R2}\,(1-Q_{R2}) = \frac{K}{\omega_b^2 \times m_2}$$

Dividing these equations give:

$$\frac{Q_{R1}\,(1-Q_{R1})}{Q_{R2}\,(1-Q_{R2})} = \frac{\frac{K}{\omega_a^2 \times m_2}}{\frac{K}{\omega_b^2 \times m_2}} = \frac{\omega_b^2}{\omega_a^2} \tag{14}$$

Defining the antiresonance frequency ratio as:

$$R_f = \frac{\omega_b}{\omega_a} \tag{15}$$

Equation 14 then equates to:

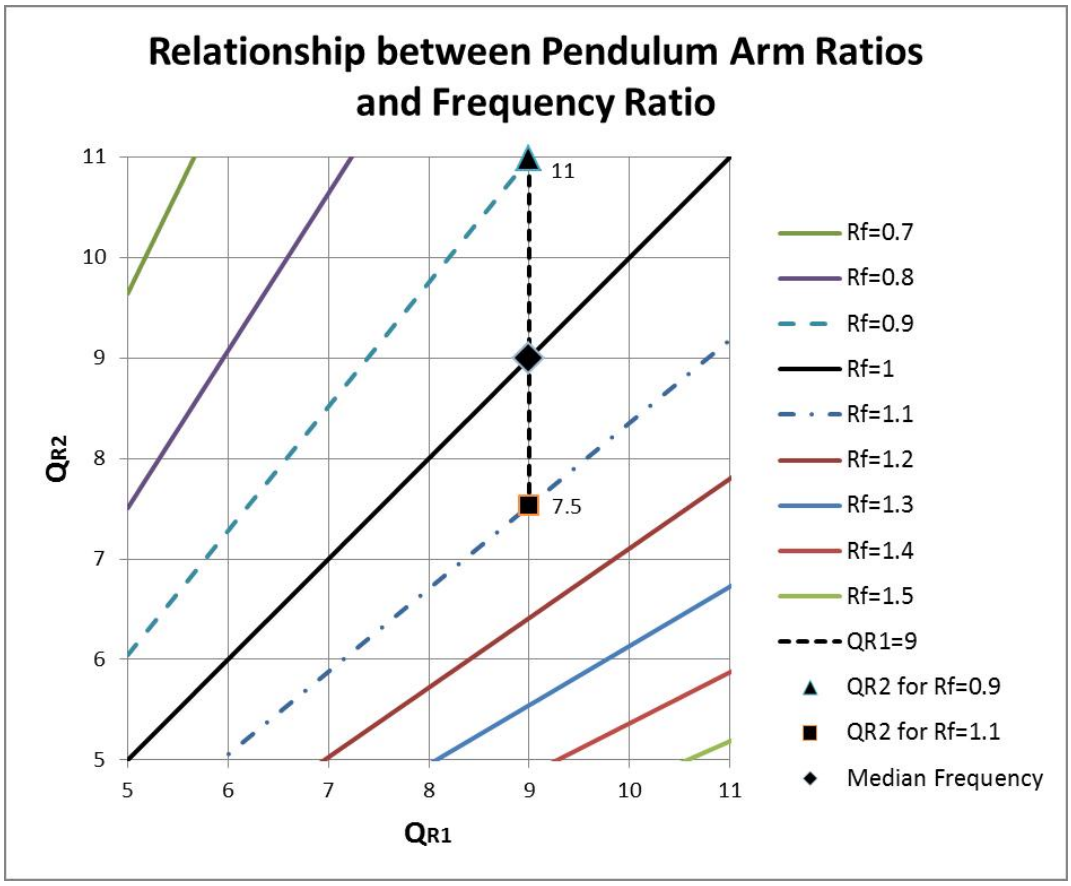

Figure 25: Frequency ratio as a function of pendulum arm ratios

$$\frac{Q_{R1}(1-Q_{R1})}{Q_{R2}(1-Q_{R2})} = R_f^2 \tag{16}$$

Defining the ratio of pendulum arm ratios $R_Q = \frac{Q_{R1}}{Q_{R2}}$ gives:

$$\frac{R_Q(Q_{R2}^{-1}-R_Q)}{(Q_{R2}^{-1}-1)} = R_f^2 \tag{17}$$

Equation 17 is implicit because R_Q is a function of R_f, Q_{R1} and Q_{R2} . Therefore, the value of Q_{R2} required to achieve a certain change in frequency is dependent on the initial choice of Q_{R1}. Plotting Equation 16 with constant values for R_f leads to the graph shown in figure 25.

Figure 25 shows the constant antiresonance frequency ratio lines R_f, any location on a curve defines the values of Q_{R1} and Q_{R2} that are required to achieve said frequency ratio. Notice that for any constant value of Q_{R1} the jump in Q_{R2} required to shift from one frequency ratio to another becomes larger the larger the initial value of Q_{R1}, as the constant ratio lines diverge away from one another with increasing Q_{R1}.

Therefore the smallest initial ratio of Q_{R1} would be optimum and require the minimum shift in the pendulum arm ratio. However, the smaller the initial pendulum arm ratio the heavier the pendulum mass required to alleviate the required frequency of vibration.

Because this system is intended for aviation purposes, optimisation for least mass takes precedence, leading to most antiresonance Vibration Isolators used in the aviation industry to have a pendulum arm ratio as large as possible reducing the pendulum arm mass required, and thus lowering the total mass of the system.

Although no literature was found stating this, most pendulum arm ratios tend to be around 7 to 9, I believe this ratio is capped at 9 due to various design restrictions in term of available space in the transmission bay, required stiffness of the transmission suspension, and the geometrical constraints of the hinge proximity that define r in the ratio $Q_R = \frac{R_p}{r}$. Thus for the purpose of this feasibility study a median and initial value of $Q_{R1} = 9$ is selected.

The constant lines $Rf = 1.1$ and $Rf = 0.9$ correspond to a 10% increase and decrease of the antiresonance frequency respectively, with an initial value of $Q_{R1} = 9$. Figure 25 shows that Q_{R2} values should be 7.5 and 11 respectively to achieve said antiresonance frequency shifts. This corresponds to a decrease of 17% in pendulum arm ratio ($R_Q = 0.83$) to shift the antiresonance frequency up by10%, and an increase of 22% in Q_R ($R_Q = 1.22$) to lower the antiresonance frequency by 10% from the median frequency.

Overall the pendulum arm ratio must change by 39% to cover the required total 20% shift in antiresonance frequency.

There are two ways of changing the pendulum mass arm ratio $Q_R = \frac{R}{r}$, firstly by changing the total pendulum arm length R and secondly by changing the hinge distance r. Defining a ratio of pendulum arm ratios with a constant pendulum arm length R :

$$R_{Qr} = \frac{Q_{R2}}{Q_{R1}} = \frac{R}{r_b} \times \frac{r_a}{R} = \frac{r_a}{r_b} \tag{18}$$

Defining the hinge distance ratio as $R_r = \frac{r_b}{r_a}$ yields:

$$R_{Qr} = \frac{1}{R_r} \tag{19}$$

Repeating this process but keeping r a constant:

$$R_{QR} = \frac{Q_{R2}}{Q_{R1}} = \frac{R_b}{r} \times \frac{r}{R_a} = \frac{R_b}{R_a} \tag{20}$$

Defining a pendulum arm length ratio $R_R = \frac{R_b}{R_a}$ yields:

$$R_{QR} = R_R \tag{21}$$

Note that $R_{QR} = R_{Qr}$, thus we use R_Q as a general ratio describing change of the ratio of pendulum arm ratios, because all quantities are in terms of ratios both methods can be plotted on the same graph in comparison to their respective change on the ratio R_Q, see Figure 26.

Figure 26 shows two horizontal lines for the 22% increase and 17% decrease of the pendulum arm ratio required to lower and raise the antiresonance frequency by 10% as shown in Figure 25. The red and blue curves show the ratio of pendulum ratios as a function of pendulum arm length ratio and pendulum hinge length ratio respectively.

The change in the pendulum arm length R is directly proportional to the change in pendulum arm ratio, see Equation 21, thus a 22% increase and 17% decrease in pendulum arm ratio corresponds to the same magnitude of change in the pendulum arm length. This method is thus equally effective at lowering the Pendulum Arm Ratio as it is in raising it.

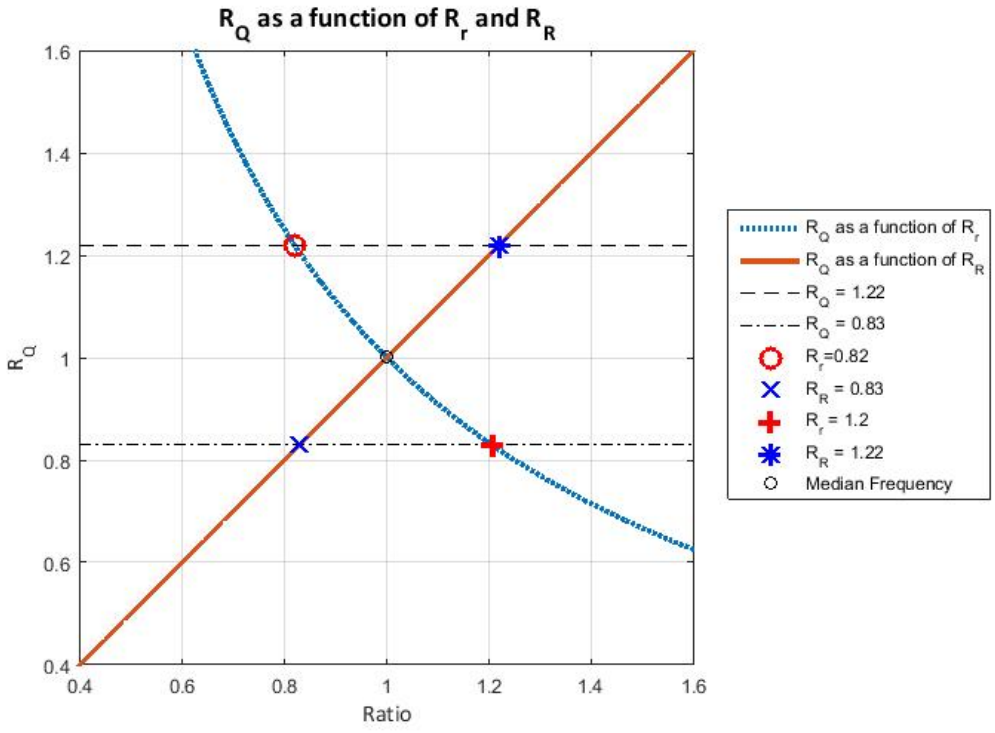

Figure 26: Relationship between the ratio of pendulum ratios and the ratio of hinge lengths and pendulum arm lengths

The change in the pendulum arm ratio with respect to changing the hinge length is a reciprocal function, and as seen from the graph, changing the hinge length is exponentially more effective in raising the pendulum arm ratio than it is in lowering it. So for the aforementioned required change in Pendulum Arm Ratio the Hinge Length should be decreased by 20% and increased by 18%, for a total change of 38% to achieve the total frequency shift of 20%.

Changing the hinge length requires a slightly smaller overall change in comparison to changing the pendulum arm length, 38% compared to 39%, to achieve the required antiresonance frequency shift. Clearly the benefit in changing the hinge length compared to changing the pendulum arm length is negligible for small shifts in antiresonance frequency like 10%, and a decision should be made by investigating the practical implications of each method.

For other implementations of antiresonance vibration isolation systems, where large decrease in antiresonance is required, changing the hinge length would greatly outperform changing the pendulum arm length. In contrast, implementations where large increases in antiresonance frequencies are required, changing the pendulum arm length will greatly outperform changing the hinge length.

3.1.4 Practical implementation for tuning isolator

Lastly an investigation on the practical implementation of these two methods are discussed.

Figure 27 shows a method of adjusting the pendulum arm ratio using an adjustable concentrated mass m_m , the concentrated mass is shifted up and down the pendulum arm, subsequently shifting the pendulum assembly mass CG, which in turn changes the pendulum arm ratio Q_R.

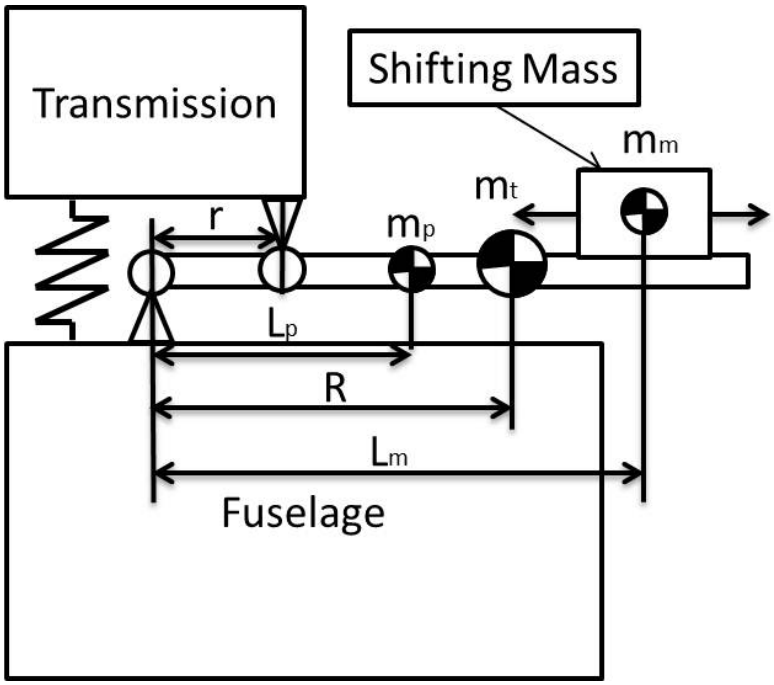

Figure 27: Shifting mass on a DAVI

The Pendulum arm ratio is defined as $Q_R = \frac{R}{r}$ shown in Figure 27, the Pendulum Arm Length R is defined as the length from the first hinge position to the centre of mass of the pendulum arm assembly m_t. This centre of mass cannot be shifted directly as the pendulum assembly mass is the sum of pendulum arm mass m_p and pendulum concentrated mass m_m of which the pendulum arm centre of gravity cannot be shifted. Therefore the pendulum assembly centre of mass can only be shifted by shifting the Pendulum Concentrated mass m_m.

Pendulum arm length is defined as:

$$R = \frac{m_p L_p + m_m L_m}{m_t} \tag{22}$$

with pendulum assembly mass being:

$$m_t = m_p + m_m \tag{23}$$

Defining a ratio of pendulum concentrated mass as a function of total mass $R_{mf} = \frac{m_m}{m_t}$ and substituting into Equation 22 yields:

$$R = L_p - R_{mf} L_p + R_{mf} L_m \tag{24}$$

$$R = L_p + R_{mf} (L_m - L_p) \tag{25}$$

Assuming that L_p and L_m remain constant, we investigate the limit states of Equation 25 with respect to the ratio R_m.

As $R_m \to 0$, meaning that the Pendulum Mass is very small compared to the total mass, then $R \to L_p$ which will be a minimum for this equation. As $R_m \to 1$, meaning that the Pendulum mass makes up the majority of the total mass, then $R \to L_m$ which is a maximum for this equation.

Therefore, for maximum effectiveness of shifting the pendulum arm ratio by moving the shifting mass requires that the pendulum arm should always be as light as possible with the shifting mass comprising as large a part of the total mass of the pendulum assembly as possible.

However, because the pendulum arm has to be durable and stiff this is not an easy objective. The pendulum arm mass for this prototype turns out to be almost half the total weight of the pendulum assembly, meaning that quite large shifts in the concentrated shifting mass is required for small shifts in the pendulum arm ratio.

3.1.5 Conclusion

It is clear from the feasibility study that, for the 10% antiresonance frequency shift range of interest in this dissertation, no specific design variable change quantifiably outperforms another with respect to tuning the antiresonance. All three methods requiring a percentage wise change of roughly the same magnitude, about 40%, to cover the frequency range of interest.

Thus, further investigation is required to determine the best solution based on other criteria which is later covered in the conceptual designs.

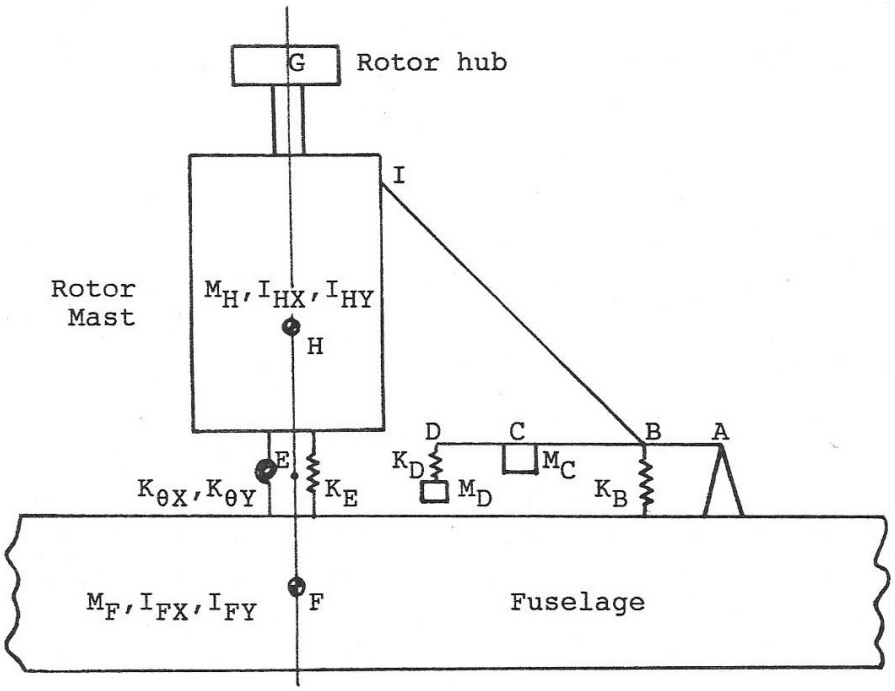

Figure 28: Karl Lippert's antiresonance vibration isolation system [17]

3.2 Feasibility of using ADAMS for simulation of antiresonance vibration isolation systems

MSC ADAMS is one of the worlds leading multi-body dynamics analysis programs, making it the perfect candidate for designing a vibration isolation system. However, it first needs to be determined if ADAMS has the ability to model these systems with the required accuracy, especially with respect to vibration analysis.

A complete parametrised model of the antiresonance vibration isolation system proposed by Lippert KG [17] is modelled in ADAMS and compared to the Analytical results obtained in his dissertation. This study will validate the use of ADAMS to further develop an antiresonance vibration isolation system for the unmanned rotary winged helicopter that is the subject of this dissertation.

The model proposed in Lippert's dissertation have the following specifications.

Shown in Figure 28 is a quarter model of an antiresonance vibration isolation system as proposed by Lippert. All the masses are denoted by M_*, stiffnesses by K_* and moments of inertia by I_*. The x-axis is defined as the forward facing direction of the helicopter, therefore, inertias or stiffnesses with subscript x and y are the roll and pitch rotation degree of freedom respectively.

This system claims to alleviate vibrations at the main rotor head frequency and its first harmonic for both pitch, roll and heave excitations. Based on the DAVI as described in Section 2.3.4 but with an added subsystem comprising of mass spring system K_D and M_D to alleviate vibrations at the first harmonic.

Lippert studied this system in the form of a medium size helicopter of 4200 kg with the following specifications:

Q_{R1} and Q_{R2} are the pendulum arm ratios as defined in any DAVI system.

The inertias are calculated using the following equations:

$$I_{FX} = (M_F + M_H)^2 / 6500 \tag{26}$$

$M_F = 4200\,kg$	$K_E = 7.5E6\,N/m$
$M_H = 800\,kg$	$K_B = 5E6\,N/m$
$M_C = 6.2\,kg$	$K_D = 4.7E4\,N/m$
$M_D = 2.3\,kg$	$K_{\theta X}\,and\,K_{\theta Y} = 4.78E6\,Nm/rad$
$Q_{Rh1} = 9$	$L_{EG} = 1.2\,m$
$Q_{Rh2} = 9.45$	$L_{EH} = 0.5\,m$
$L_{AB} = 0.08\,m$	$L_{EF} = 0\,m$

Table 2: Lippert model specifications [17]

$$I_{FY} = (M_F + M_H)^2 / 900 \tag{27}$$

$$I_{HX} = (M_F + M_H)^2 / 42000 \tag{28}$$

$$I_{HY} = (M_F + M_H)^2 / 40000 \tag{29}$$

These equations are derived from empirical data relating helicopter inertias to their total mass[17].

A model was created in ADAMS following these specifications and compared to Lippert's model, this is a good comparison of a numerical ADAMS solution to that of Lippert's Analytical solutions, and would validate the use of ADAMS for the design of the isolation system proposed in this dissertation.

Figure 29 shows the ADAMS model with corresponding coordinate system in the bottom left corner. Frequency response functions are generated using ADAMS for the following cases:

1. Fuselage heave response to vertical force Fz
2. Fuselage pitch response to moment My and force Fx
3. Fuselage roll response to moment Mx and force Fy

Note that the reference forces and moments are all applied at point G, the rotor hub assembly. The results from the ADAMS vibration analysis is compared to that of Lippert's thesis, the frequency response functions of Lippert's dissertation were extracted from the hard-copy of said dissertation by scanning the graphs and using open source digitiser software to convert them to digital CSV format.

Figures 30 to 32 all show almost exact correlation between the ADAMS model and the Lippert model, there are very small discrepancies on certain points on the graphs. These discrepancies are assumed to be caused by slight differences in how the parts were constrained in the two models or by user error during the digitising process where one has to select points by manually clicking on a image of the curves.

Lippert's dissertation does not define how the parts are constrained so assumptions were made when constraints were applied in the ADAMS model.

The correlation between the analytical Lippert- and the ADAMS model created in this work, validates the use of ADAMS for developing antiresonance vibration isolators.

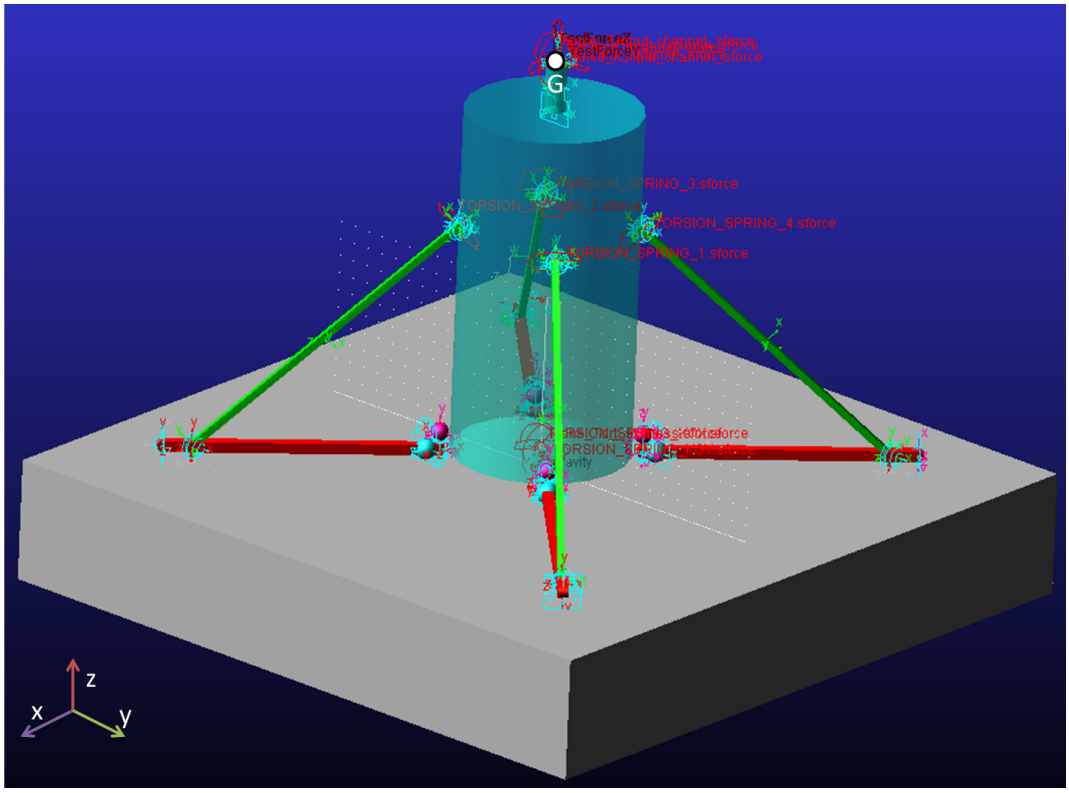

Figure 29: Lippert's model recreated in ADAMS

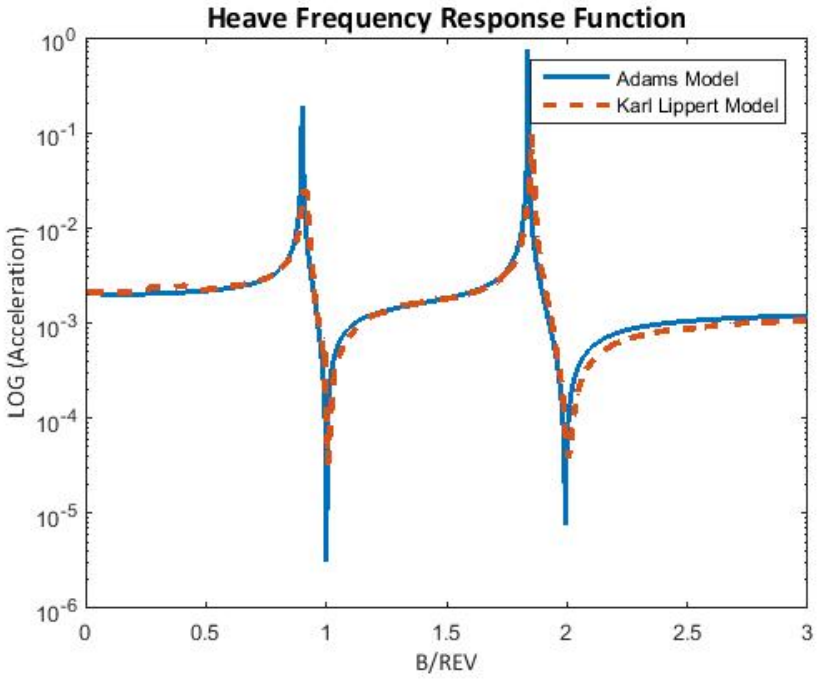

Figure 30: Fuselage heave response to vertical force Fz

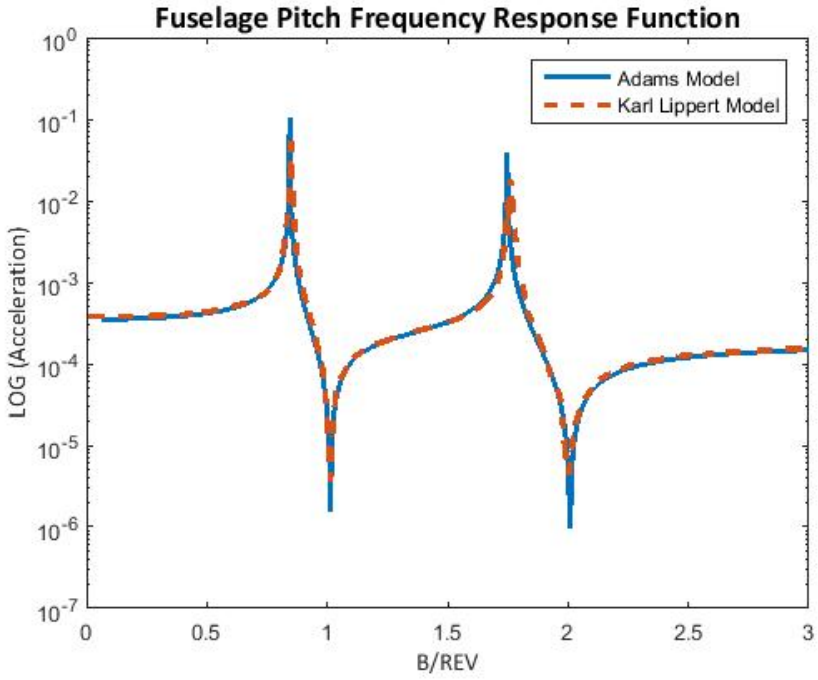

Figure 31: Fuselage pitch response to moment My and force Fx

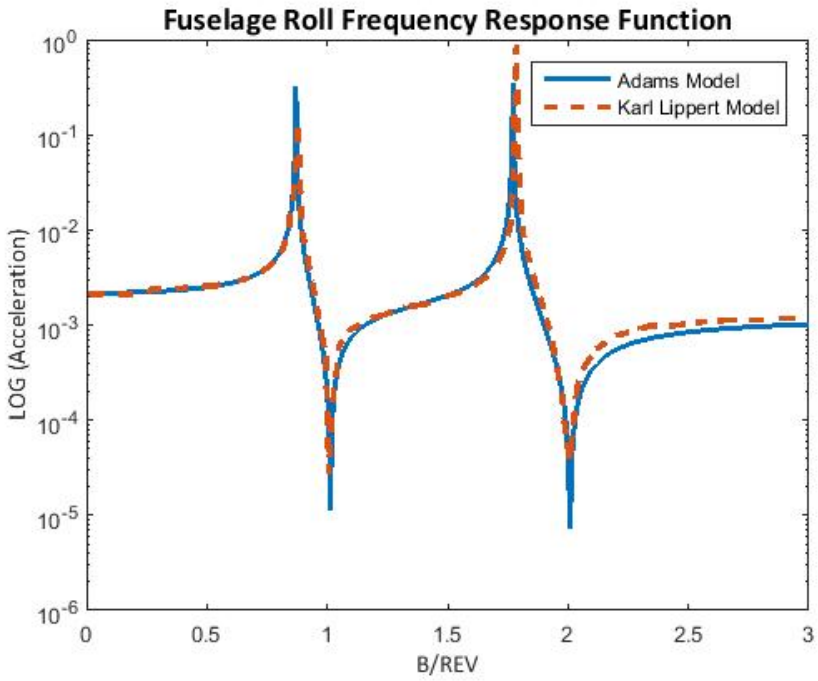

Figure 32: Fuselage roll response to moment Mz and force Fy

4 Concept designs

Based on the conclusion of the feasibility study Section 3.1.5, that no change in any one specific design variable outperforms another, means that the optimal system for tuning the antiresonance vibration isolator encompasses a much larger, complex and abstract list of criteria like: overall weight, design simplicity, practicality, robustness, reliability, and many others. Furthermore, there are multiple ways of changing each of the variables in the aforementioned feasibility study, further adding to the complexity. Therefore, a few concepts are developed for each method of tuning, each concept is discussed, scrutinised and the most suitable candidate is chosen as the system to be developed further in the dissertation.

Before the concept designs are displayed please note that most of them have diagrammatic visualisations of the spring or stiffness of the transmission relative to the fuselage in the form of a coil spring. Although this is not impossible it is more likely that leaf spring are used in systems where space is limited in the vertical axes. Figure 33 shows the principle way in which a leaf spring functions.

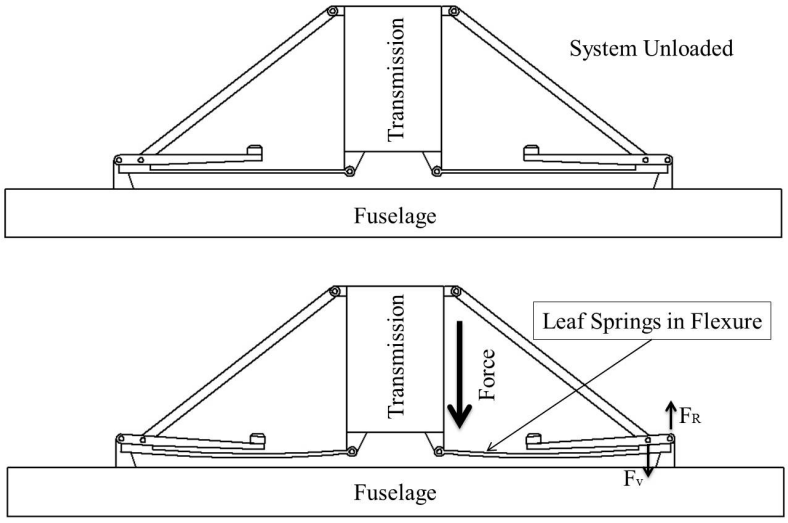

Figure 33: Flexure of leaf springs

The vertical force F_v at the stay hinge is resisted by the vertical reaction force F_R at the fuselage hinge, the distance between the two hinges creates a moment couple which is in return resisted by the leaf spring and taken up as flexure in the leaf spring. This creates a vertical stiffness much like a helical spring would.

4.1 Varying of tuning bar mass

Hereby follows a concept for changing the mass of the tuning bar weight.

4.1.1 Oil Reservoir

Seen in figure 34 is a system for changing the mass of the tuning bar weight using hydraulics. A hydraulic fluid is pumped in and out of a reservoir, increasing or decreasing the mass of the tuning bar weight. A plunger and spring system is also required to ensure that the hydraulic fluid is always under positive pressure, ensuring that the fluid is not able to splash around causing adverse dynamic effects.

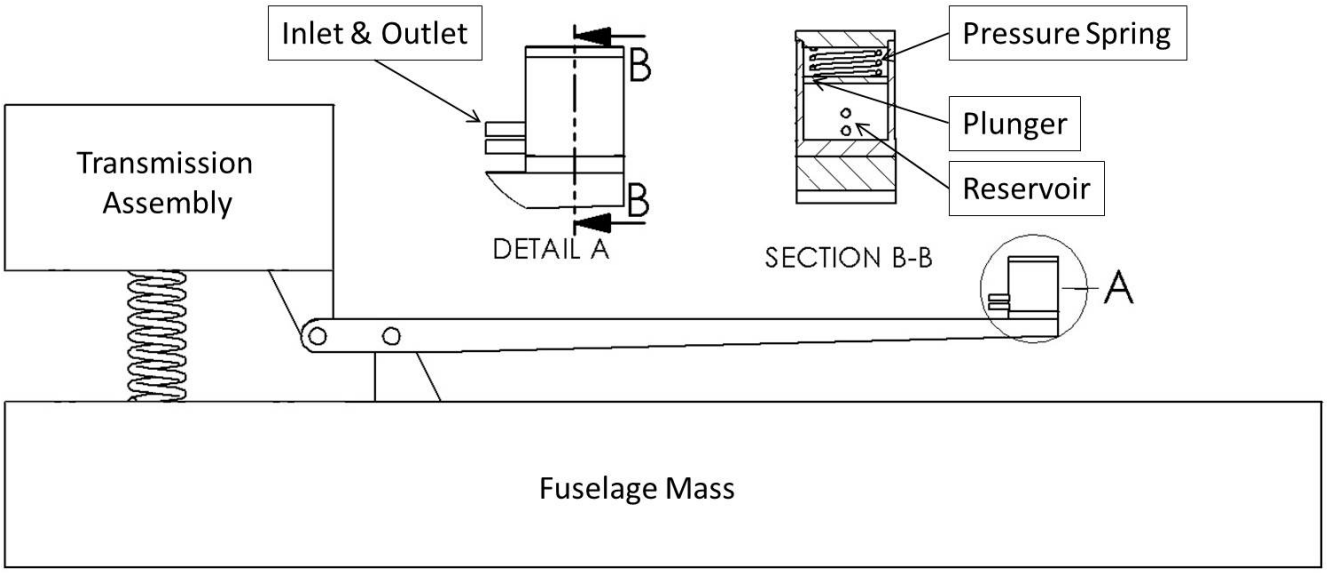

Figure 34: Hydraulic mass

Furthermore, the stiffness of this spring plunger system will depend on the required pumping speed as pumping the fluid out of the reservoir should not cause too large a negative pressure causing cavitation in the fluid, the spring plunger system ensures positive pressure head counteracting this effect. This could lead to quite heavy spring plunger assemblies which in turn required a shorter tuning bar length to compensate for a gross larger tuning bar mass design.

Most commercial fluids used for hydraulics have low densities of about $850\frac{Kg}{m^3}$ in comparison to that of steel's $7800\frac{Kg}{m^3}$, therefore a system using hydraulic fluid would be 9 times larger to achieve the same weight than an equivalent system using steel. Although there are fluids that are very dense like mercury for example, they're not designed for hydraulic applications and therefore do not have all the necessary traits that define a hydraulic fluid, like low viscosity and corrosion inhibition.

From a pump perspective the higher the density of the liquid the harder it is to pump, furthermore, fast pumping speeds will be required to switch between frequencies at an acceptable speed. This will ultimately result in relatively large and heavy pump systems, which is not ideal for the low weight design doctrine of helicopters in general.

4.2 Varying system stiffness

There are many ways to change the stiffness of a system, a few concept designs are shown to determine the practical implications of such a system.

4.2.1 Pressurised bellows

Shown in figure 35 is a concept design for altering the stiffness of the system using a pressurised bellows. A bellows is attached between the transmission and the fuselage that is pressurised using the combustion gasses from the aircraft's engine, a pressure regulator is required in conjunction with feedback control via a pressure transducer to determine and control the pressure inside the bellows.

The bellows can be made from a variety of materials from rubber infused with fibre to aluminium or steel corrugated vessels like the one depicted in figure 35. Pressurised gas can be bled at high pressure from the combustion chamber

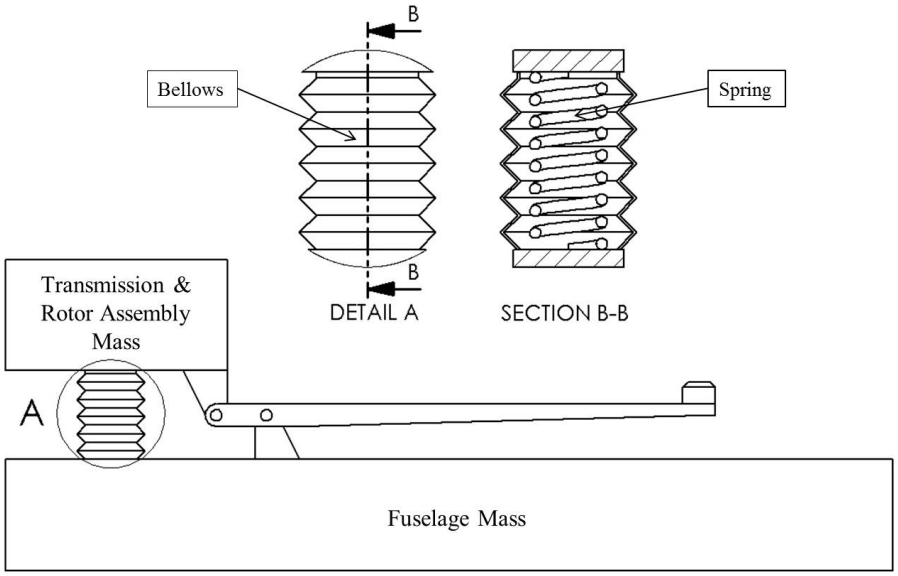

Figure 35: Changing the system stiffness using a pressurised bellows

of the internal combustion engine and fed to said bellows. By increasing the pressure in the bellows the stiffness of the system will increase; the opposite is true if the pressure is lowered.

Pressurising gas is an irreversible adiabatic process and therefore introduces damping into the system as energy is turned into heat during compression, damping has an adverse effect on the efficiency of an antiresonance vibration isolation system, drastically reducing the isolation effect. Furthermore, the high temperature gasses used to compress the bellows, create a high corrosive environment that would require more maintenance. This system would require active feedback control of the pressure inside the bellows, this added complexity and parts is not ideal for a robust simple, low maintenance design.

Positive aspects of this system are infinite tuning range, no loose parts , no extra power sources required and a fairly simple mechanical design.

4.2.2 Shifting the leaf spring connection point

Another way of altering the stiffness a leaf spring suspension system would be to shift the location of where the leaf spring is supported at one of its ends, effectively making the system more or less stiff by lengthening or shortening the active spring section.

Figure 36 shows a concept of such a system, a ball screw drives a spring loaded roller arm that firmly supports the loose end of the leaf spring. The pinch point of the two rollers define the effective length L_{eff} of the leaf spring as depicted in figure 36.

One positive aspect of this system is an infinite tuning range between its minimum and maximum tuning frequencies. Negative aspects are plenty, with a complex and relatively heavy design, many moving parts, lots of joints and wearable mechanisms to name a few.

Furthermore, a feedback control system will be required to determine the position of the pinch point with respect to the rotor speed and corresponding antiresonance frequency required, this adds complexity and more maintenance.

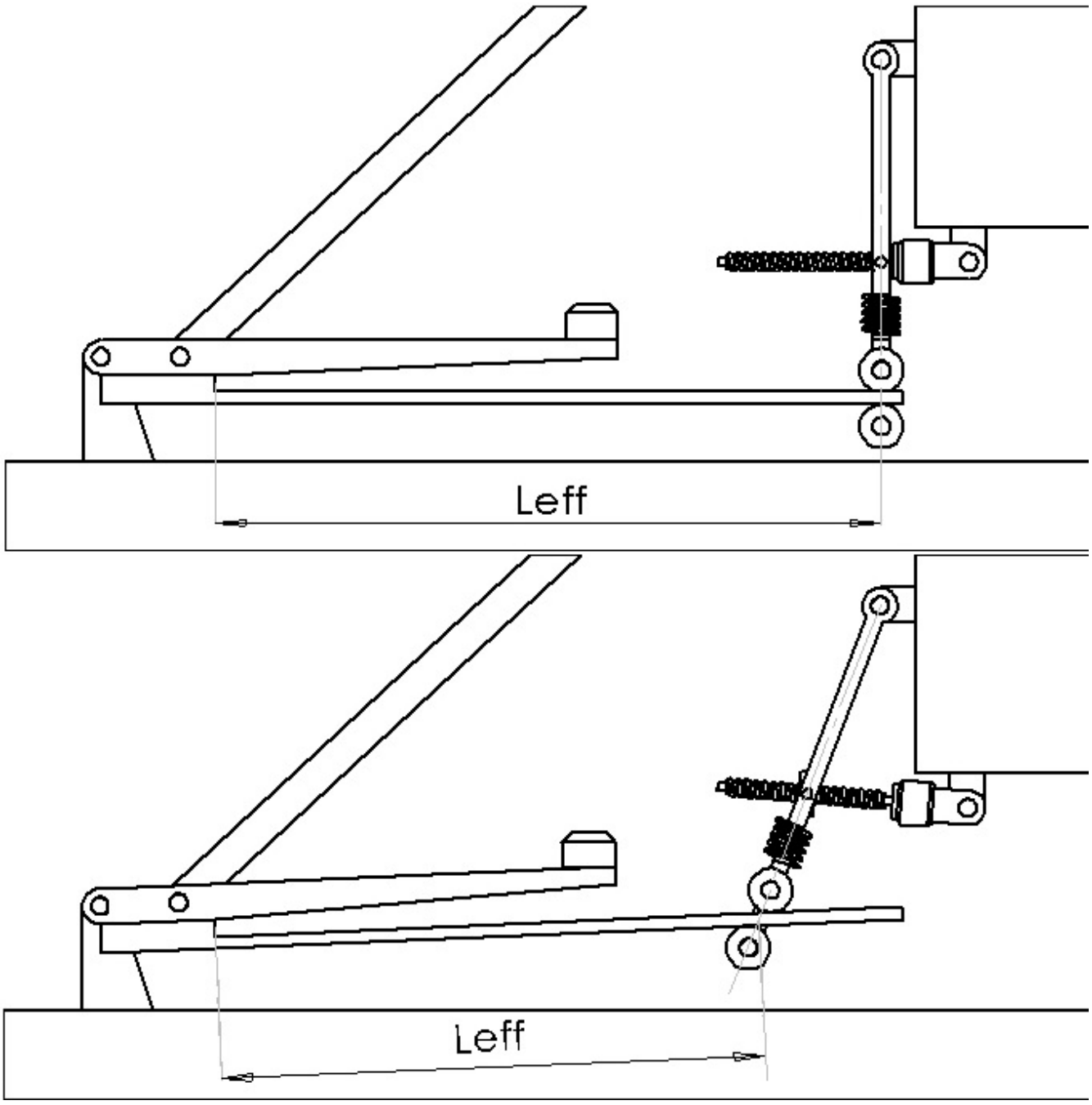

Figure 36: Mechanism for changing the effective stiffness of a leaf spring suspension

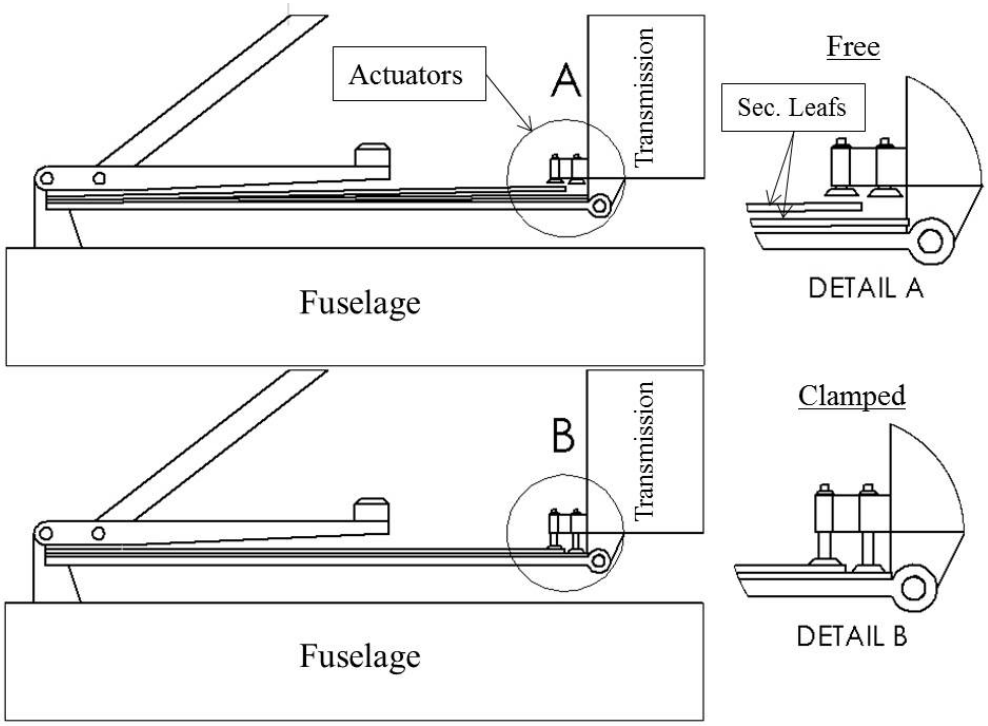

Figure 37: Multiple leaf spring stiffening system

4.2.3 Multiple leaf springs

Multiple leaf springs activated separately is another possible method for altering the stiffness, one example of such a system is shown in Figure 37.

Figure 37 shows a system where there are three leaf springs in total, the main leaf spring is permanently engaged while two other sub-springs with stiffnesses of 19 and 21% of the main spring, as calculated in the feasibility study, are activated via some actuator. This will allow a leaf spring suspension with three distinct stiffnesses depending on whether no, one or both sub-springs are active.

These three stiffnesses will tune the system to isolate the vibration at the three distinct frequencies required. Shown in the figure is the free and clamped states of the leaf springs, in the free state (Detail A) both actuators are disengaged and only the main leaf is active, actuators clamp (Detail B) their respective secondary leaf springs to the main leaf spring increasing the stiffness of the suspension.

One positive aspect of this system compared to the concepts in Sections 4.2.1 and 4.2.2 is that the system has three distinct operating settings corresponding to the three distinct rotor speeds. This means that the need for feedback control is not required and a much simpler control scheme. Alternatively a pure mechanical system can be devised to actuate the springs for the different settings, lowering the complexity of the system. Furthermore this is a simple robust design with quick response to the rotor speed change.

Negative aspects of this system is that unclasped secondary leaf springs can vibrate freely and cause a lot of noise. This is also a heavy design with 8 actuators in total and extra material required for the secondary leaf springs.

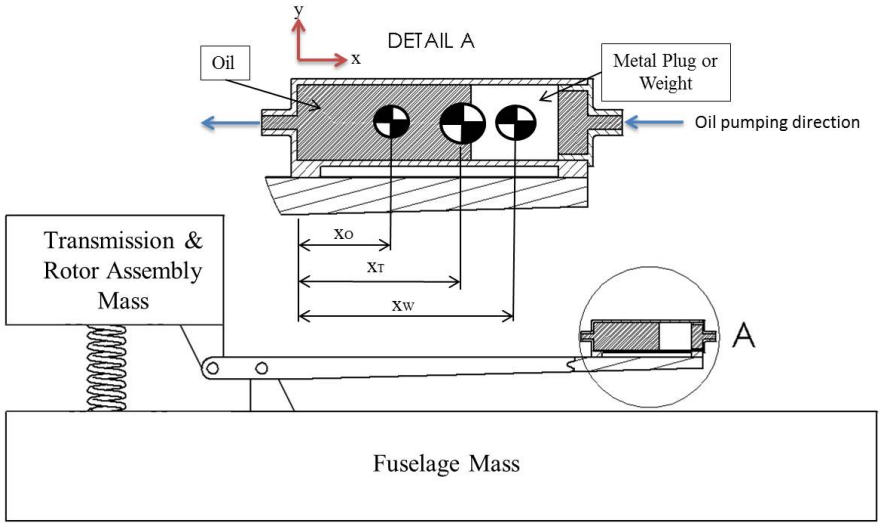

Figure 38: Pendulum mass shifted by using hydraulics

4.3 Varying tuning bar length ratio Q_R

Referring to Section 3.1 and Figure 8 the length ratio is defined as $Q_R = \frac{R}{r}$, and the ratio Q_R can be varied by changing the distance between the fuselage hinge and the centre of mass of the pendulum (R) or by changing the distance between the fuselage hinge and the pendulum arm hinge (r). Concepts of both types will be discussed next.

4.3.1 Changing pendulum length R

The length of R can be changed by shifting the pendulum mass along the length of the pendulum arm, hereby follows a few concepts in which this can be accomplished.

Hydraulic shifting mass

A concentrated mass can be shifted along the length of the pendulum using hydraulics as seen in Figure 38.

The figure shows a metal plug inside a hydraulic cylinder filled with hydraulic oil, the plug has a snug fit inside the hydraulic cylinder and pumping the oil in one direction will cause the plug to move in said direction. Also shown are distances x_O, x_T and x_W which are the centre of gravity position for the body of oil, the mechanism as a whole and the weight respectively.

The distance R is defined by the centre of gravity of the whole system x_T which will shift left and right following the plug. As discussed at the end of Section 3.1.3, the mass of the pendulum arm, hydraulic housing and fluid should be as low as possible in comparison to the concentrated moving mass or plug, for the most effective change in x_T or R per distance of moving the weight.

An infinite tuning range, no loose parts and a robust design are a few positive aspects of this design. Some negative aspects include requiring feedback control, possible oil leaks, high maintenance, heavy design and slow reaction time to frequency change.

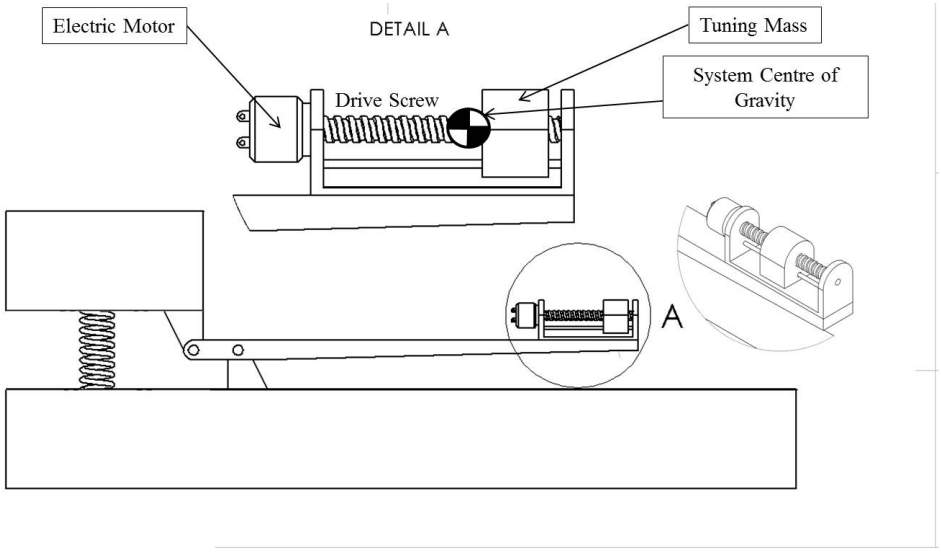

Figure 39: Pendulum mass shifted by using a drive screw

Screw driven mass

Working on the same principle as the previous system but using a drive screw to move the weight.

Similarly to the hydraulic system the distance R, in this case the distance from the first hinge to the system centre of gravity shown in Figure 39, is shortened or lengthened by shifting a weight along the length of the pendulum arm via a drive screw and electric motor. This will change the ratio Q_R and tune the system to different frequencies. A guiding rod is required with this system to stop the mass rotating about the drive screw when the mass is being shifted. This system will have a much faster response than its hydraulic counterpart as well as a simpler design with fewer parts whilst also having an infinite tuning range.

On the other hand screw drives are sensitive to dust and debris, causing them to seize, increasing maintenance and lowering the robustness of this design. The mass is also loose on the screw drive and will be free to vibrate unless constrained with a clamping mechanism, a feedback control system will also be needed for tuning purposes.

Solenoid driven shifting mass

The final concept for shifting the mass is through solenoids.

Figure 40 shows a concept that shifts the pendulum mass along the length of the pendulum arm using a set of solenoids connected in series, $d1$, $d2$ and $d3$ show the shift of the effective CG mass of the pendulum weight in three distinct configurations of extended and/or contracted solenoid states.

This system has three distinct vibrations isolation frequencies depending on the mentioned solenoid configurations, and has the ability to quickly switch between configurations via the extension or contraction of the solenoids. Practically a very robust and maintenance light implementation as solenoids are reliable, inexpensive, robust and easy to replace if maintenance is required.

4.3.2 Changing the hinge distance r

Alternatively the ratio Q_R can be altered by changing the distance between the hinges r as shown in Section 3.1 and Figure 8.

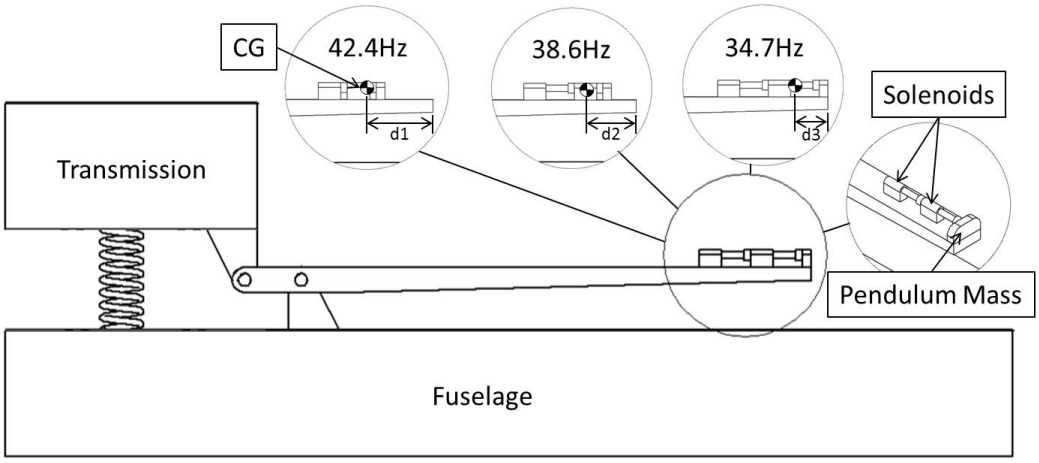

Figure 40: Pendulum mass shifted by using solenoids

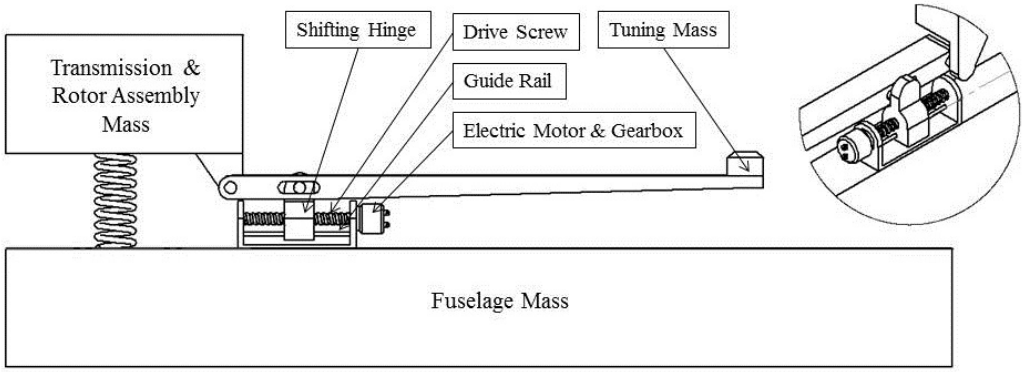

Figure 41: Shifting hinge using a power screw

Shifting hinge power screw

The distance between the hinges can be altered by using a power screw to shift the hinge along the length of the pendulum arm.

Figure 41 shows a concept for shifting the hinge position using a power screw with an electric motor, this will directly alter Q_R by changing the distance between the hinge points r and therefore tune the system to the desired frequency.

Positive benefits of tuning the system in this way compared to shifting the pendulum mass as discussed in Section 4.3.1, is that shifting the hinge point by a unit length, directly changes r by that amount,whereas, shifting the pendulum mass by a unit length only changes R a fraction of the distance moved, depending on the weight of the pendulum mass compared to the pendulum arm and actuation mechanism. In other words, a much smaller shift in the hinge position is required compared to that of the pendulum mass to achieve the same degree of tuning.

This system also has an infinite tuning range and a relatively simple design. Negative attributes are the power screw's intolerance to dust and debris, subsequently extra maintenance will be required. This system will also

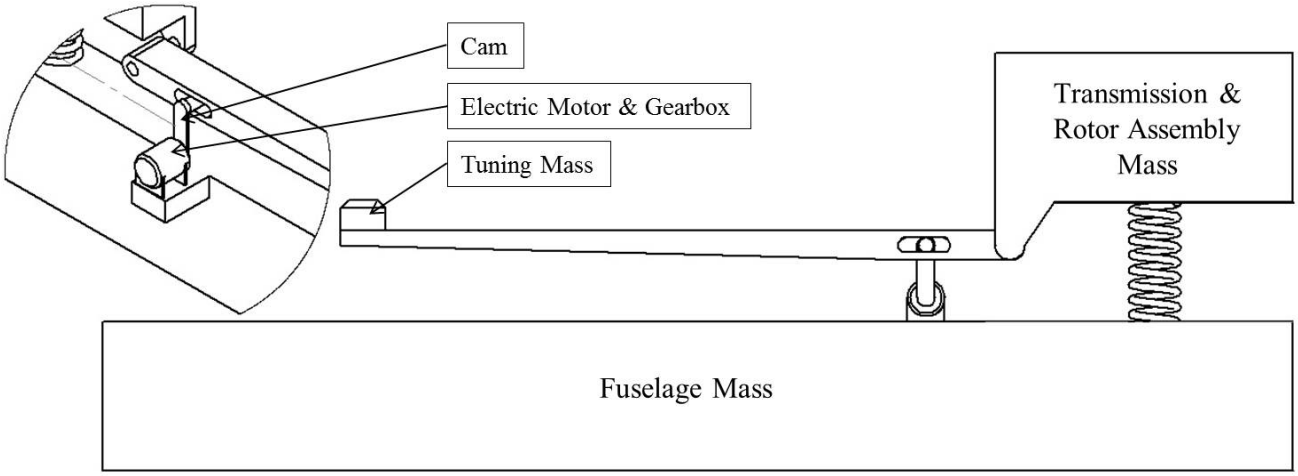

Figure 42: Shifting hinge using a cam

require feedback control and will have loose fitting parts like the shifting hinge that will adversely effect the isolator performance, unless a clamping mechanism is also introduced to clamp the shifting hinge every time it is in the desired location, adding complexity and weight to the design.

Shifting hinge cam

Similarly to the power screw concept the ratio Q_R is changed by shifting the the hinge location, however, a Cam is used instead of a power screw as seen in Figure 42.

This concept has an infinite tuning range and a relatively simple and robust design. Similarly to its sister concept it is sensitive to dust and debris but to a lesser extent because there is no exposed power screw. Furthermore, creating a sliding pin joint with high tolerance is difficult and expensive and a degree of looseness is to be expected which in turn degrades the isolator performance, unless a clamping mechanism is introduced which increases mass, complexity and cost.

The design most likely requires an electrical motor with a gearbox and a control system to drive the Cam, this ads considerable weight and complexity plus increased maintenance requirements. All things considered this design seems superior to its power screw counterpart.

4.4 Changing the dynamic characteristics

By using multiple spring and mass systems it is possible to change the dynamic characteristics of the isolation system to alleviate vibrations at multiple frequencies.

Figure 43 shows one such concept, there are three masses in total, mass $m1$ is fixed and makes up the body of the mechanism, masses $m2$ and $m3$ are floating masses that slide freely in channels. Low stiffness springs are used to secure the free sliding masses in their respective channels and solenoids or some other mechanisms are used to lock the floating masses in place depending on the isolation frequency required.

This will allow for 3 distinct frequencies of vibration attenuation, however the free sliding mass springs cannot be too soft as to allow the masses to hit the end of the channels during operation as this will cause non-linear

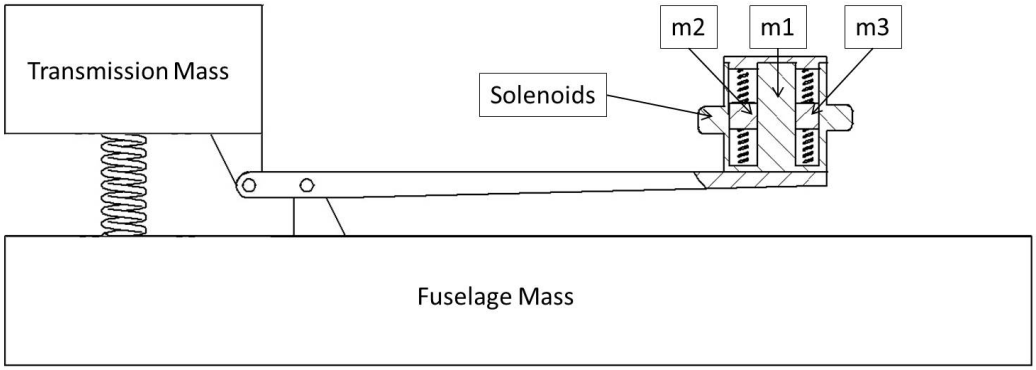

Figure 43: Change dynamic characteristics

behaviour of the vibration isolation system. Stiffer springs will on the other hand require larger sliding masses to achieve vibration isolation at the desired frequencies.

Clearly this design is not trivial and would require multiple iterations and analyses to achieve the required results, including the use of actuators and other mechanisms to achieve a feasible robust working system. A lot of moving parts and a system for controlling said actuators will also be required, further complicating the design and introducing more elements of maintenance in the systems life cycle. A simple circuit can be set up to actuate the masses that will be coupled with the speed control system of the helicopter main rotor, as each rotor speed correspond directly to a distinct configuration of clamped or unclasped masses.

4.5 Concepts conclusion

Shifting the mass on the pendulum arm similar to concepts shown in Sections 4.3.1 seems to be the most practical, robust and easy to manufacture, at least with respect to the available resources for this dissertation. That is not to say that other concepts are not more desirable for actual production helicopters, however, simplistic and robust solutions are most likely to be sought for any production helicopter. The shifting of the pendulum mass is chosen to be the subject of further study for this dissertation. The stiffness between the transmission and the fuselage will be provided by a leaf spring system similar to that depicted in Figure 33. Unlike the concept shown in Section 4.3.1, a single mass will be moved and clamped in between experimental tests as a proof of concept, as developing a full system that shifts the pendulum mass is outside the scope of this dissertation.

My engineering intuition tells me that a system as shown in Section 4.3.1 would be a prime candidate for development of production tunable antiresonance vibration isolator. The system is small, simple, robust and easy to implement relative to the other concepts.

5 Design and fabrication of prototype

This chapter discusses the fabrication of the first prototype and all components it is comprised of.

5.1 Vibration isolation system

Figure 44 shows a diagram of the tunable vibration isolation system that is designed and fabricated for this dissertation. It is almost identical to the system described in the introduction of Section 4 except that the tip of the leaf spring is attached to the fuselage as opposed to the transmission and this system has a diaphragm plate and a moveable pendulum mass. In conventional helicopters the diaphragm plate is designed to provide the gearbox casing reaction torque whilst being relatively elastic in the vertical or heave direction. Although there is no rotor torque in the experiment done in this work, the diaphragm is still required to locate and secure the bottom of the transmission, and is especially designed to add as little vertical stiffness to the overall system as possible.

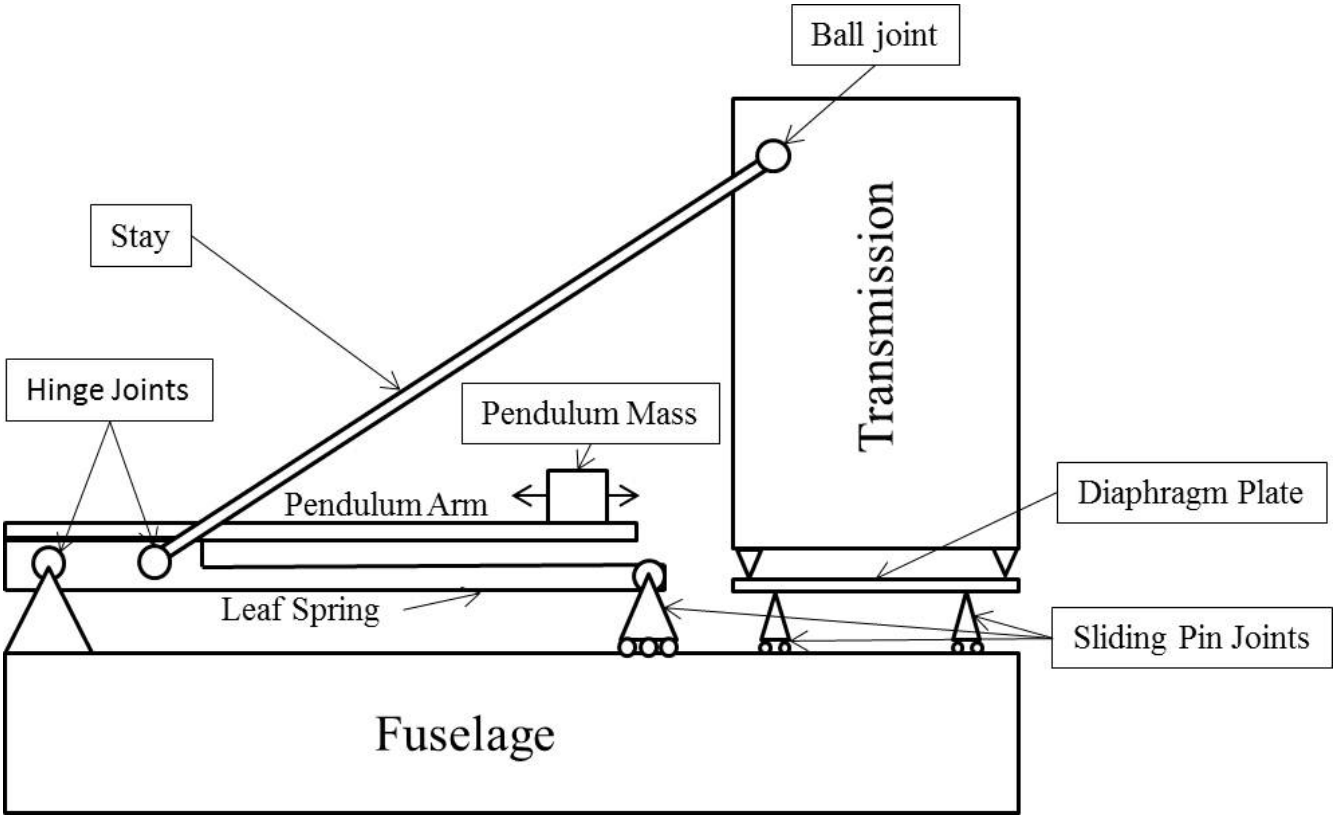

Figure 44: Tunable vibration isolation system diagram

5.1.1 Leaf spring design

The client of the proposed UAV helicopter suggested that their $5mm$ deflection, between transmission and fuselage, under $2.8G$ loading specification for their $6ton$ attack helicopter be scaled with regards to mass as a stiffness specification for the UAV helicopter. This corresponds to a $1.67mm$ deflection between the transmission and the fuselage of the UAV during a 2.8G manoeuvrer. Working with the estimated full up weight of the envisioned helicopter at $580kg$ under 3G static loading, the required stiffness for a $1.6mm$ deflection is calculated to be $10.6 \times$

$10^6 N/m$ or $10.6 kN/mm$. The diaphragm plate stiffness is assumed to be negligible in comparison to the total stiffness and is not considered in the design thereof.

Assuming that the total stiffness is made up with the four leaf springs, then each leaf spring has a stiffness of $2.62 \times 10^6 N/m$ ($2.62 kN/mm$). Since no analytical equations of tapered beams similar to the beam in question was found, a Matlab beam bending analysis program that calculates beams with multiple different cross sections is used. The tapered leaf spring is discretized into small beam lengths each with a constant cross section, but with different cross sections between concurrent elements, creating the approximation of a tapering beam.

A starting base width of $40mm$ is chosen, whilst the taper angle ensures a constant bending stress as the bending moment decreases, the thickness of the leaf spring is iterated until the deflection is roughly $1.67mm$ at the leaf spring to transmission stay joint. The stress in the beam is then checked to assure its below the allowable stress level for a high quality spring steel.

Figure 45 shows the plan view, shear, bending moment and the deflection diagrams of the final result after the iteration process[13, pp. 271 - 299, 607 - 611]. The fuselage hinge is situated at $0mm$ and the stay hinge is situated at $25mm$, the deflection at the stay hinge is measured at each iteration until the $1.6mm$ deflection criterion is met. Note that up to $50mm$ in length the spring has a constant $40mm$ width and a $30mm$ thickness, which houses the pins for the stay and fuselage hinges. The $4.9mm$ spring thickness refers to the tapered section of the spring.

The spring in the figure has a constant thickness of $4.9mm$, and constant bending stress of $770MPa$ across the tapered length when a 3G static load is applied. This stress level is acceptable for most high tensile spring steels, which usually have yield stresses of $1000MPa$ and above.

The spring is accurately modelled in SolidWorks incorporating the pin holes for the required hinges and a pocket for the stay rod end, the model is then imported into SimXpert and finite element analysis is done to verify the results obtained by the Matlab beam analysis program discussed previously.

The leaf spring finite element model consists of 25787 parabolic tetrahedra solid elements (CTETRA 10) with 10 nodes per element giving the system 251256 degrees of freedom. An element size of $2.5mm$ ensures at least two elements or 5 nodes (because the elements are higher order parabolic) through the thickness of the leaf spring.

Figure 46 shows the results of the finite element analysis, the tapered section of the spring shows a uniform constant stress as was the intended design philosophy.

Furthermore the deflection at the stay hinge given by the FEM analysis is $1.625mm$ which is within 2.5% of the $1.67mm$ designed deflection, with a Von Mises stress of $536MPa$ across the tapered length of the spring. A Modal Neutral File of the spring is created using SimXpert with free-free boundary conditions that can be imported, constrained and used as a flexible body directly in the ADAMS model.

The FEM model is constrained with the tip on a sliding ball joint and the first hinge on a pin joint, a modal analysis is then completed on the leaf spring to ensure that its natural frequencies do not lie within the test frequency range, as this may lead to unexpected behaviour.

Figure 47 shows first and second natural modes of vibration for the leaf spring, with the first mode at $199Hz$ and the second at $894Hz$. With the first and slowest mode at more than 4 times our highest frequency of interest, it is clear that the natural frequencies will not have an effect on the test results within the test frequency range.

5.1.2 Pendulum arm design

The pendulum arm was designed to be as light and as stiff as possible for the available design space. A height of $10mm$ is chosen to ensure a compact and low profile design for the vibration isolation system assembly. A width of $40mm$ is chosen so that the pendulum arm can easily be fitted to the leaf spring. The pendulum arm is made as long

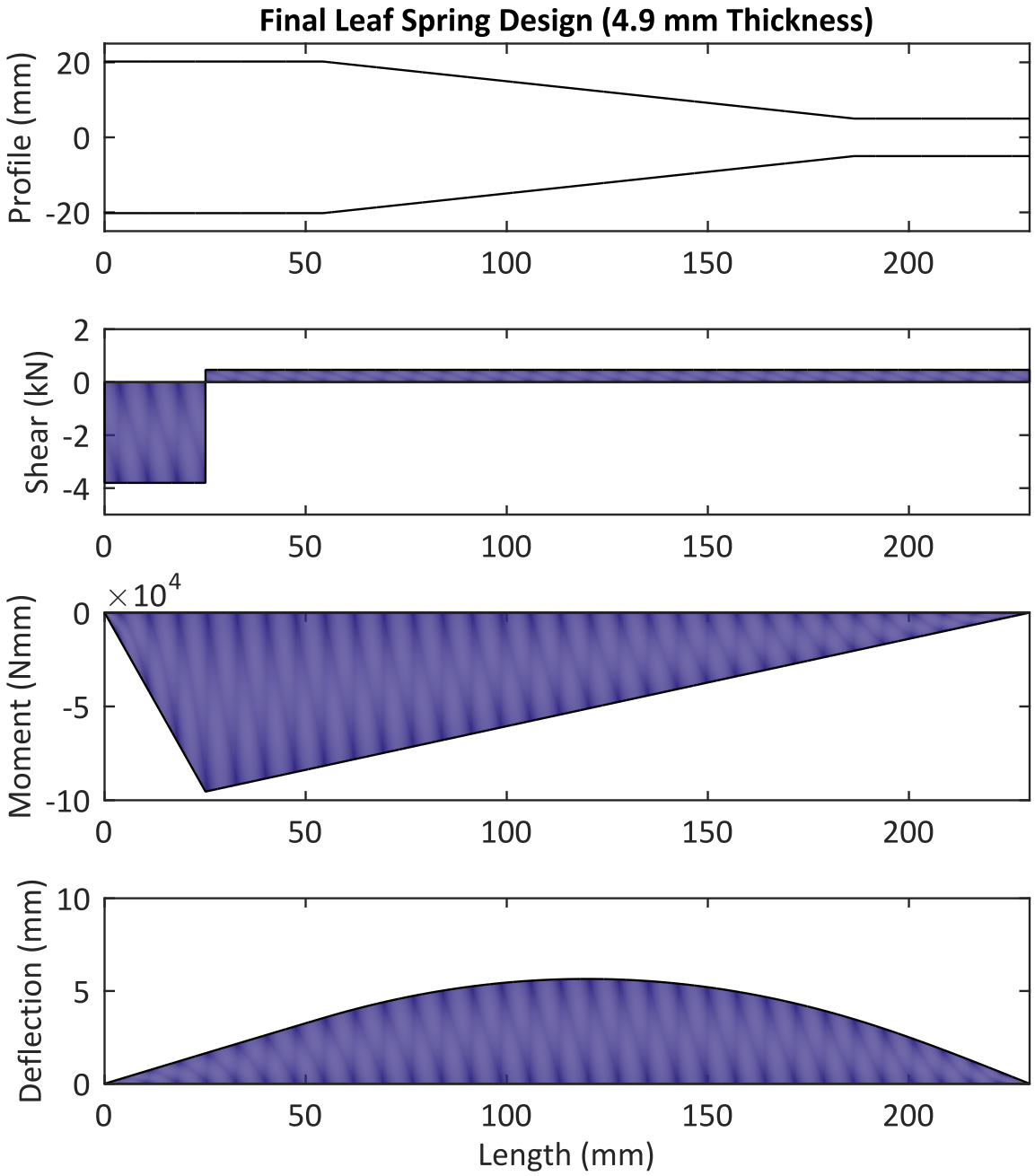

Figure 45: Leaf spring analysis

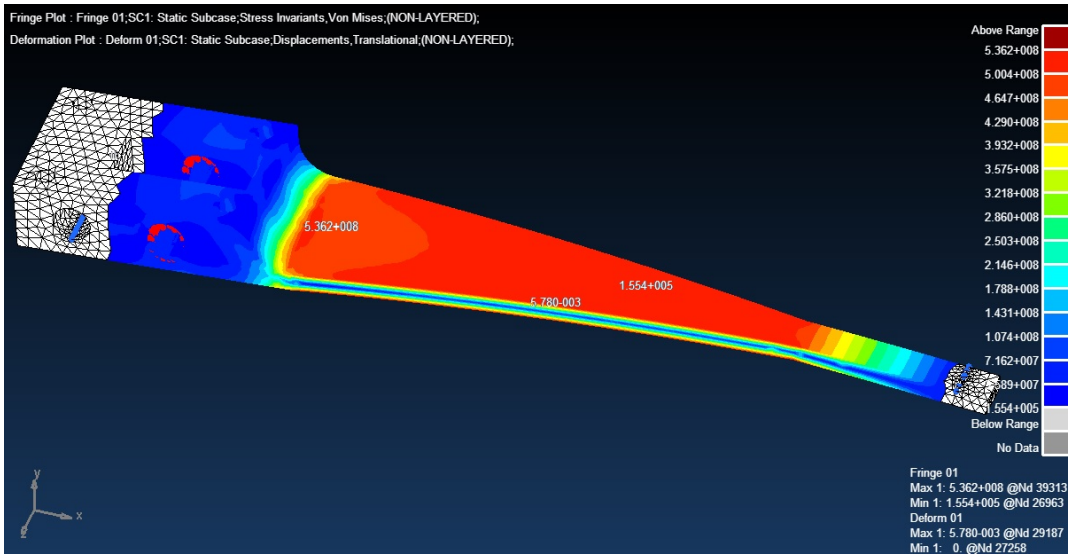

Figure 46: Leaf spring FEA static deflection analysis

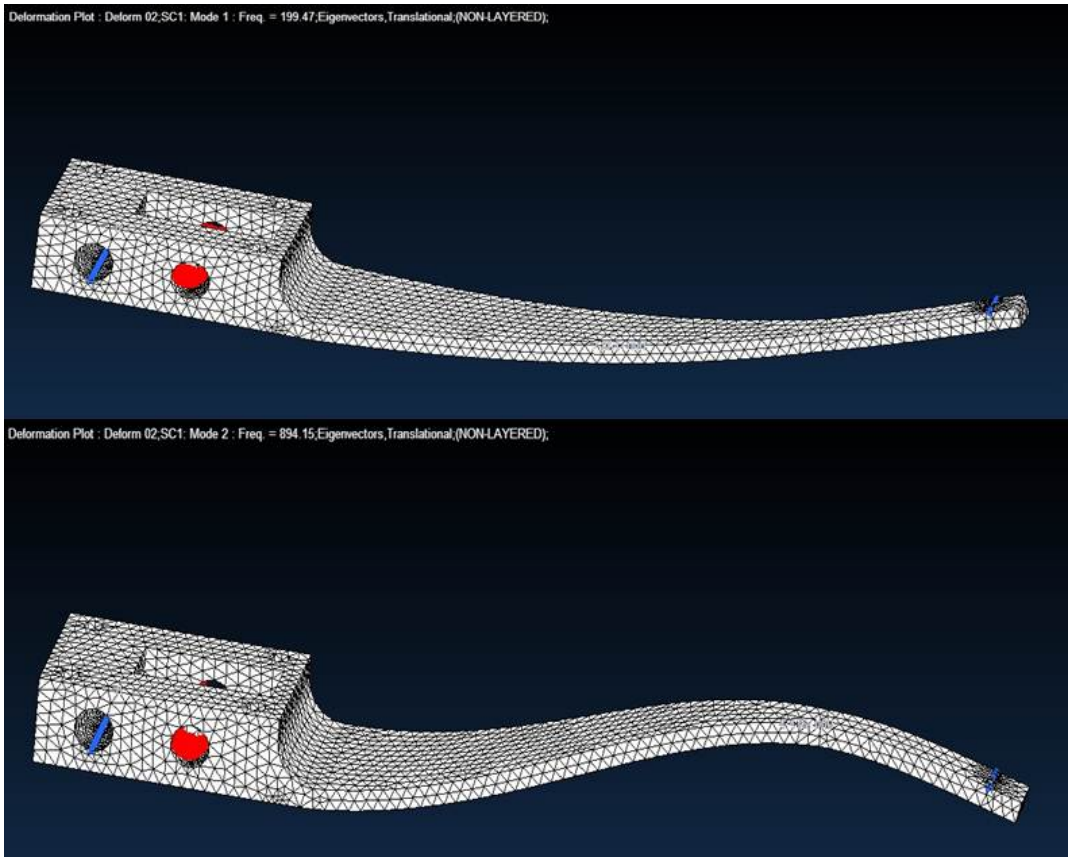

Figure 47: First two mode shapes of leaf spring

as possible within the design space to ensure as large as possible pendulum arm ratios Q_R which in turn minimizes the mass requirement of the pendulum sliding mass.

Two through slots are machined in the centre of the pendulum arm, the first allows the stay to reach the stay pin the second is the guide for the pendulum mass, the length of the guide slot is determined by the shifting length required to alleviate vibration at the design frequencies. Blind slots are machined throughout the pendulum arm to reduce weight whilst having minimum impact on its bending stiffness. Four small bolts secure the pendulum arm to the leaf spring. Figure 48 shows the CAD model of the Pendulum Arm with all relevant geometry as discussed.

Due to the thin web features on the pendulum arm, a finite element model consisting of parabolic quadrilateral shell elements (CQUAD8) is created and used in a modal analysis to determine mode shape and frequencies of the pendulum arm. The modal analysis is to determine if any natural resonance frequencies of the pendulum arm are within the test frequency range.

The model has 5159 element with a total of 109440 degrees of freedom. Figure 49 shows the first three natural mode shapes and frequencies, the green lines show the elements and nodes that are fully fixed during the modal analysis and simulates the pendulum arm in its bolted down state.

Considering the first and slowest natural frequency of vibration at $204\,Hz$ is more than 4 times larger than the fastest test frequency of interest, the natural frequencies of vibrations for the pendulum arm is far removed from the test frequencies of interest and will not adversely affect the test results.

5.1.3 Pendulum mass design

The pendulum mass is designed to slide within the guide slot if the pendulum arm. It is designed to have a mass that can tune the vibration isolation system to alleviate vibration at the three design frequencies within the sliding range of the pendulum arm guide slot.

The pendulum mass also has a small bolted bar that acts as a clamp to ensure that the pendulum mass is secured to the pendulum arm during testing, see Figure 50. As the pendulum mass is just a compact dead weight no further analysis or FEA is required.

5.1.4 fabrication

The leaf springs are designed for $2.8G$ loading and maximum deflection specifications of small UAV helicopters, however the prototype was designed for this dissertation only and experimental loads do not exceed $1G$ plus vibration amplitudes, therefore all the parts were machined from mild steel as this was more than adequate for the experimental test loads. Solid models of all the vibration isolation system parts were sent to a machine shop and all parts were made with CNC milling machines from mild steel.

5.2 Dummy fuselage

5.2.1 First prototype design

At the time of designing the experiment there had not been an actual fuselage of the UAV to use, nor was there plans to have one finished by the time that testing would begin. A dummy fuselage is created to simulate the mass and inertia of the actual fuselage, and is the substitute for the actual fuselage.

The first dummy fuselage is designed to have its mass, centre of mass location, pitch, roll and yaw inertias identical to that of the UAV helicopter. Figure 51 shows the original concept for the design of the dummy fuselage.

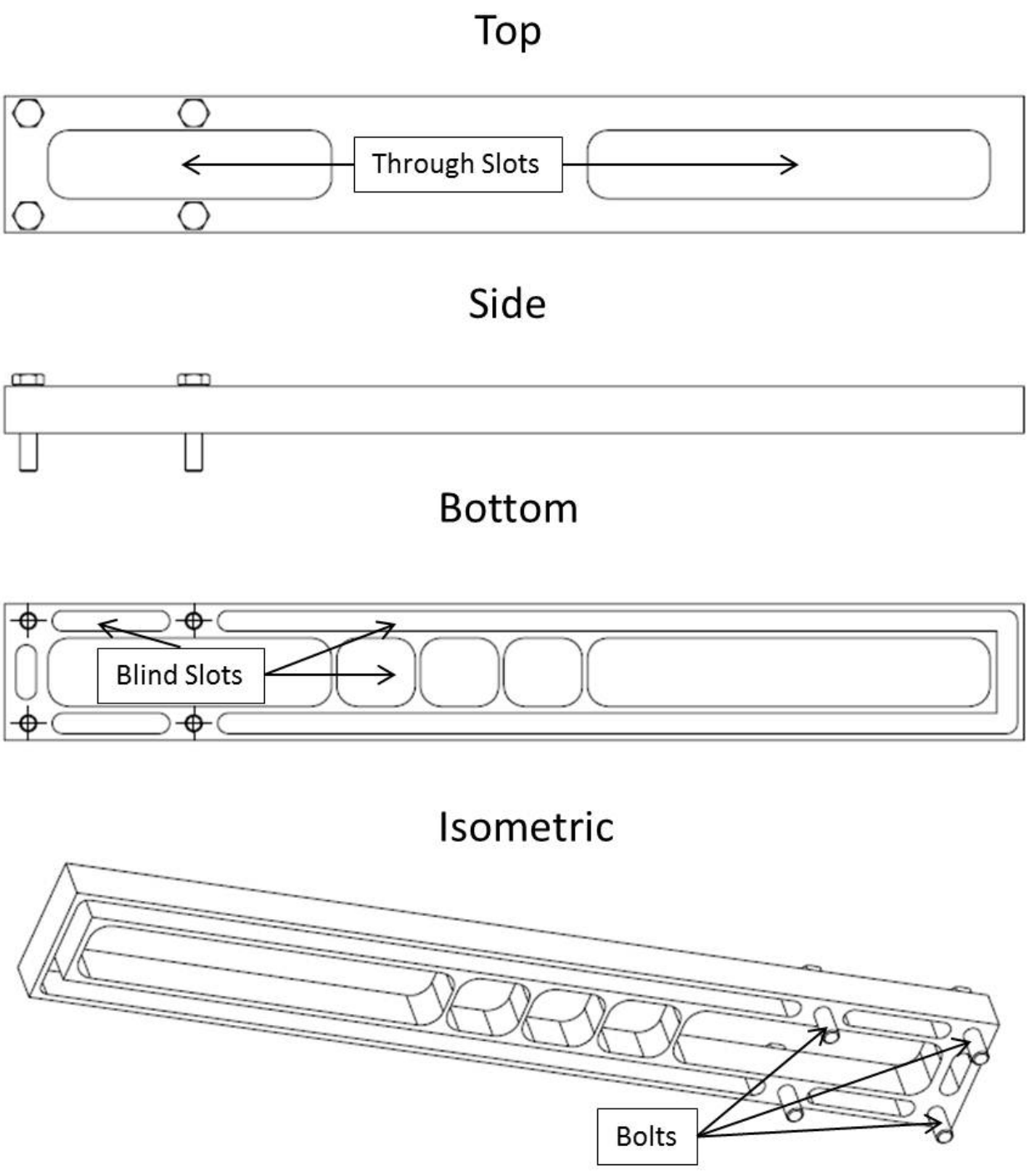

Figure 48: Pendulum CAD model

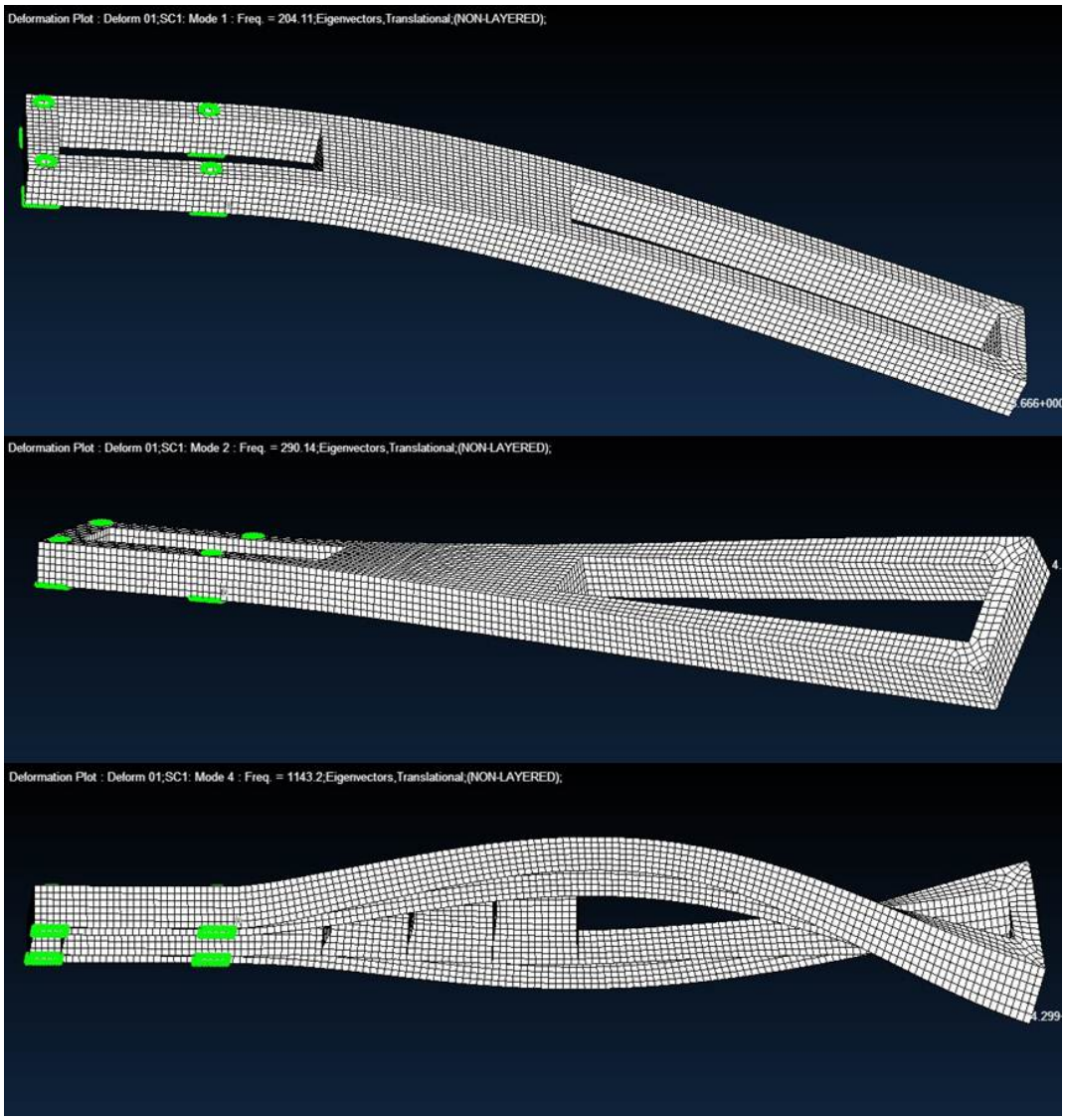

Figure 49: Pendulum arm mode shapes and frequencies

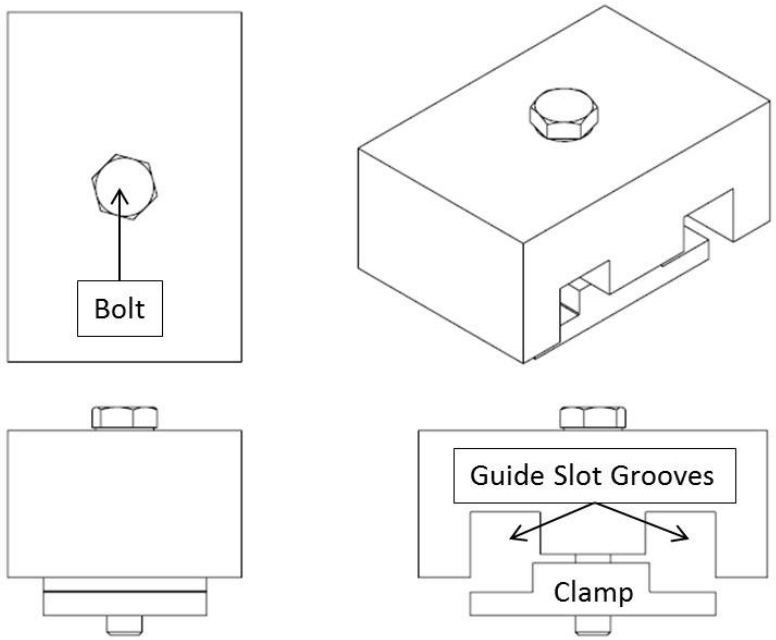

Figure 50: Pendulum mass CAD

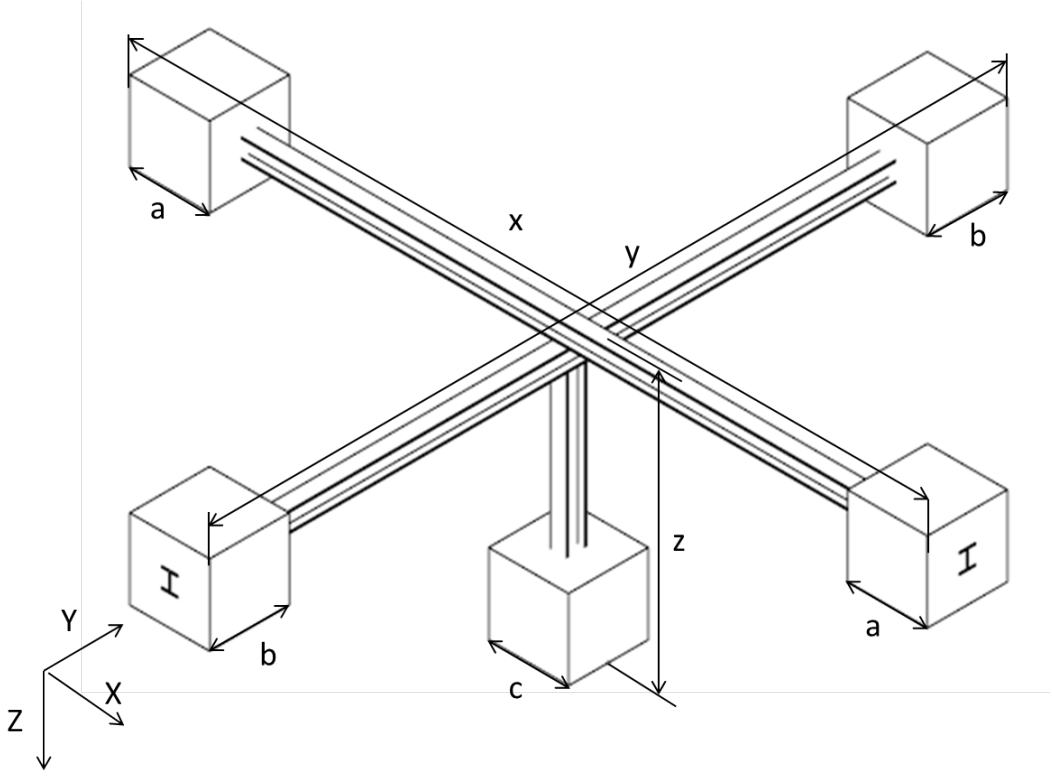

Figure 51: Development of first prototype

Adjusting the beam lengths x, y, z and the concrete cube side lengths a, b and c defines the mass and inertia properties of the dummy fuselage. There are 5 equations that are solved simultaneously, the pitch, roll and yaw inertias the mass equation and the centre of mass equation in terms of the 6 variables discussed earlier. The equations are non-linear and there are more variables than equations so a numerical solving technique is used.

A non-linear simultaneous equation solving technique using optimisation mathematics is utilised in Matlab to solve this problem[2]. All five equations are written in the form $F(\bar{x}) - S = 0$ where F is the equation in question $\bar{x}$ are the unknown variables and S is the known scalar value that we want $F(\bar{x})$ to equate to. The cost function of the optimisation problem is defined as:

$$F_C(\bar{x}) = (F_1(\bar{x}) - S_1)^2 + ... + (F_N(\bar{x}) - S_N)^2 \tag{30}$$

Where N is the total number of equations to be solved simultaneously. The cost function has a global minimum of 0 which is only achieved when all equations that are being squared also equates to 0. If a global minimum is found then a solution to the system of equations is also found. Although there are simultaneous non-linear equation solvers already available in Matlab, they can use non-feasible variable values, for example negative cube sizes, to determine solutions to the system of equations. The minimisation technique described has a powerful advantage, constraints are handled as part of the minimisation procedure, so constraints for this problem and variables are formulated, ensuring faster convergence to feasible solutions:

$$a, b, c, x, y, z \geqq 0 \tag{31}$$

$$z > CG \tag{32}$$

$$a > b \tag{33}$$

Constraint equation 31 is simply that all variables should be positive and feasible, constraint equation 32 is a logical assumption that the centre of gravity in the z direction lies within the length of the vertical beam z, constraint equation 33 is based on the fact that the pitch inertia of helicopters are more often than not much larger than roll inertia and therefore the side-length a of the concrete block contributing to the pitch inertia will be much larger than that of the block contributing to the roll inertia with side-length b.

It is found that the cube length of b is impractically small and therefore neglected and removed from the system of equation formulation. A solution to the set of non-linear equations are $a = 0.42m$, $b = 0m$, $c = 0.397m$, $x = 2.92m$, $y = 3.88m$ and $z = 0.626m$, for initial mass, centre of mass and inertia estimates of the UAV at $m_t = 573kg$ (total mass), $CG = 0.263m$ (centre of gravity), $I_y = 654kg.m^2$ (pitch inertia), $I_x = 116kg.m^2$ (roll inertia) and $I_z = 624kg.m^2$(yaw inertia).

Figure 51 does not have a frame or fastening fixtures for attaching the vibration isolation system, furthermore modal analysis for beam y shows that resonance in the test region of this beam is expected and therefore stiffening beams are added to the design. Figure 52 shows the completed first dummy fuselage design modelled in SolidWorks.

During experimental testing it is speculated that the first dummy fuselage has low frequency dynamics in the test frequency range of interest, and extensive stiffening modifications are designed in the form of lattice box frames as seen in Figure 53. For a more detailed discussion of all the experimental trials that led to the current frame seen in Figure 53 and eventual abandonment of the first dummy fuselage refer to Appendix A.3.

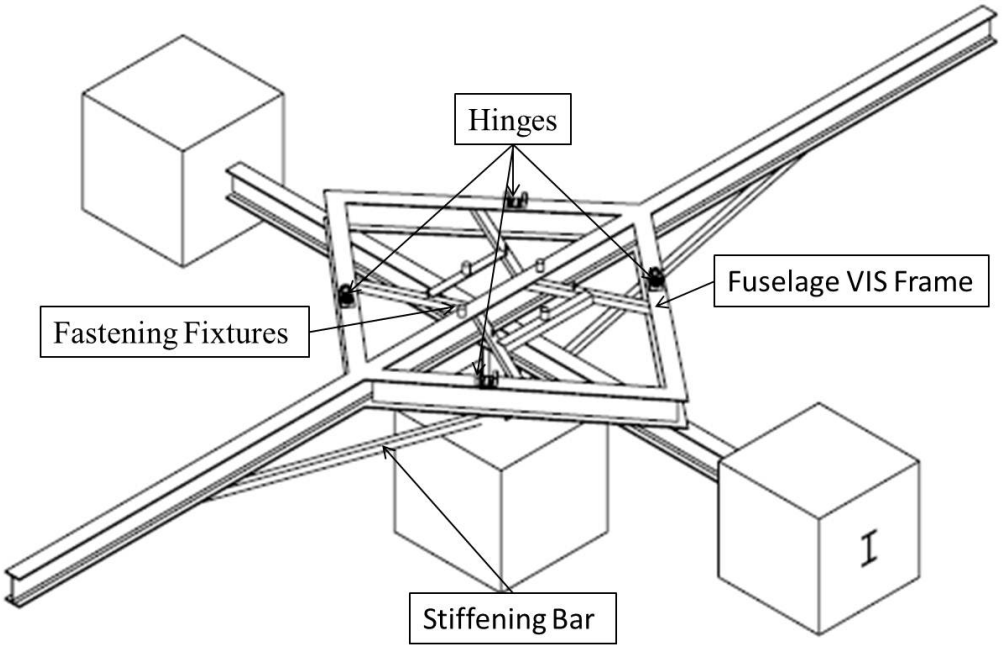

Figure 52: First prototype CAD model

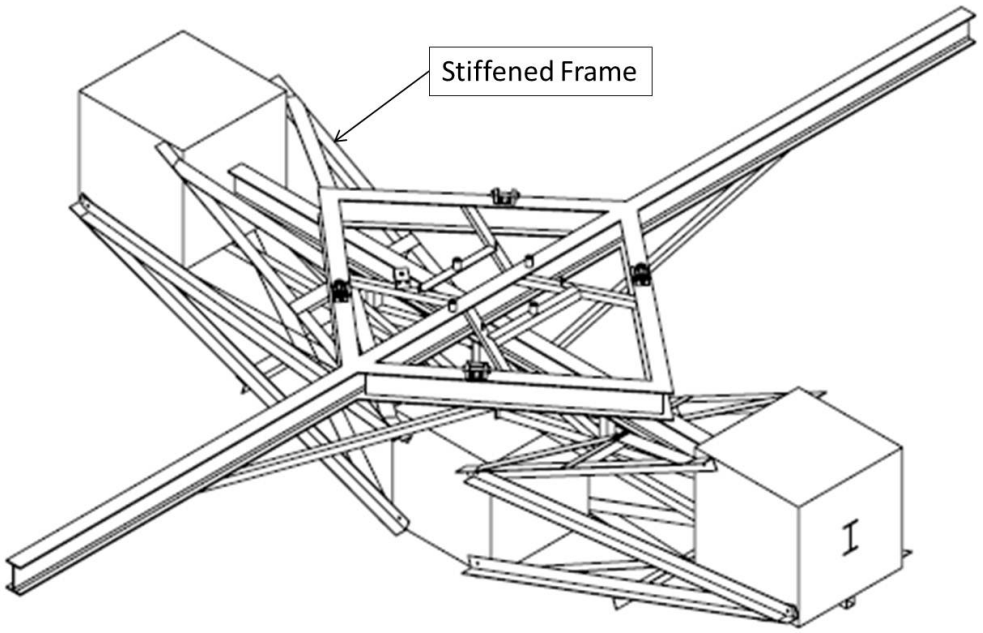

Figure 53: First prototype structural stiffening

Figure 54: First dummy fuselage, in a slightly modified form.

After stiffening, experimental results improve but are not conclusive. A simpler dummy fuselage is created that does not have the aforementioned stiffness issues, however this new dummy fuselage only simulates the actual fuselage in terms of mass, centre of mass and vertical heave inertia, this means that the effect of roll, pitch and yaw inertias cannot be simulated and tested.

5.2.2 First prototype fabrication

For a detailed chronology of the first prototype fabrication refer to Appendix A.2. The final stiffened first dummy fuselage but with the two extender I-beams removed, can be seen in Figure 54.

5.2.3 Final prototype design

The Dummy Fuselage is designed to have the same centre of gravity and mass as the actual helicopter fuselage, the centre of gravity for the prototype helicopter is estimated to be $263mm$ below the Vibration Isolation System deck. Therefore the dummy fuselage needs to be twice that in height to have the centre of mass at the desired depth. This defines the height of the concrete block to $526mm$, measuring the casting box plank thickness to be $17.8mm$ gives a total height of $543.8mm$ for the fuselage dummy mass.

Now that the height is defined, the width and length of the concrete box needs to be determined to ensure that the total volume of concrete creates a fuselage mass of $573kg$. Using the footprint of the fuselage hinges, the width and length is adjusted until the fuselage hinges all fit on the top of the concrete block and the concrete block has a mass of $573kg$ given an estimated concrete density of $2223kg/m^3$.

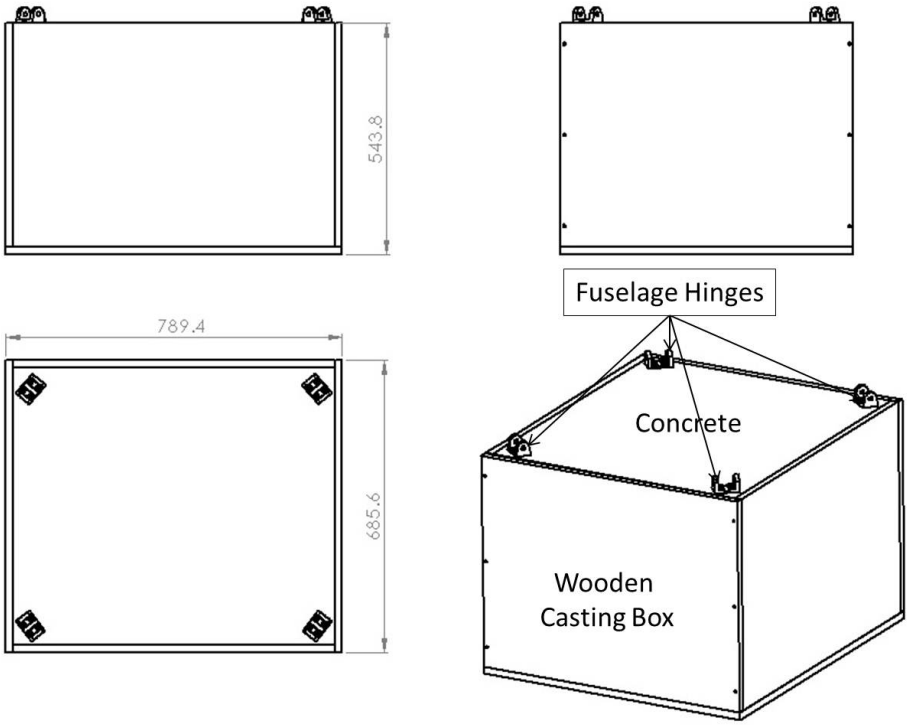

Figure 55: Dummy fuselage CAD

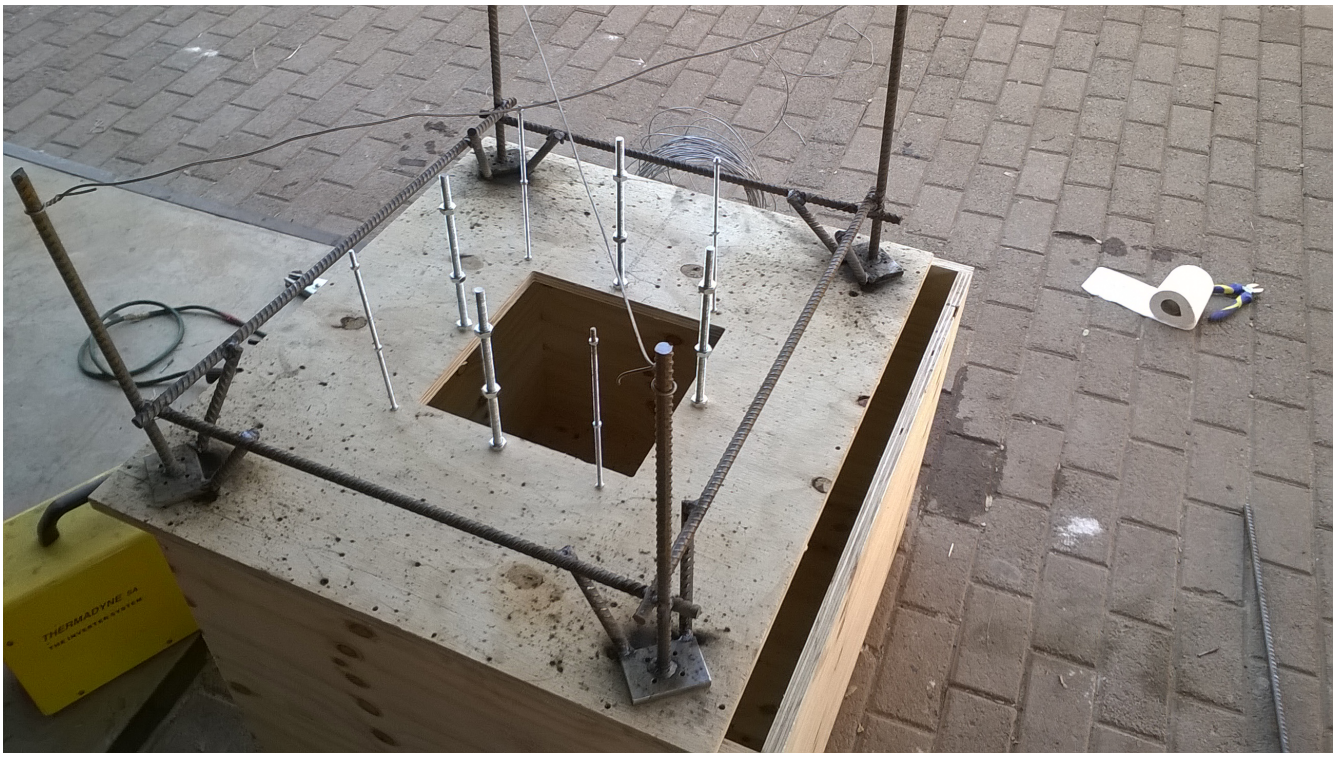

Figure 56: Dummy fuselage cast box and reinforcing (with the casing box top panel inverted)

Figure 55 shows the final dimensions of the Dummy Fuselage, note that the fuselage hinges just manage to fit on top of the dummy fuselage concrete block.

5.2.4 Final prototype fabrication

The casting box panels of the dummy fuselage is machined with a CNC wood router and assembled with wood screws, holes are also machined into the top panel where the various parts of the vibration isolation system attaches to the dummy fuselage.

Four plates are created onto which the fuselage hinges will be bolted, these plates are screwed onto the top panel of the casting box ensuring their correct placement. A rebar structure is welded from these plates, connecting them and creating a steel structure that keeps the concrete together. Threaded rods are bolted into the top panel that will later serve as attachment points for the leaf spring tips and the diaphragm plate respectively. Figure 56 shows the top panel on its back with the rebar and threaded rods inserted as discussed.

The top panel is then screwed onto the casting box and the box filled with concrete through the centre hole of the top panel; see Figure 57. The concrete is left for two weeks to cure, after which the top panel is removed as seen in Figure 58.

Figure 58 shows the finished dummy fuselage with the fuselage hinges bolted on and the studs for the leaf spring tips and diaphragm plate protruding from the concrete.

Figure 57: Dummy fuselage cast concrete

Figure 58: Completed dummy fuselage

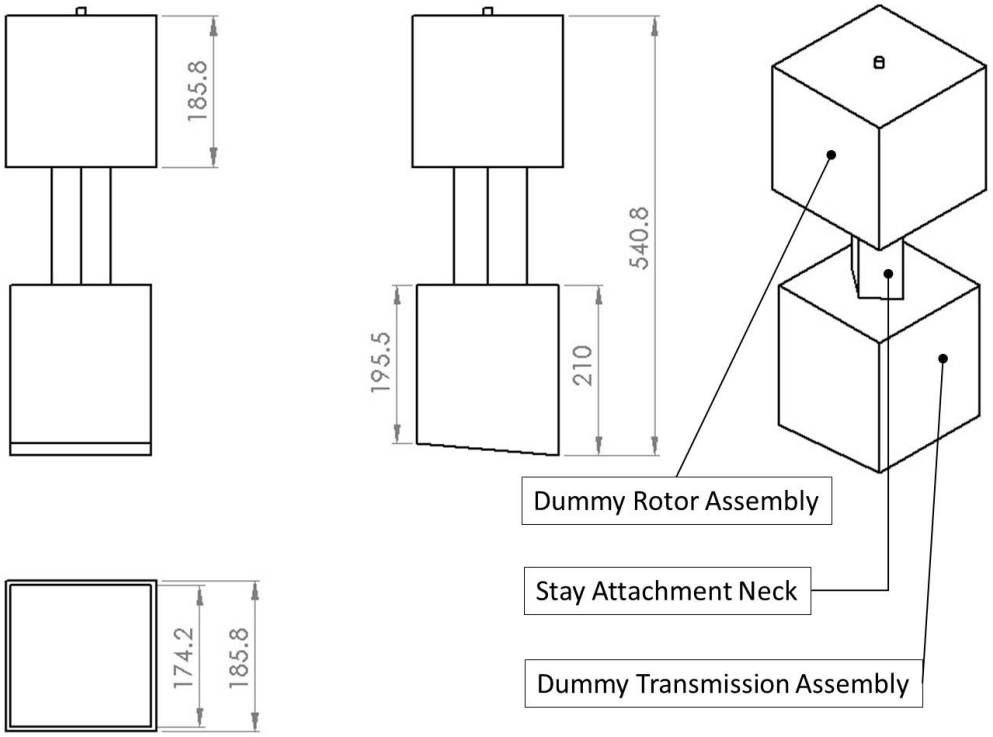

Figure 59: Dummy transmission and rotor mass prototype I

5.3 Dummy transmission and rotor head

5.3.1 Design

The transmission and rotor head is designed to have masses of 16.48kg and 15.4kg respectively in accordance to best estimates of the prototype helicopter. Concrete blocks with the correct masses are calculated, connected by a steel neck onto which the transmission hinges will be bolted; see Figure 59.

Figure 59 shows the CAD model for the dummy transmission and rotor head assembly. During tests both the transmission and rotor head dummy concrete blocks either broke or cracked, a cage was designed to clamp the transmission concrete block together and stop further cracking while the rotor head dummy concrete mass was completely removed and replaced with large round bar steel pieces of equal mass.

The top of the rotor head was further modified with a bar so that the dummy helicopter can be suspended from said bar and excited in the centre as opposed to the original setup where the dummy helicopter was suspended from the centre of the rotor head and excited off centre. Figure 60 shows all modifications to the transmission and rotor head assembly.

5.3.2 fabrication

Casting boxes are machined with a CNC router and assembled with wood screws, a metal spine is created that joins the Transmission and Rotor Head dummy masses and ensures that the load path goes through the spine and directly to the stays so that the concrete never takes any load and purely acts a dead weights.

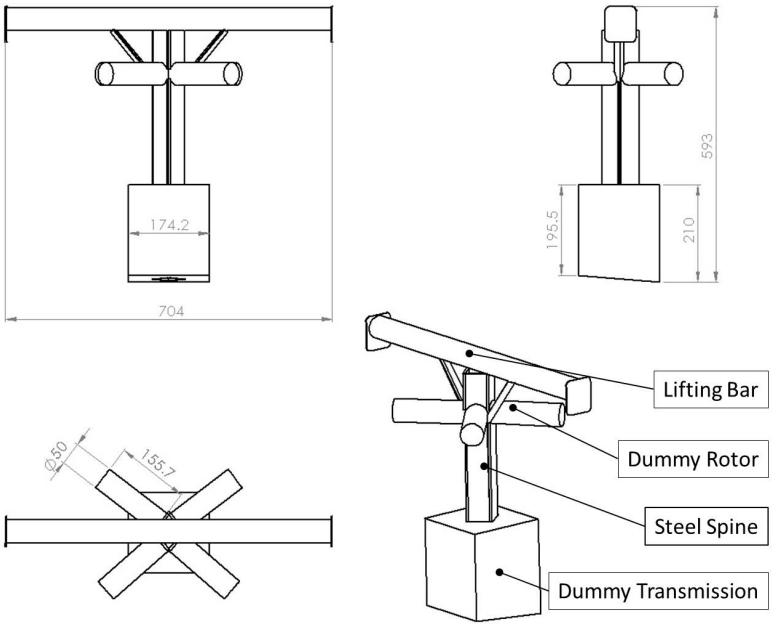

Figure 60: Dummy transmission and rotor mass prototype II

Figure 61: Dummy transmission building materials

Figure 61 shows all the building materials for the dummy transmission and rotor head assembly, except the casting box for the rotor head which is added later. Note that the transmission casting box has a metal cage inside that is connected to 4 bolts coming out the bottom to which the diaphragm plate is connected. This cage ensures that the concrete structure is held together and that the diaphragm bolts are secured within the concrete.

To the right of the transmission casting box is the spine or neck of the assembly with the transmission hinge studs already welded onto the spine and protruding from the neck casting box. Concrete is cast in the transmission box, the spine is then inserted and screwed to the box, finally the rotor head casting box is screwed to the neck box and filled with concrete.

Figure 62 shows the final result, the concrete is left to cure after which all the wood is removed and the concrete painted as seen in Figure 63.

After the transmission and rotor head masses cracked or broke the modifications are made as discussed in Section 5.3.1 and the final transmission and rotor head assembly is shown in Figure 64.

5.4 Final prototype assembly

5.4.1 Design

All the previously mentioned parts were designed around the prototype helicopter transmission to fuselage interface geometry, so all the parts are assembled as shown in Figure 65 with the correct stay lengths that are made from 10*mm* threaded rod, with rod end bearings at each end.

5.4.2 Fabrication

The dummy helicopter is assembled as follows. Each of the four stay assemblies are assembled as shown in Figure 66 and levelled using a spirit level. Note that the leaf spring tips are bolted to their respective studs that are cured within the concrete and that the pendulum sliding masses are not required at this stage in the assembly and will only be attached to the pendulum arms during testing.

The transmission and rotor head assembly with the stays already attached, as seen in Figure 67, are lowered onto the dummy fuselage with the diaphragm plate and stays attached to the fuselage and spring hinges respectively.

Figure 68 shows the complete prototype Dummy Helicopter.

Figure 62: Cast dummy transmission

Figure 63: Completed dummy transmission prototype I

Figure 64: Completed dummy transmission prototype II

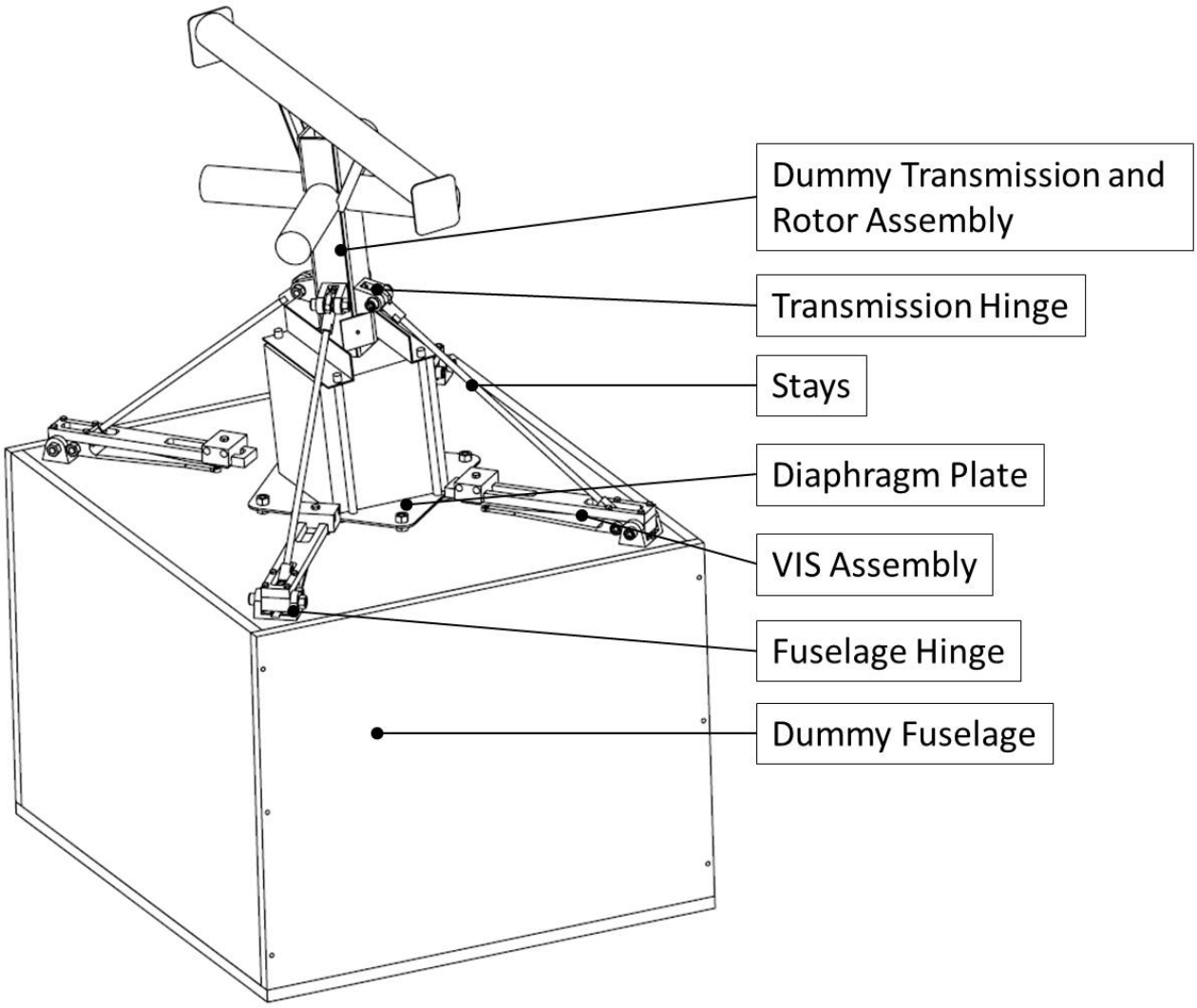

Figure 65: Prototype assembly

Figure 66: Vibration isolation system assembly attached to dummy fuselage

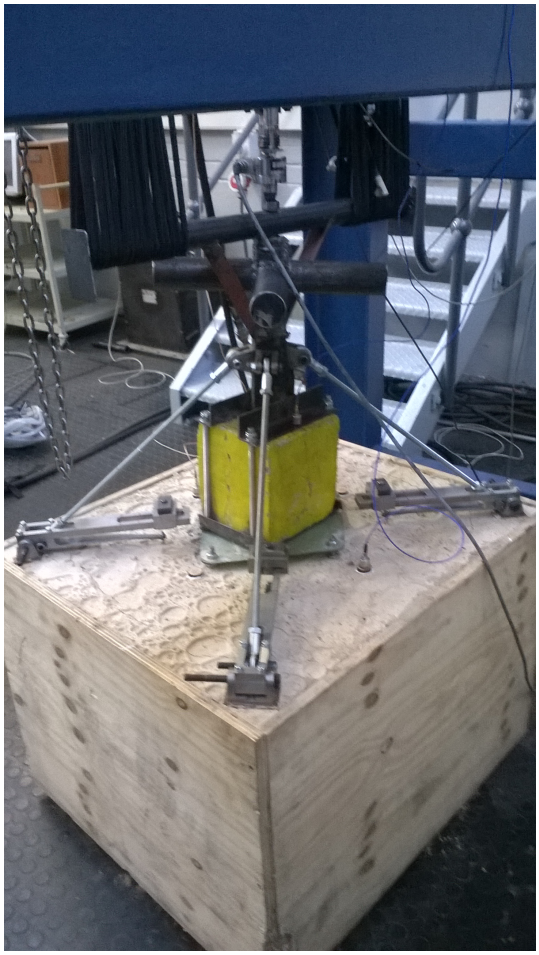

Figure 68: Finished prototype

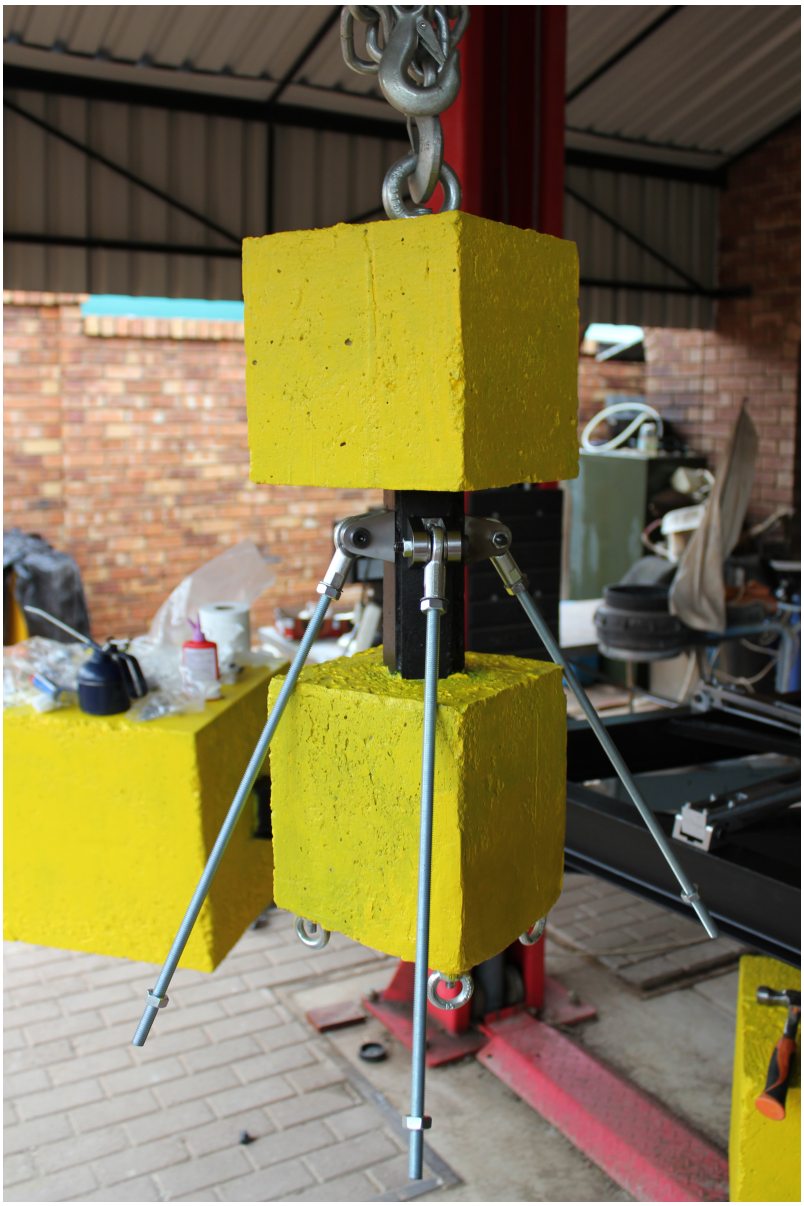

Figure 67: Dummy transmission attachments

6 Experimental evaluation of the vibration isolation system

For an accurate representation of real life flight conditions the dummy helicopter is suspended from elastic cord bundles that are as soft as possible for the deflection height available in the test area. This tries to simulate the helicopter being in hover without transferring dynamics from the structure suspending the dummy helicopter. A heavy frame is assembled over the dummy helicopter from which a hydraulic actuator acts upon the dummy rotor head, this simulates vibrations coming from the rotor blades.

Both displacement and force is measured at the dummy transmission and hydraulic actuator interface, the hydraulic actuator is controlled through the displacement transducer and the force going into the dummy helicopter is measured and used to calculate the frequency response functions. Accelerometers capture the acceleration of the dummy transmission and fuselage, and in conjunction with the force data, are used to generate the frequency response functions.

6.1 Experimental setup

The experimental setup is designed in SolidWorks and the final assembly is as shown in Figure 69, with a broken out section view through one of the frame legs to ensure that all the detail is visible. The circle and triangles show the locations of the accelerometers on the transmission and fuselage respectively. Only the vertical heave response is of interest in this experiment so all accelerometers are facing upwards and only capture vertical acceleration.

Note that there are two fuselage accelerometers on either side of the transmission, due to asymmetry of the transmission leaning forward at roughly 10°.

There is pitch moment introduced that cause angular acceleration of the dummy fuselage.This angular acceleration is significant enough to be recorded by the vertical accelerometers and influences the location of the perceived antiresonance frequency.

Two accelerometers are placed at equal lengths from the centre of rotation of the dummy fuselage, averaging their signals effectively filters out the effect of the angular acceleration signal and isolates the vertical acceleration as this is the only acceleration of interest in this experiment.

The accelerometers are attached to the fuselage using wax, small discs are glued at the locations of interest to assure a level and smooth surface. Figure 70 shows the fuselage and transmission accelerometers.

Figure 71 shows the effect of the rotational acceleration on the frequency response functions of the heave response. Both accelerometers measure the resonance peak at the same frequency, with the front accelerometer measuring larger magnitudes than the rear until about $34.7Hz$ where the reverse relationship is visible. The measured antiresonance frequency locations are different for the two accelerometers, with the front being at a slightly higher frequency than the rear accelerometer.

The ADAMS model defines the heave response as the vertical acceleration of the fuselage centre of mass to a vertical force excitation, and the experimental results are compared to this response. There was no way to directly measure the centre of gravity acceleration as the centre of gravity lies within the concrete, by taking the average of the two accelerometers over the centre of mass gives us an approximation of the vertical response of the centre of gravity, seen as the solid line in Figure 71. Throughout this dissertation this average response will be compared to that of the ADAMS results unless specified otherwise.

The interface between the dummy rotor head and the frame is shown in Figure 72, this shows the layout of the hydraulic actuator and various measuring equipment. A hydraulic actuator applies force to the dummy rotor head, this force is measured with the force transducer connected between the actuator and the rotor head. The displacement transducer, connected between the force transducer and the actuator cylinder and therefore in effect the heavy frame, serves as the feedback signal for controlling the amplitude and frequency of the input excitation.

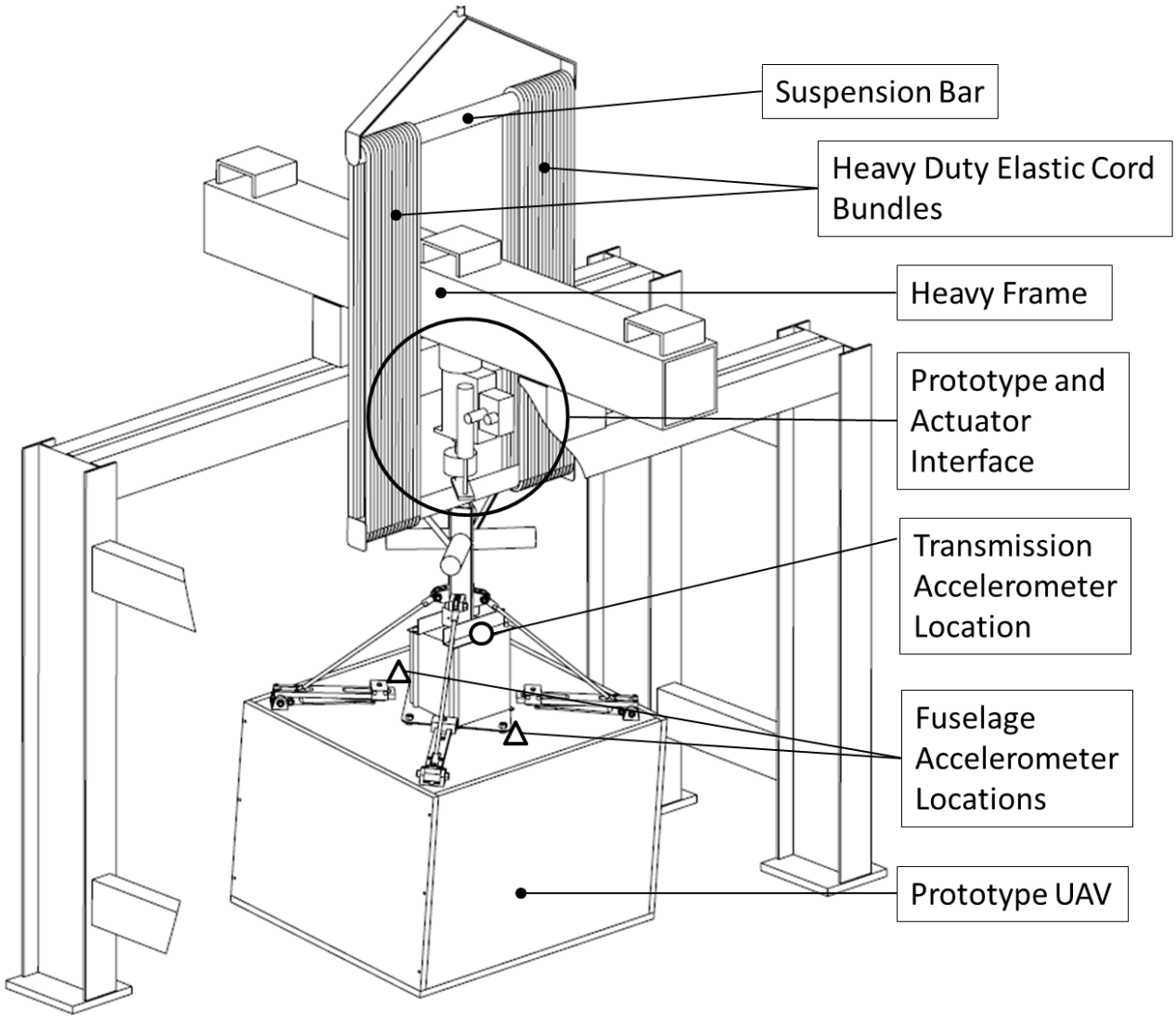

Figure 69: Experimental setup diagram

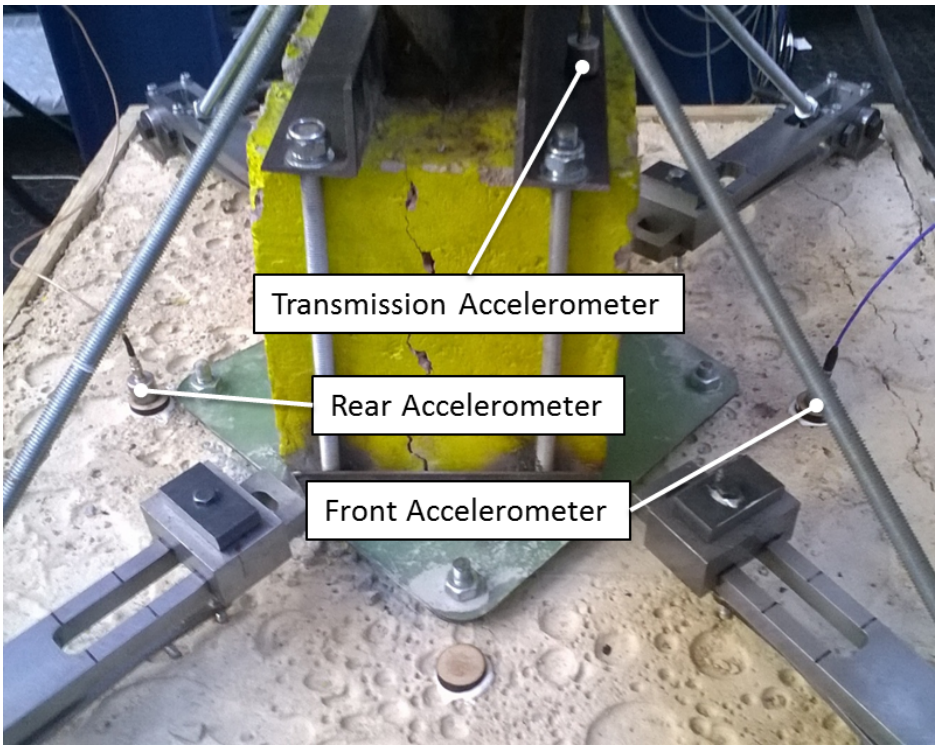

Figure 70: Accelerometer Locations

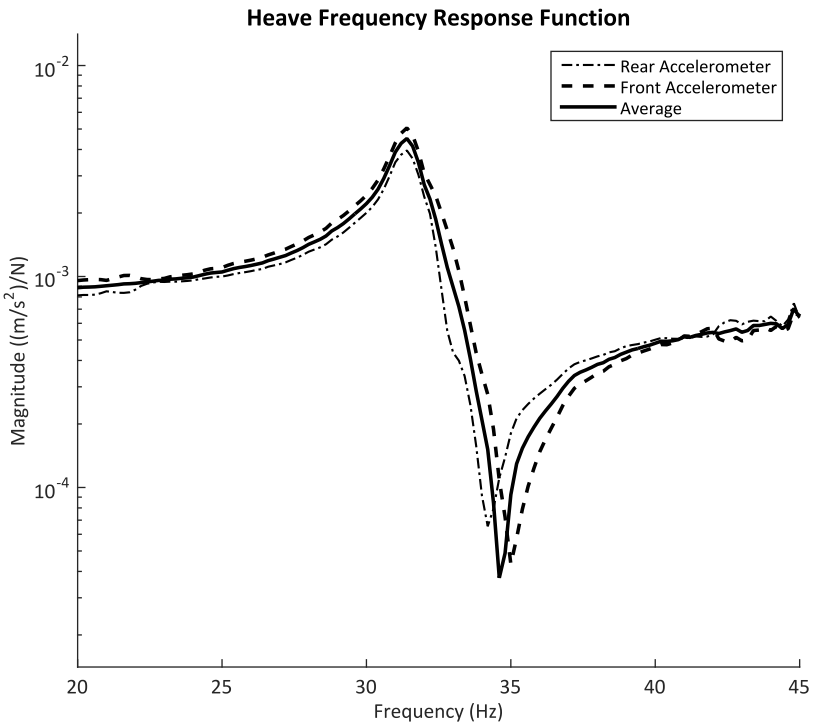

Figure 71: Effect of rotational acceleration on heave response

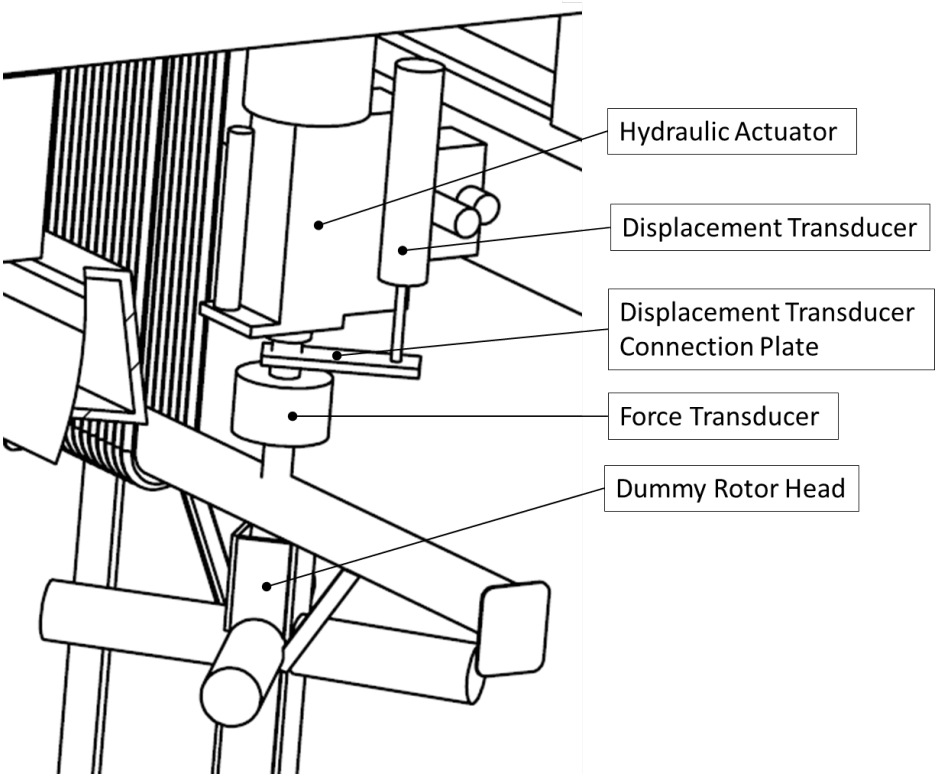

Figure 72: Instrumentation setup diagram

Originally it was attempted to control the input excitation solely by the force transducer, which would negate the need for measuring displacement, however, this control scheme was unstable resulting in a test where the experiment was forced into the ground, cracking the transmission block. The transmission had to be fixed by adding a cage that clamped the concrete together. Controlling the experiment through a displacement transducer ensures that the dummy helicopter is constrained to move around a set point, reducing the risk of control failure and further damage to the experiment.

Seen in figure 73 is the actual layout of the afore mentioned setup.

The full experimental setup is shown in Figure 74.

6.2 ADAMS model

A full ADAMS model is created of the prototype and analysed for vibration, these results are compared to the experimental results. The complete SolidWorks assembly created during the design of the prototype is imported into ADAMS as a .STEP file and the parts are all constrained relative to each other with joints that are analogous to their real world counterparts. Figure 75 shows the prototype in the ADAMS model view.

6.2.1 Pendulum mass placement and flexible leaf spring bodies

Figure 76 shows the locations of the pendulum mass on the pendulum arm for the different frequencies of interest, as well as the effective pendulum arm length ratios Q_R for each. The leaf springs are flexible FEM bodies that are directly utilised by ADAMS for vibration analysis, this is a more realistic analysis than using distinct massless

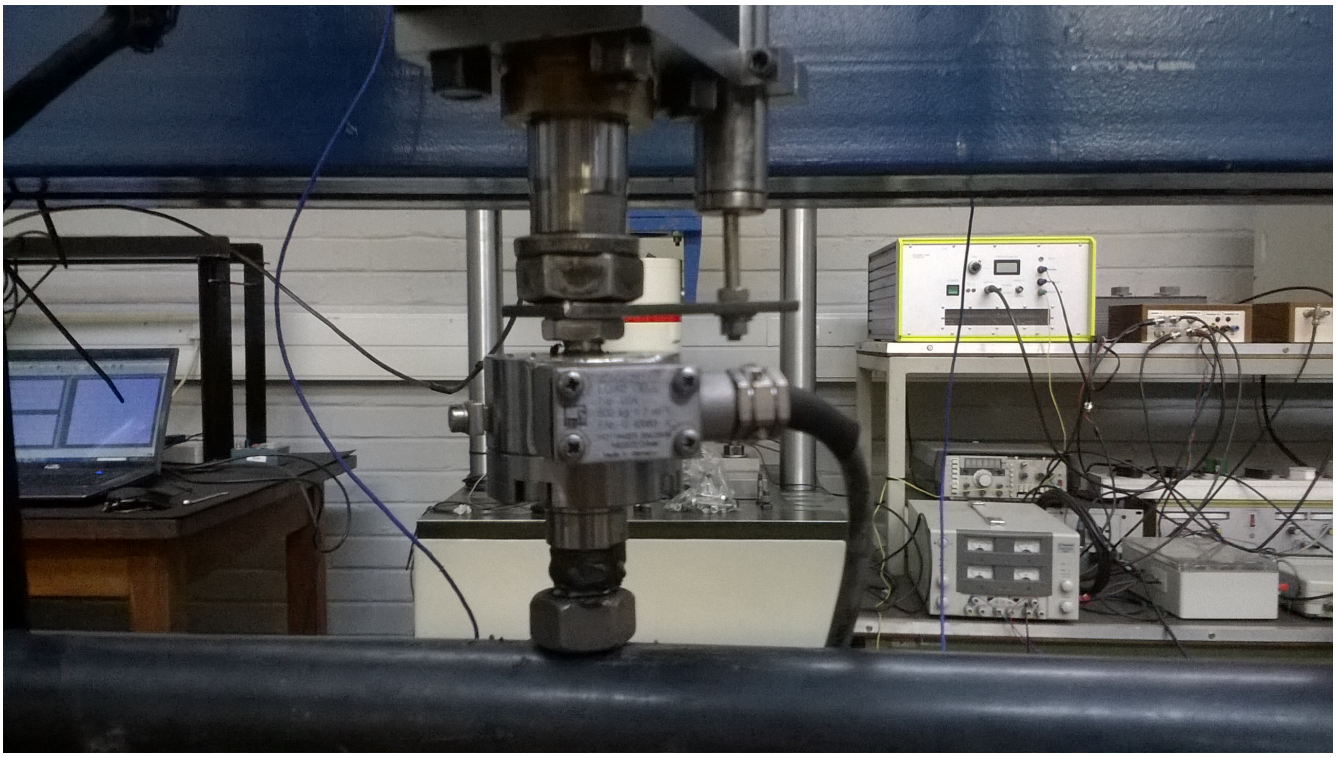

Figure 73: Instrument Setup

springs and will yield more accurate results because the mass of the spring does influence the Pendulum Arm Length Ratio. The pendulum masses are $483g$ and the leaf springs have stiffnesses of $2.62 \times 10^6 N/m$ as discussed in Section 5.1.1.

6.2.2 Flexible leaf springs and pendulum arms

As will be discussed in the following sections, the ADAMS model is further refined by replacing the rigid pendulum arm bodies with flexible ones as seen in Figure 77.

There is also a distinct massless spring added to the ADAMS model at a later stage to represent the diaphragm plate stiffness, see Figure 78.

Just to show the flexible bodies in action Figure 79 on page 76 shows the natural resonance mode shape of the Vibration Isolation System at $31.1 Hz$ with the leaf springs showing a bending shape.

Figure 80 on page 76 shows the natural mode shape at $196 Hz$ with both the Leaf Springs and the Pendulum Arms showing flexible bending shapes.

6.3 Experimental results and comparison

All the responses shown up to Subsection 6.3.10 are the frequency response functions of the fuselage heave acceleration, normalised to a theoretical system response that has no vibration isolation system. If this theoretical system is infinitely stiff the response function is simply a constant value of the reciprocal of the system mass over all frequencies. Thus the heave response shown is representative of the amplification or attenuation of the system

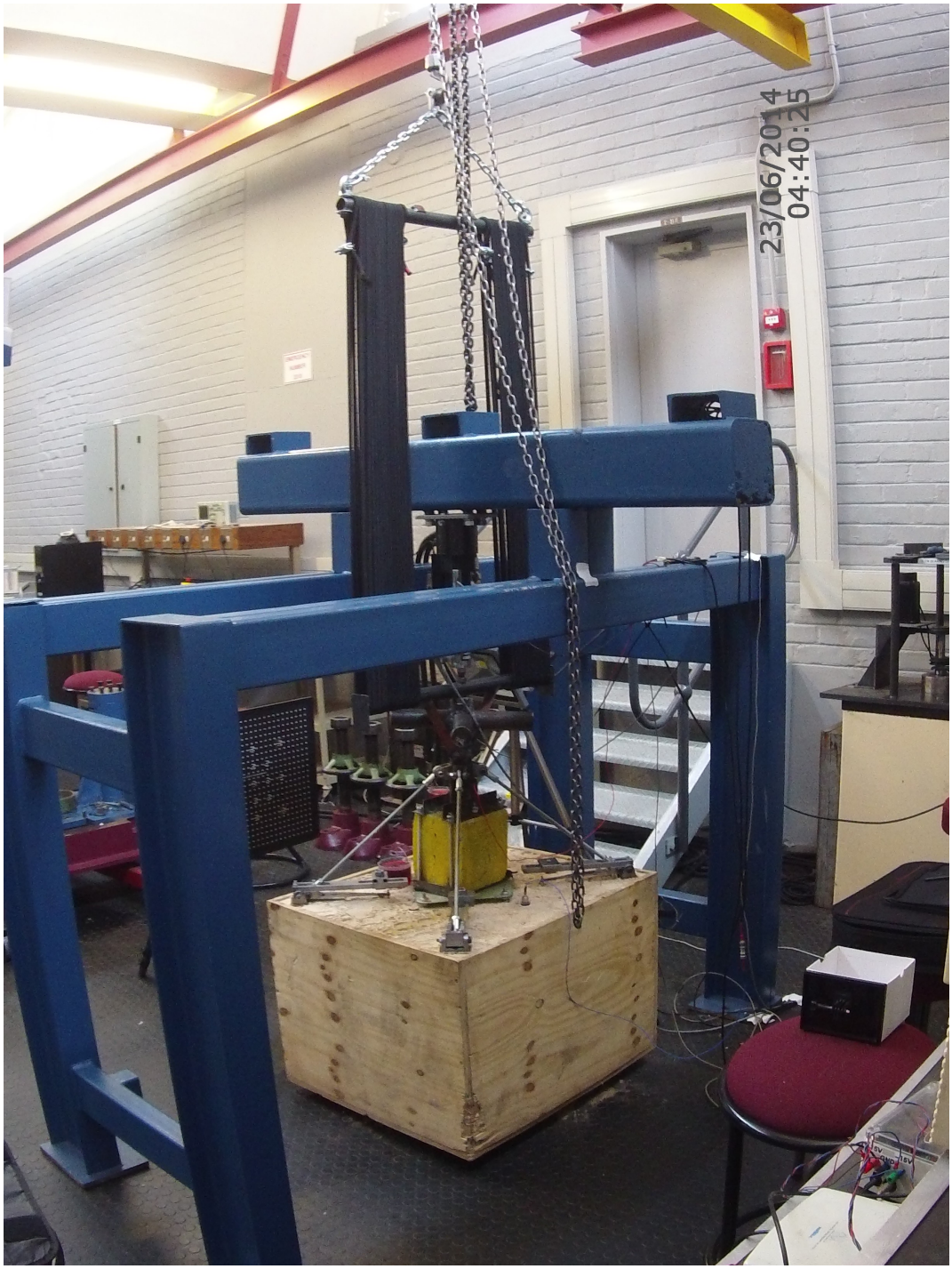

Figure 74: Experimental setup

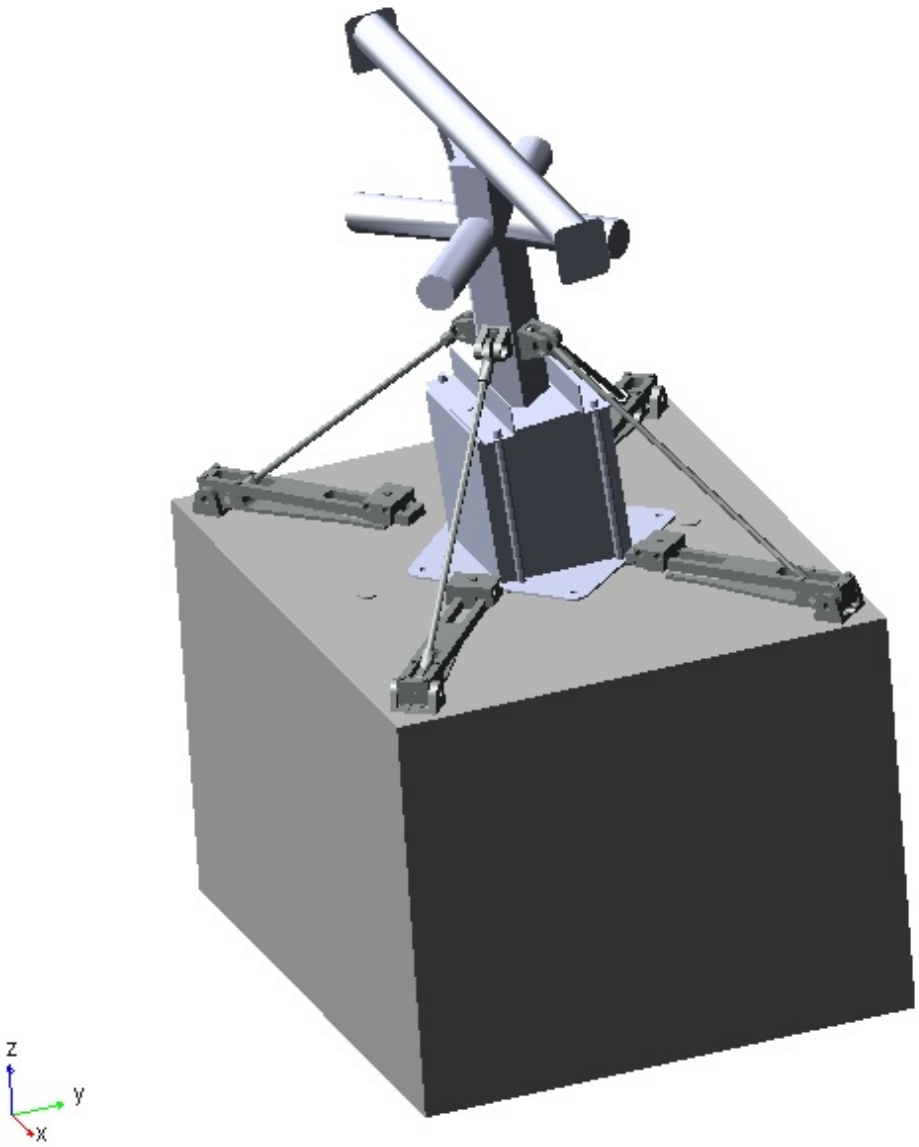

Figure 75: ADAMS Model

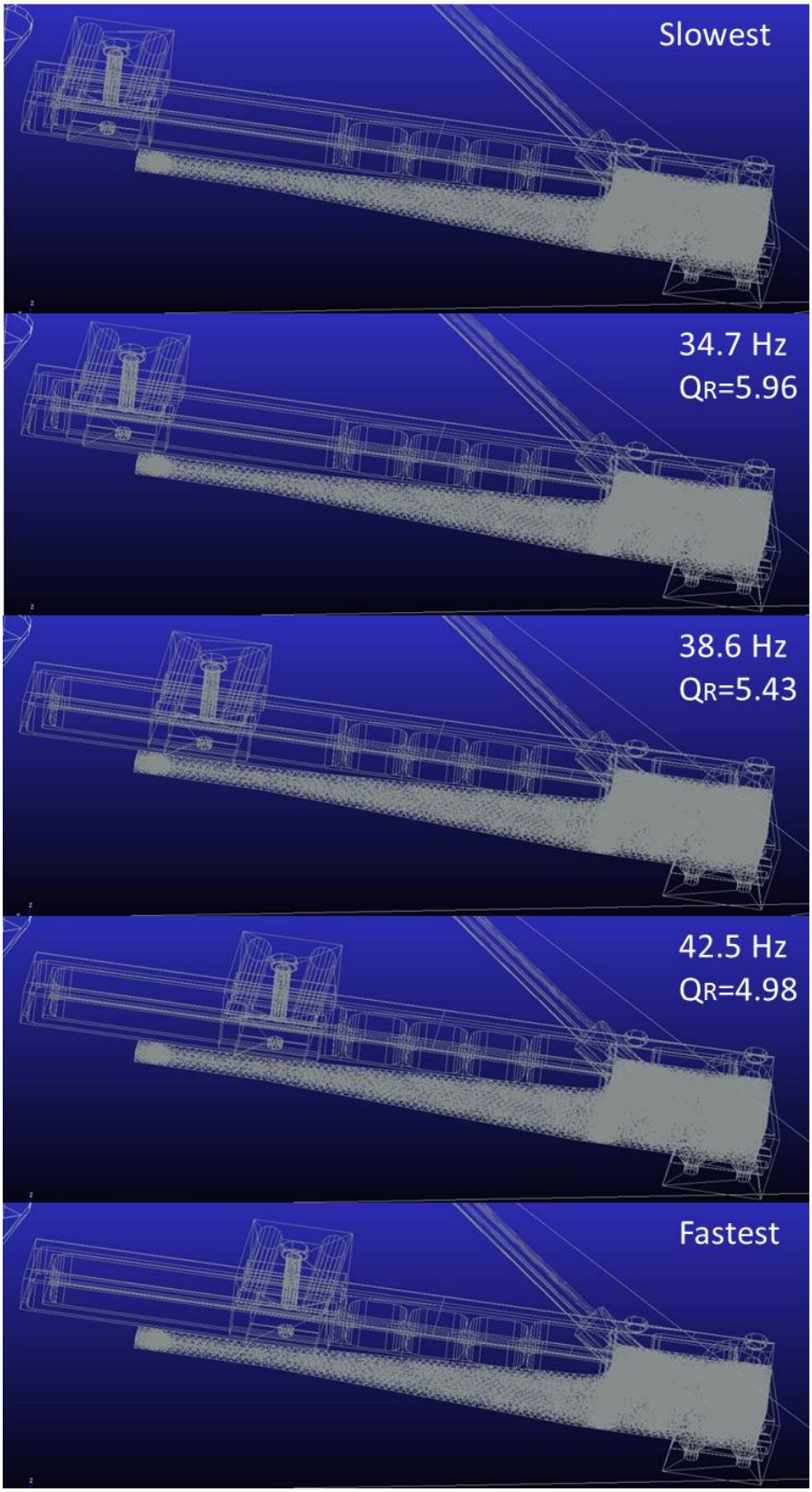

Figure 76: Pendulum mass positions and effective pendulum arm length ratio Q_R

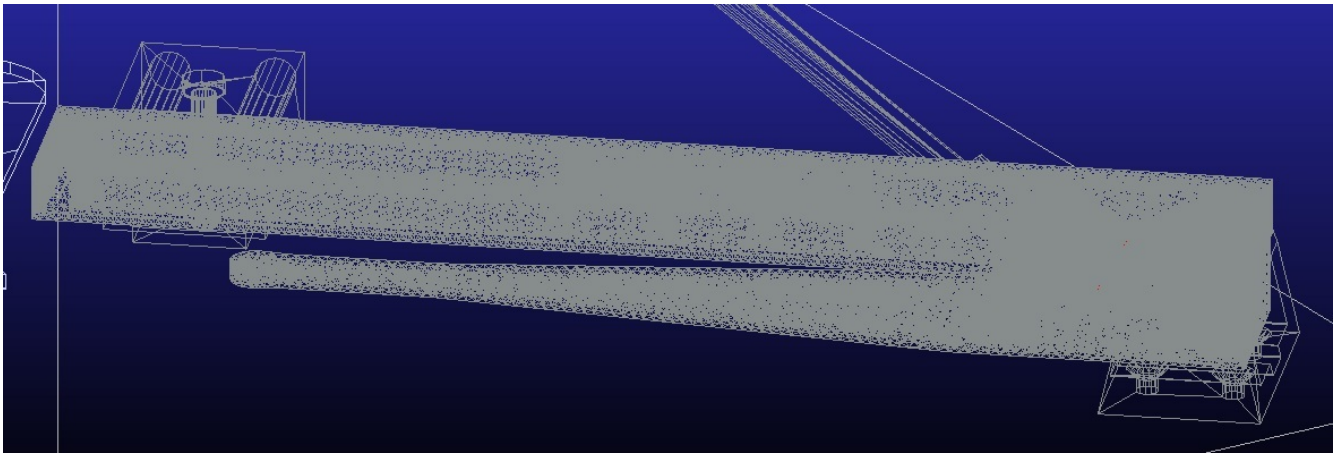

Figure 77: Flexible leaf spring and pendulum arm

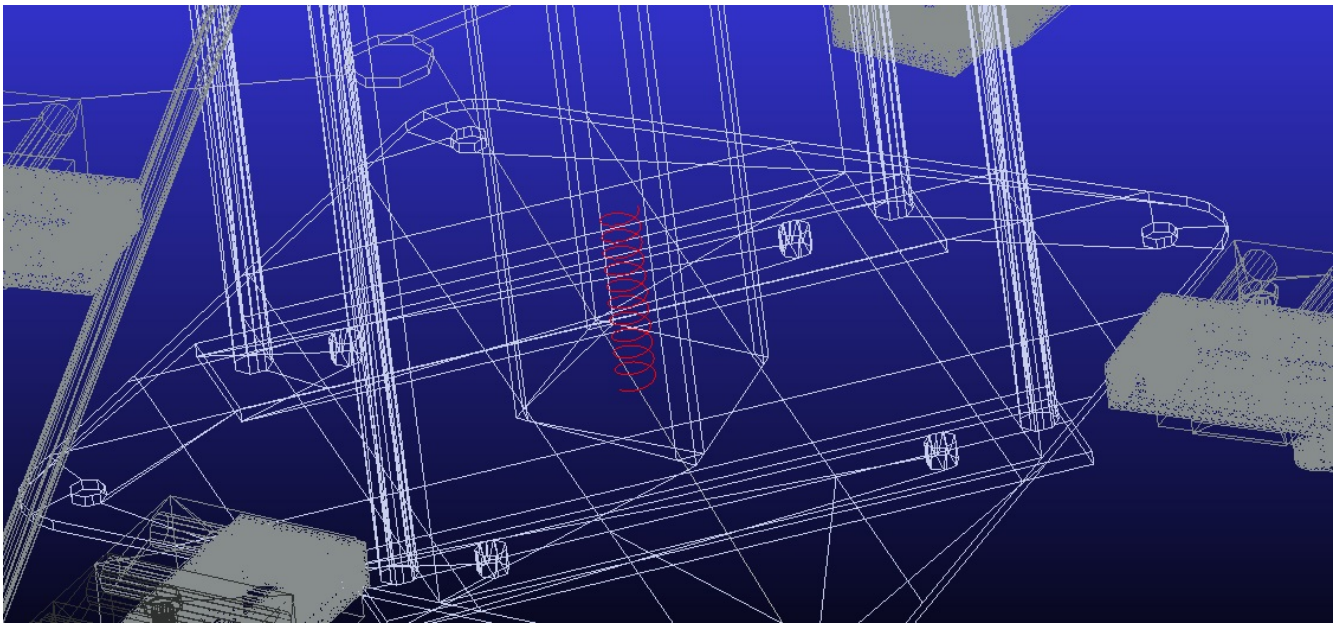

Figure 78: Diaphragm plate stiffness approximation

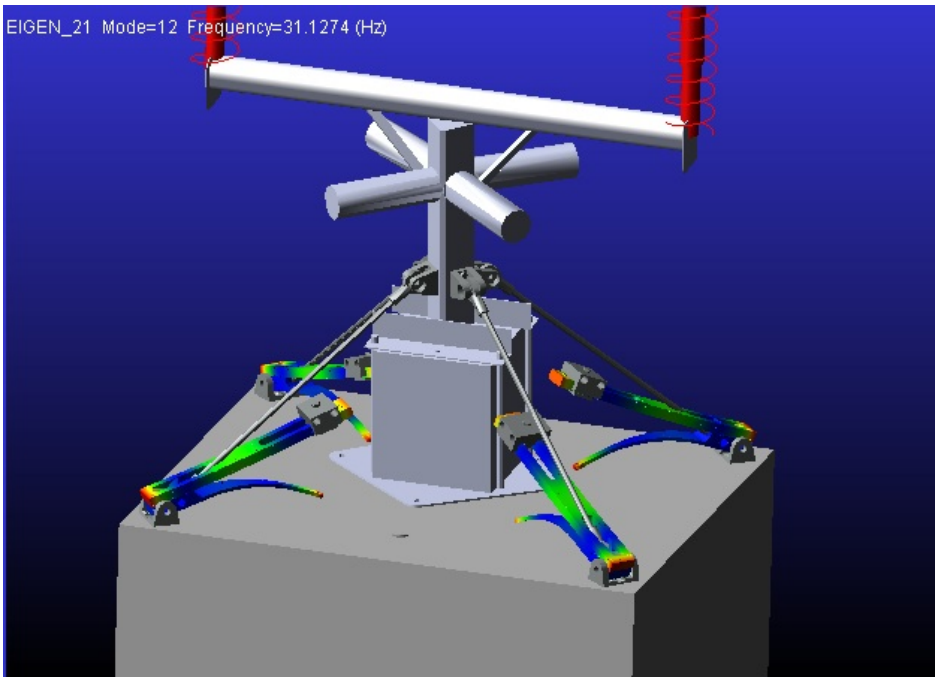

Figure 79: Natural mode shape at 31.1 Hz

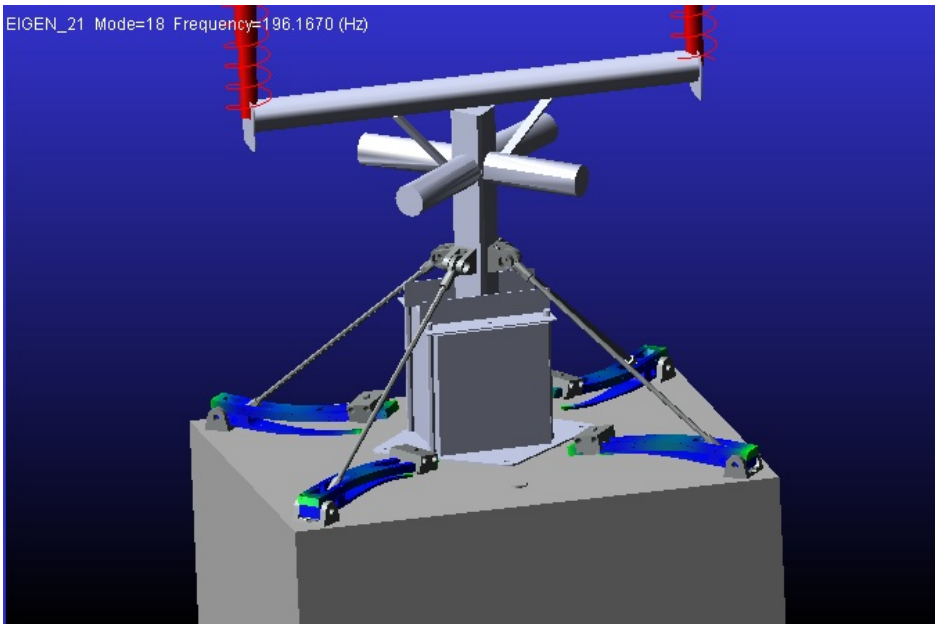

Figure 80: Natural mode shape at 196 Hz

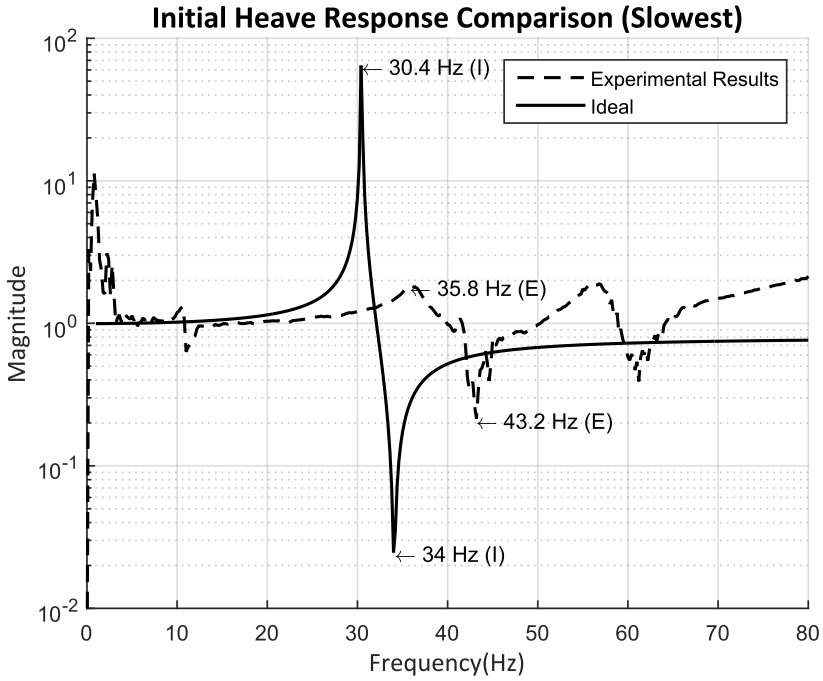

Figure 81: Initial heave response for the slowest state

response at a certain frequency in comparison to a system having no vibration isolation system. Therefore the y axis is unitless and is an amplification or attenuation factor or ratio, this is a much more intuitive communicator of system performance compared to accelerance $((m/s^2)/N)$.

However, this is not the true measure of system performance as it is a comparison between a fuselage with an antiresonance vibration isolator and one without, and does not show the level of vibration transmission from the source (transmission and rotor hub assembly) to the fuselage. Therefore, the final comparison and measure of system performance is done in Subsection 6.3.10 in the form of a transmissibility graph comparing the fuselage heave response in reference to transmission and rotor head assembly response, which shows the transmission of the vibration through the system.

Initial experimental results do not reflect what is theoretically expected, tests show that friction damping creates a phenomenon where it increases the dynamic stiffness and therefore increases the antiresonance frequencies. How the friction damping problem is detected and remedied is discussed in the sections to follow.

First the absolute end states of the vibration isolation system is experimentally tested to get an idea of whether or not the system is performing as designed. The first absolute state, called the slowest state, is where the pendulum mass is shifted all the way out, and this corresponds to the slowest possible antiresonance frequency obtainable by the system. Alternatively the fastest state is where the pendulum mass is shifted all the way in, and corresponds to the fastest antiresonance obtainable by the system. The three specific antiresonance frequencies that this system is designed for, lie between these two end states.

6.3.1 Initial results

The initial heave responses for both the slowest and the fastest states are shown below compared to the ideal theoretical response.

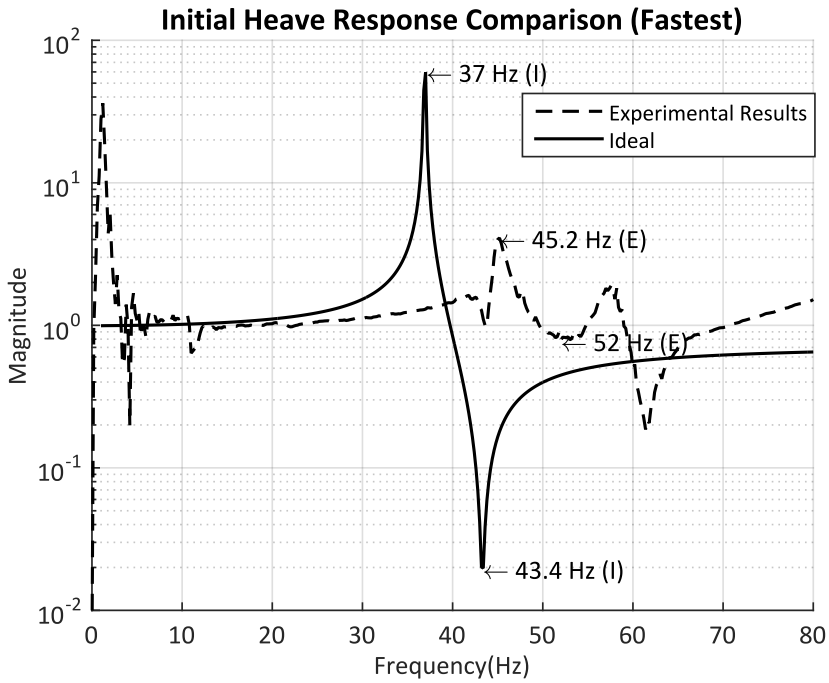

Figure 82: Initial heave response for the fastest state

Figures 81 and 82 shows the initial experimental results compared to the ideal ADAMS simulation for the slowest and fastest states respectively, both states show that the resonance and antiresonance peaks and valleys are not well defined and in both cases there is a very dominant unexpected response between 50 and 70 Hz. Secondly both cases show resonance and antiresonance peaks at about $10Hz$ higher than the system is designed for.

6.3.2 Centre excitation modification

It was suspected that the system might be excited in either the pitch or roll directions due to the transmission being suspended from the centre of the dummy rotor head and excited off centre, so the transmission was modified to be suspended from a bar and then excited on the centre of the dummy rotor head to minimise rotational excitation. After modifying the transmission the results are showed in Figures 83 and 84.

Exciting the experiment from the centre greatly improved the results in both the slowest and fastest cases, with sharper more well defined resonance peaks and antiresonance valleys than what was achieved with the previous configuration. The unexplained dynamics between 50 and $70Hz$ have also disappeared, confirming the suspicion that the system was excited in rotation, that adversely affected the heave response results. However, the figures clearly show that both responses are still roughly $10Hz$ higher than expected and the cause yet to be discovered.

The individual masses and the pendulum arms are weighed to check for discrepancies and the pendulum arm ratios measured before each test to ensure that they are correct. Due to the very large stiffness of the overall system, it was too difficult to measure the static stiffness as very large forces are required whilst measuring very small deflections that are susceptible to measuring errors. Tests concluded that the mass differences between the ideal and actual system was no more than 2.5% for the pendulum arms and less than 1% for the pendulum masses.

The pendulum arm ratios are for all practical purposes identical. These mass discrepancies are not large enough to cause a antiresonance frequency increase of $10Hz$, using the equations in the feasibility study either the mass

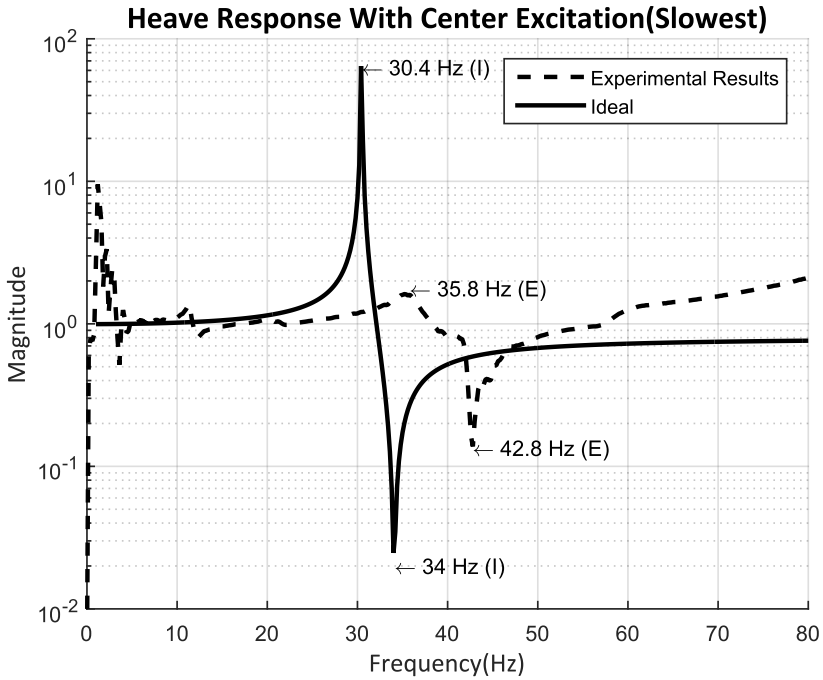

Figure 83: Initial heave response for the slowest state with centre excitation

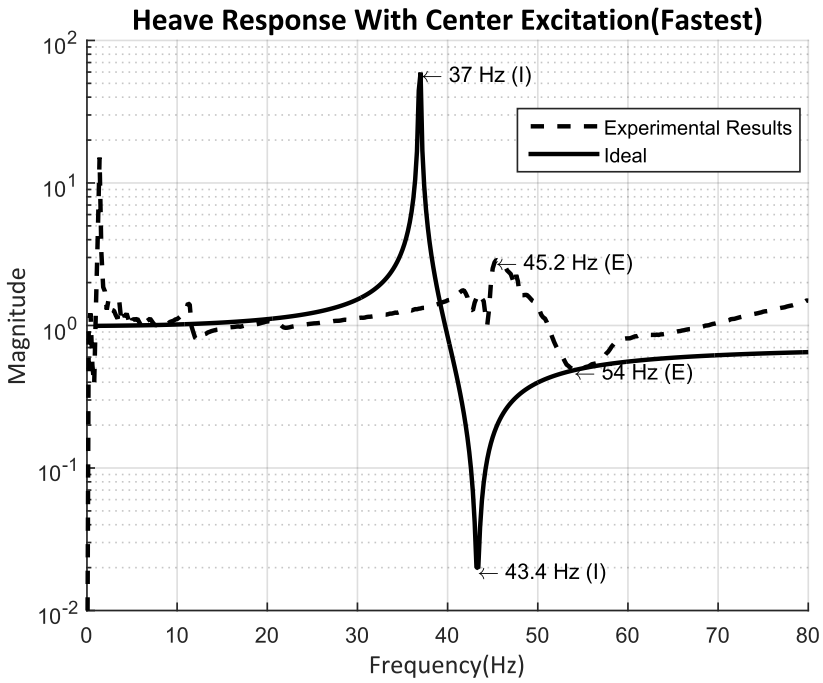

Figure 84: Initial heave response for the fastest state with centre excitation

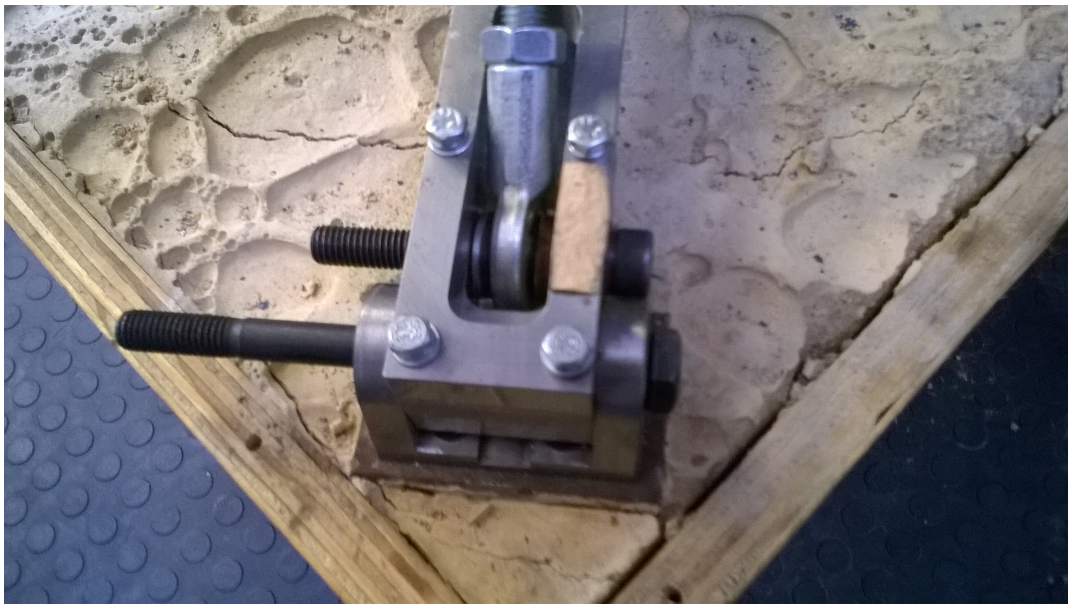

Figure 85: Loose bolt pins

should be 40% lower or stiffness should be 67% higher than currently measured, to account for the $10Hz$ higher antiresonance frequencies. Even though the system stiffness is not experimentally verified, it is highly unlikely that the leaf springs are all 67% stiffer than what they were designed to be. Some other phenomenon must be the cause of these large discrepancies.

6.3.3 Friction damping phenomenon

After many tests it is decided to investigate the effect of the friction damping in the joints as being the possible cause of this phenomenon, as friction damping is highly non-linear and unpredictable. The precision fit bolts that are originally inserted in all the joints are removed and replaced with $10mm$ bolts which have a shaft diameter of $9.7mm$, and because of the $10mm$ hole sizes this is a very loose fit and instead of having half the hole as a friction surface we are now left with a smaller contact area almost like a pin joint with a great reduction in friction contact surface area. Figure 85 shows these bolts fitted on the experimental setup.

The results of the looser bolts are immediate and substantial.

Figures 86 and 87 show that the results have improved drastically, the slowest frequency is now only $2.4Hz$ higher than the ideal and the fastest only $5.4Hz$ higher compared to both being on average $10Hz$ higher with the original tolerance bolts. This confirms that the higher antiresonance frequencies are caused by a friction damping phenomenon.

6.3.4 Study of reduction of bearing friction

To eliminate most of the friction in the joints, low profile needle roller bearings are inserted in the fuselage hinges and the leaf springs. These bearings only have an outer race with the needle rollers running directly onto the precision $10mm$ hardened bolts, this creates a very low profile bearing with an outer diameter of $14mm$ and an inside diameter of $10mm$. This was a necessity as the leaf springs are only $20mm$ thick meaning that normal bearings with inside diameter of $10mm$ will not fit into the available material.

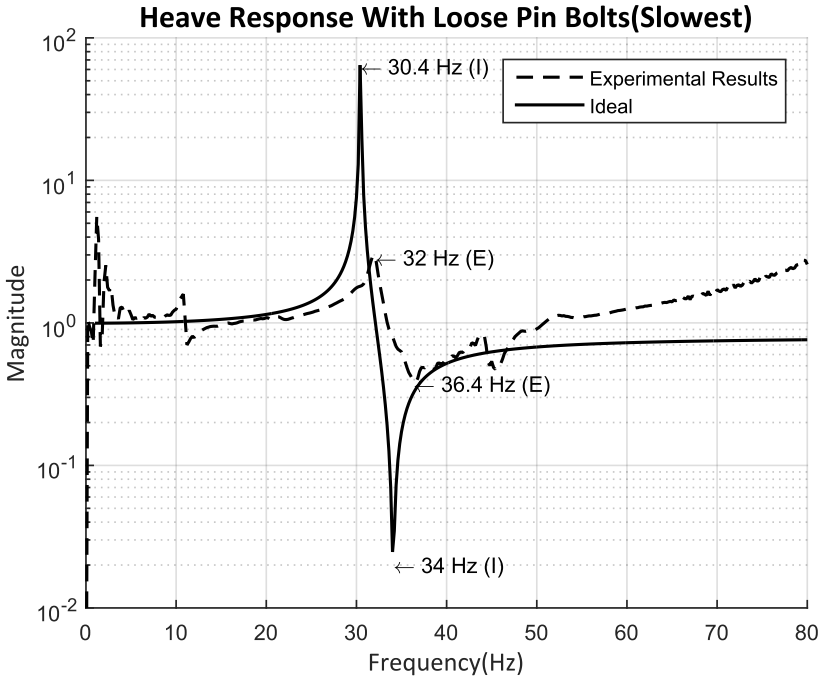

Figure 86: Slowest heave response with smaller bolts

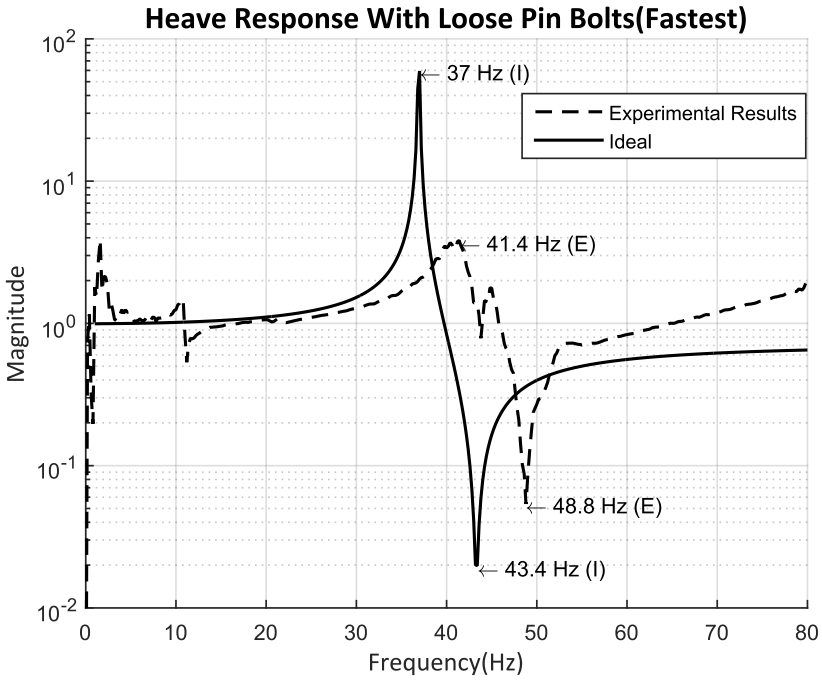

Figure 87: Fastest heave response with smaller bolts

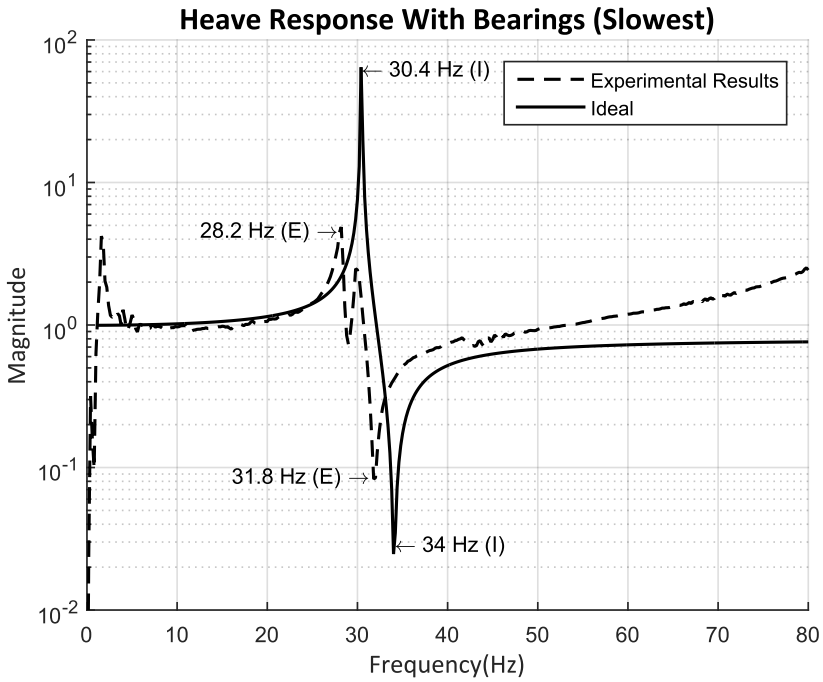

Figure 88: Slowest heave response with bearings

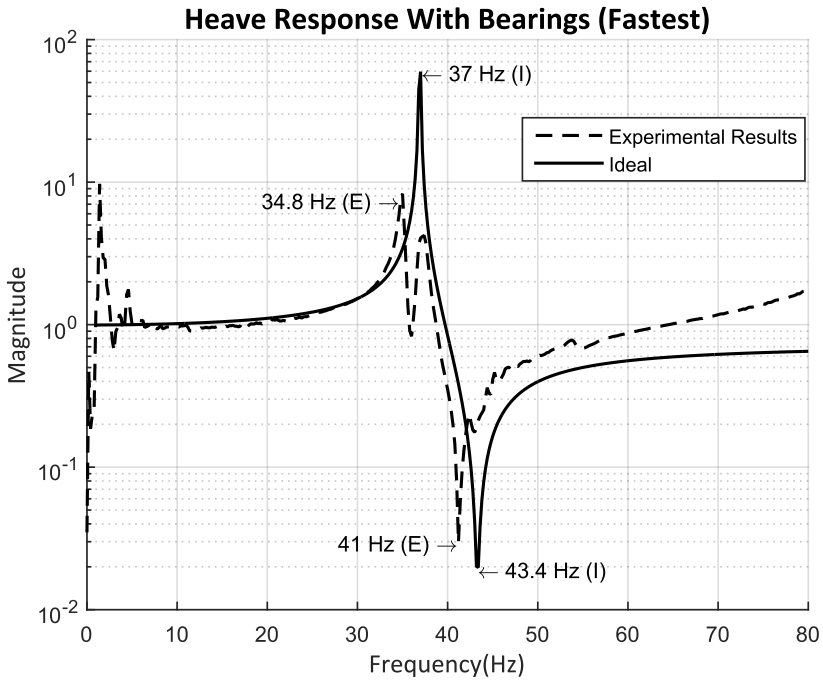

Figure 89: Fastest heave response with bearings

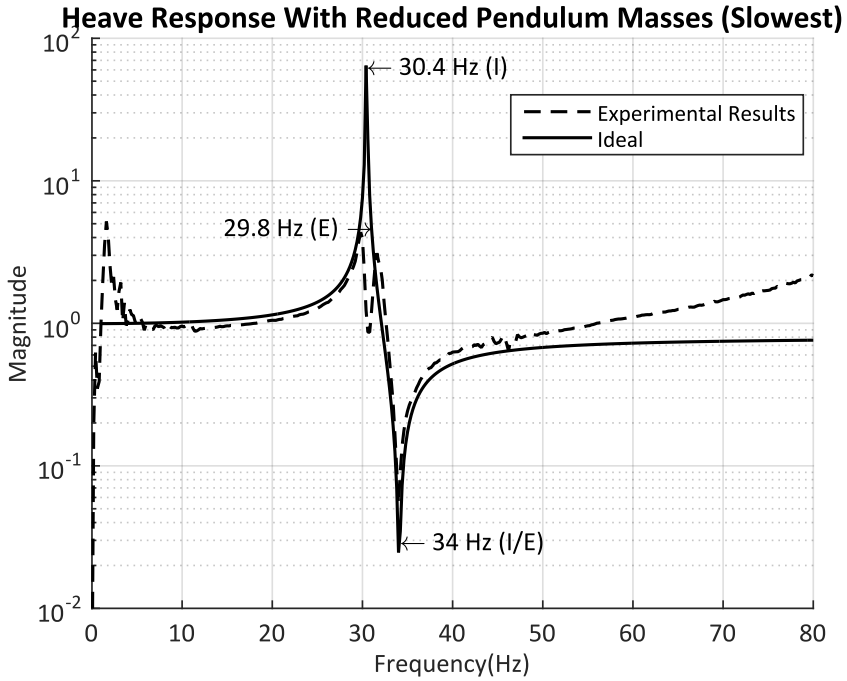

Figure 90: Slowest heave response with reduced pendulum masses

Figures 88 and 89 show the slowest and fastest heave responses with the bearings inserted, both antiresonance frequencies are much closer to the ideal within about $2.4\,Hz$, relating to a 6.5% and 5.5% error on the antiresonance frequencies of the slowest and fastest responses respectively.

The experimental results have now dropped below the ideal expected results and is a clear indication that the stiffness of the experimental vibration isolation system is lower than what it was designed for considering that the masses and pendulum arm ratios are verified to be very accurate. Furthermore there is a double resonance peak before each antiresonance, which is an unexpected result that requires explanation.

6.3.5 Retuning the vibration isolation system by reducing pendulum-mass weight

Because it is difficult to determine the exact cause of the overall lower stiffness and more so to increase said stiffness, it is decided to alter the pendulum masses instead, to further fine tune the vibration isolation system. The equation used to initially design the vibration isolation system, equation 1, is used to determine the effective current overall stiffness given the measured masses, pendulum arm ratios, and the recorded antiresonance frequencies as seen in Figures 88 and 89.

From this the stiffness is calculated to be $9.26 \times 10^6 N/m$ which is about 9.5% lower than the designed stiffness of $10.2 \times 10^6 N/m$. A new required pendulum mass value is calculated from this effective stiffness and it is determined that the pendulum masses must be reduced by 70 grams to retune the system to the ideal antiresonance value. Two $12mm$ diameter holes drilled through the $40mm$ width of the pendulum masses reduces the weight by the required 70 grams, the experimental results follow.

Figures 90 and 91 are the heave responses of the system after the pendulum mass reduction, the figures show that the antiresonance frequencies now align almost perfectly. However, there are still the double resonance peaks on both results that require further investigation.

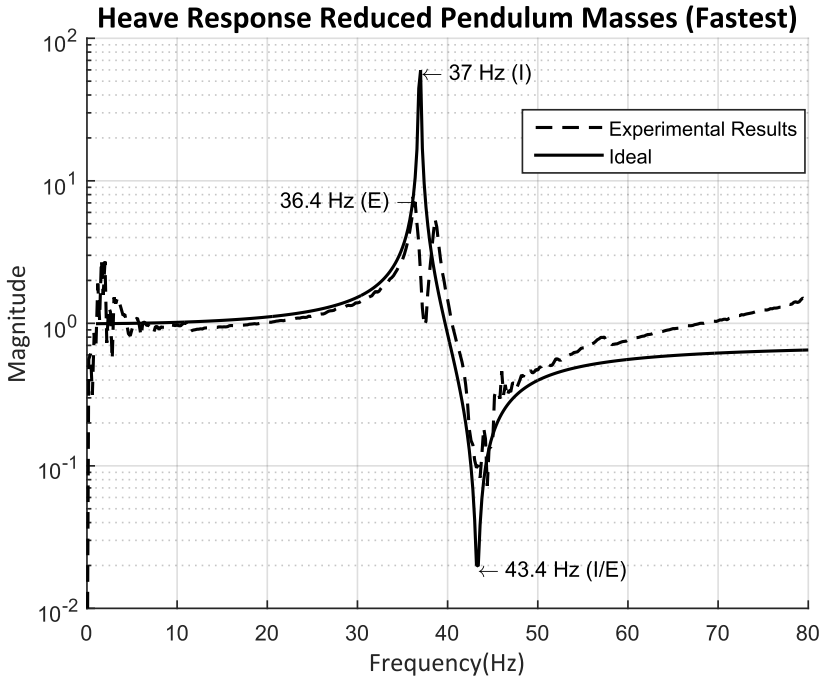

Figure 91: Fastest heave response with reduced pendulum masses

Even though the antiresonances align exactly and the system will function exactly as expected at this frequency, the second resonance peak lies closer to the ant-resonance and makes this system more susceptible to running into that resonance frequency if the rotor speed would vary or slow down. Before the double resonance peak is investigated, we place the masses at the designed lengths corresponding to the three frequencies that the system is designed to alleviate, to see if the vibration isolation system is working as expected.

Figure 92 shows the fuselage response to heave at the three distinct frequencies that the system is designed for, clearly the system is very well tuned as the experimental antiresonance frequencies align very well with the ideal theoretical results. The fastest frequency at $42.5\,Hz$ does not have a well defined antiresonance peak, this is due to the fact that the hydraulic shaker struggles to input energy into the system at higher frequencies as is the nature of hydraulics. Except for the double resonance peaks and the noisy results at higher frequencies this system is a fully functioning antiresonance vibration isolation system.

6.3.6 Study of double resonance peaks

However, to gain a better understanding of this system the double resonance phenomenon is investigated. So the question is, what can cause the system to have an overall lower stiffness and create double resonance peaks? The leaf spring thicknesses are measured to investigate the stiffness issue as it was expected that perhaps the leaf springs were fabricated thinner than was specified.

It is discovered that two of the leaf springs are $0.1mm$ thicker than the designed $4.9mm$, one spring is exactly $4.9mm$ thick and the last remaining spring was grossly out of specification at $4.7mm$ thickness. This explains the lower stiffness and possibly the double resonance peaks. With the tuning masses set to the demarcated positions for $34.7Hz$ antiresonance frequency, the pendulum mass of the defective vibration isolation assembly is shifted out of the demarcated position until the double resonance peaks converge into one.

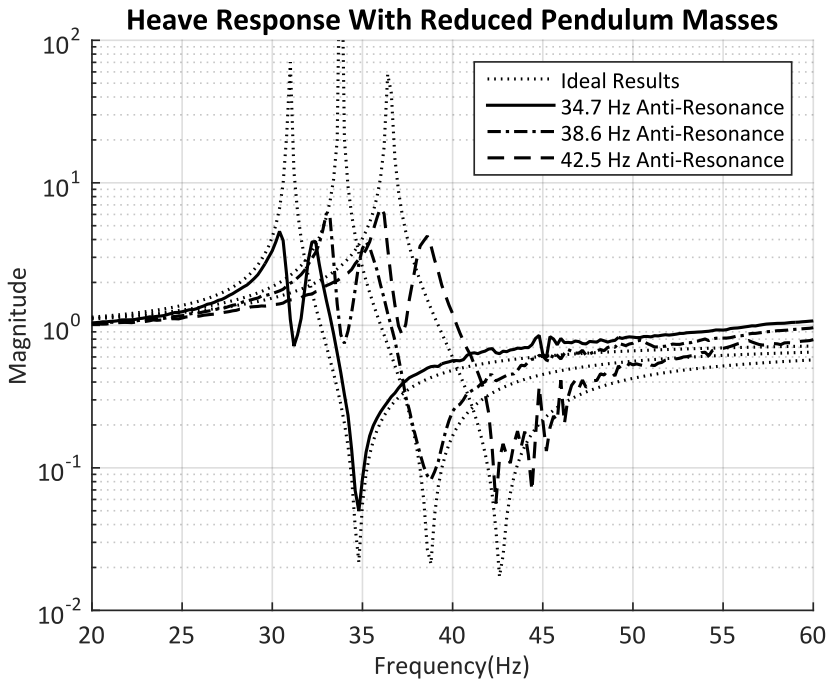

Figure 92: Heave response for three design frequencies with reduced pendulum masses

The effective stiffness of only the defective spring is then calculated by using the out of place distance, the known pendulum mass and the pendulum arm ratio. Thus the effective stiffness of the defective spring was calculated to be round about $1.918 \times 10^6 N/m$ which is almost 25% less stiff than what the spring is designed to be. A required mass is in turn calculated specifically just for the defective VIS pendulum arm that will achieve the three distinct antiresonance frequencies at the designed pendulum mass lengths, given the newly calculated spring stiffness.

This new mass that will only be used on the defective VIS assembly is a $100 grams$ lighter than the previous mass and was simply cut from a flat bar, as removing that amount of mass from the already drilled and modified pendulum mass is too difficult. Assuming that the other three springs have stiffnesses that are roughly the same , we calculate effective spring stiffnesses for these springs by subtracting the defective spring's stiffness from the overall stiffness calculated previously and dividing that by three as all 4 springs make up the overall stiffness.

New pendulum masses are calculated for the non-defective spring's assemblies given the newly estimated effective stiffness plus the designed pendulum arm ratios. These new masses are required to be $28 grams$ heavier, so M16 nuts were simply glued to the current pendulum masses to increase the mass by the required amount.

Figure 93 shows the heave responses with the corrected masses, the double resonances have now disappeared with the antiresonances very accurately correlating with the theoretical ideal with a 0.3% , 0.5% and 0.7% error on the $34.7 Hz$, $38.6 Hz$ and $42.5 Hz$ frequencies respectively.

6.3.7 Adjusted ADAMS model for improved correspondence with experimental model

Due to the discrepancies in the spring dimensions and the modifications done to the pendulum masses, the ADAMS model that was created during the design phase and used to create the ideal theoretical results does not represent the experiment anymore.

Although the ideal theoretical ADAMS results were used as a reference to modify and tune the experiment to alleviate vibration at the designed frequencies, they are fundamentally two different systems with now similar

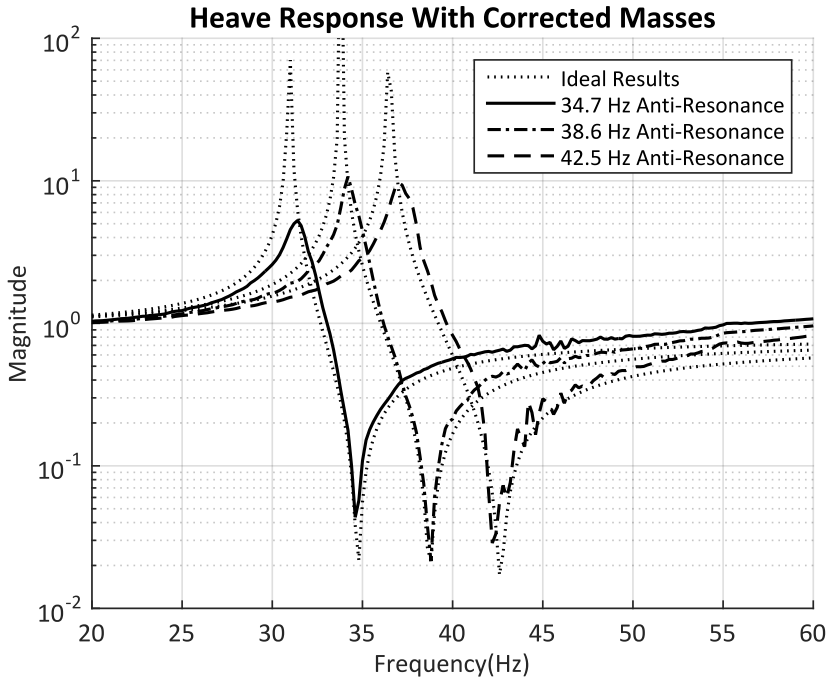

Figure 93: Heave response for three design frequencies with corrected pendulum masses

responses. All the parts of the prototype helicopter are accurately weighed and measured, and from these results a new ADAMS model is created. Table 3 shows the measured weights of all the prototype parts.

From Table 3 we see that the actual dummy fuselage and transmission and rotor hub assembly masses are within 0.5 and 0.2% error of their designed mass. For vibration isolation assemblies 1 to 3 their masses are below 0.5% error of their design weight, and for the defective VIS the mass is within 7% of the corrected desired mass.

The largest deviating pendulum arm is within 2.6% error of the design weight and finally the largest deviating leaf spring is within 3.4% error of the design weight. All the actual masses are within acceptable experimental error allowance.

As mentioned in the beginning of Section 6.3.6, two springs were 5.0mm thick, one 4.9mm and one 4.7mm. Flexible bodies are created for each different thickness spring and used within the ADAMS model. The pendulum arm and pendulum mass solid bodies are the same as used for the initial ADAMS model, but instead of allowing ADAMS to calculate their masses based on geometry we override their mass values with the ones that are measured from the actual experiment and tabulated in Table 3. Lastly both the fuselage and dummy transmission mass values obtained in Table 3 are applied to their ADAMS solid bodies, all the inertia values are estimated from the SolidWorks models and inserted into the ADAMS model, Tables 4 and 5 show the estimated inertia matrices for the fuselage and transmission.

The ADAMS model is now representative of the actual experiment and their results can be compared and discussed.

Figure 94 shows the new ADAMS model results compared to the tuned experimental results, keep in mind that the experimental results are the correct results as the system has been tuned. The frequency displayed at the front of each legend entry is the intended antiresonance frequency location and the frequency in brackets is the actual result.

From the figure it clear that the ADAMS results for all three responses show antiresonance frequencies that are about 1Hz higher than the experimental, this corresponds to an error of about 3% for the 34.7Hz and 38.6Hz

Mass Specifications				
	VIS 1 (g)	VIS 1 (g)	VIS 1 (g)	VIS 1 (g)
Pendulum Mass:	438.5	438.2	438.9	329.7
Pendulum Arm	426.7	432.1	432.3	432.2
Leaf Spring:	395.4	381.2	397.2	387.3
Total:	1261	1252	1268.4	1149.3

VIS Total Mass:	4.93 kg

Total Mass:	617 kg
Load Cell Zero:	-3 kg
Bungee Mass:	7.1 kg
Transmission Mass:	32 kg
Fuselage Mass:	576 kg

Table 3: Measured experimental part masses

$kg\,m^2$	x	y	x
x	3.05×10^{-9}	-7.2×10^{-14}	2.6×10^{-13}
y	-7.2×10^{-14}	3.12×10^{-9}	-1.1×10^{-9}
z	2.6×10^{-13}	-1.1×10^{-9}	3.01×10^{-10}

Table 4: Estimated fuselage inertia matrix

$kg\,m^2$	x	y	z
x	3.05	-7.25×10^{-5}	2.6×10^{-4}
y	-7.25×10^{-5}	3.12	-0.1
z	2.6×10^{-4}	-0.1	0.3

Table 5: Transmission and rotor head assembly estimated inertia matrix

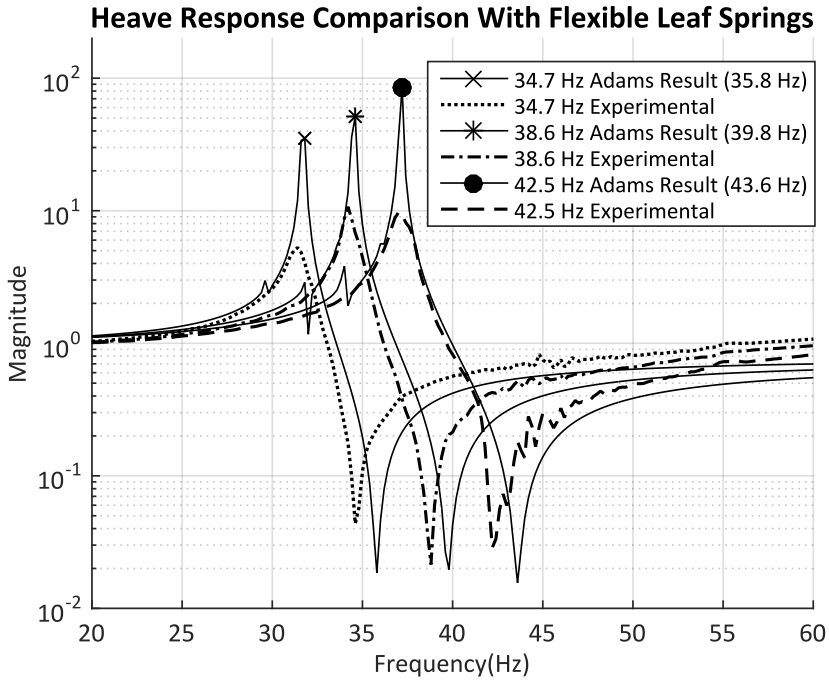

Figure 94: Heave response comparison between experimental results and ADAMS model with flexible leaf springs

frequencies and a 2.5% error on the 42.5Hz frequency.

These errors are very small, however, due to the extremely narrow bandwidth and rapid descent and rise over the antiresonance frequency a 1Hz error has a very large effect on the actual system performance. For example if the experimental results are not known and it is estimated to run the system at 35.8Hz as the ADAMS results suggest, the actual system will be achieving an attenuation of only 77% whereas the actual system antiresonance at 34.7Hz achieves an attenuation of 98%. Thus there would be a 21% loss in attenuation capability due to the 3% error on the antiresonance location estimation.

This shows that these systems are extremely sensitive to the excitation frequency, any small deviation from the actual antiresonance frequency results in massive reductions in system performance or even the possibility of running into the preceding resonance that may have very damaging results.

6.3.8 Study into the effect of modelling the pendulum arms as flexible bodies

The ADAMS model is further refined by creating flexible bodies of the pendulum arms, see Figure 77 Section 6.2.2.

Figure 95 shows the ADAMS results with the leaf springs and the pendulum arms as flexible bodies, the antiresonance frequencies for the three distinct frequencies are now approximately 1Hz lower than the tuned experimental results. This corresponds to a 3.2% error on the 34.7Hz frequency and a 2.6% error on both the 38.6Hz and 42.5Hz antiresonance frequencies.

Although this is not an improvement on error of the estimated antiresonance frequencies it has shifted the antiresonance approximations to be lower than the actual system instead of being higher as with only flexible springs, this is significant for the following reasons. The fact that the stiffness of the diaphragm plate, see Figure 65, has not been accounted for in the ADAMS model, suggests that accurate ADAMS results should yield antiresonance frequencies lower than the experimental results due to a slightly lower stiffness. This confirms that the system

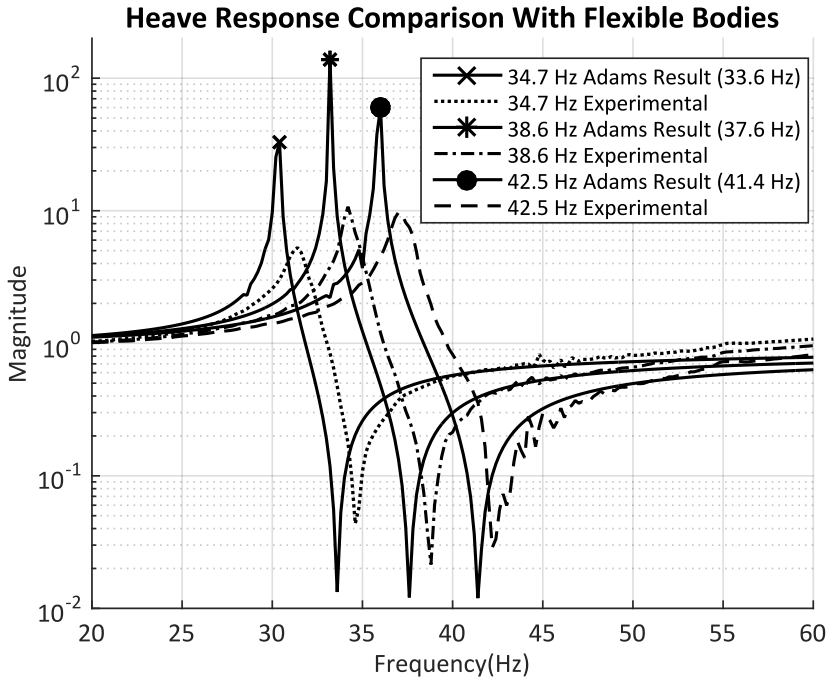

Figure 95: Heave response comparison between experimental results and ADAMS model with flexible pendulums and leaf springs

appears to be more realistic or accurate to what could be expected from the actual system, when also incorporating the pendulum arms as a flexible bodies.

There is significant change in the results between the ADAMS model with flexible leaf springs only and the system with both flexible leaf springs and pendulum arms. This suggests that modelling the components of the vibration isolation system with distributed stiffness and inertia models, like flexible bodies, improve the accuracy of the analysis.

6.3.9 Study of the effect of an additional concentrated stiffness in the ADAMS model

Figure 95 shows that the ADAMS model has resonance and antiresonance responses lower than the experimental results. Due to the fact that the mass is accurately measured and resembles the ADAMS model, leads to a conclusion that there is most likely a stiffness discrepancy. This is investigated by adding a distinct massless spring between the transmission and the fuselage to increase the overall stiffness. The added stiffness is increased until almost perfect correlation between the experimental and ADAMS results is achieved as shown in Figure 96.

It is speculated that the diaphragm is the cause of this stiffness discrepancy as its flexibility and contribution to overall stiffness is not modelled. It can be speculated that the massless spring added to the model can represent the stiffness characteristics of the diaphragm plate. However, because the diaphragm plate is made of two layers of fibre glass, it is very complex to create an accurate flexible body model, and therefore the diaphragm cannot be simulated with a degree of confidence within the scope of this dissertation. Thus the final and most accurate results obtained for the experimental and ADAMS model comparison is the ADAMS model with both flexible springs and pendulum arms as seen in Figure 95.

Based on the above speculations the stiffness value required by the added spring to align the experimental and

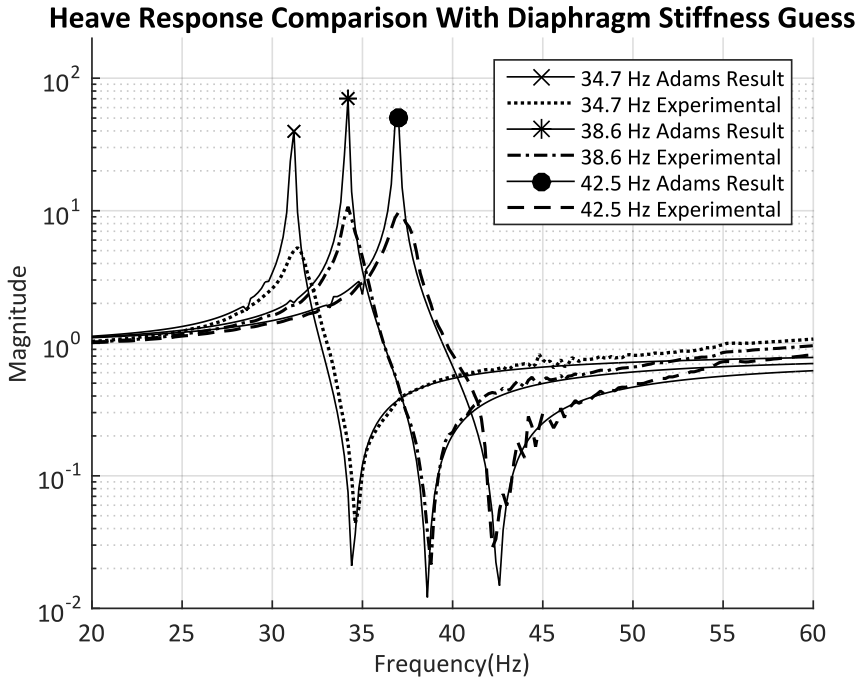

Figure 96: Heave response comparison between experimental results and ADAMS model with diaphragm stiffness guess

ADAMS results is the effective stiffness of the diaphragm plate itself. This stiffness is however not verified through experimental testing, so this is just a theoretical diaphragm stiffness value.

Figure 96 shows the ADAMS results compared to experimental for an estimated diaphragm stiffness of $6 \times 10^5 N/m$, if this estimate is correct it shows that the diaphragm stiffness is only about 6.5% of the overall system stiffness. This value seems very reasonable as the diaphragm plate was specifically designed to have very little vertical stiffness, but high lateral stiffness.

The figure clearly shows that the ADAMS model now almost perfectly correlates the experimental results. Usually the diaphragms of actual helicopters are made from steel plate and this stiffness can easily be incorporated by creating a flexible body of the diaphragm plate and including it in the ADAMS simulations.

6.3.10 Transmissibility Comparison and System Performance

Thus far only the results of the fuselage heave response was shown and compared, the transmissibility of the system defined as the acceleration of the fuselage over that of the transmission is the final comparison. This shows the amplification or attenuation of vibration through the system as a function of input vibration frequency. The transmissibility of the ADAMS model with flexible leaf springs and pendulum arms, excluding the estimated diaphragm stiffness, is compared to the experimental transmissibility results in Figure 97.

Figure 97 compares the transmissibility of the ADAMS model to the experimental results, exactly the same error on the antiresonance frequencies are seen as discussed with the fuselage heave response comparison of Figure 95. From this graph the performance of the system at each design frequency is obtained, there is a 0.5, 0.3 and 0.23% transmissibility at the 34.7, 38.6 and 42.5 Hz antiresonance frequencies respectively.

These results show the astonishing performance of an antiresonance vibration isolation system with equal or less than 0.5% of the vibration transmitted to the fuselage at the three design frequencies which is more than 99.5%

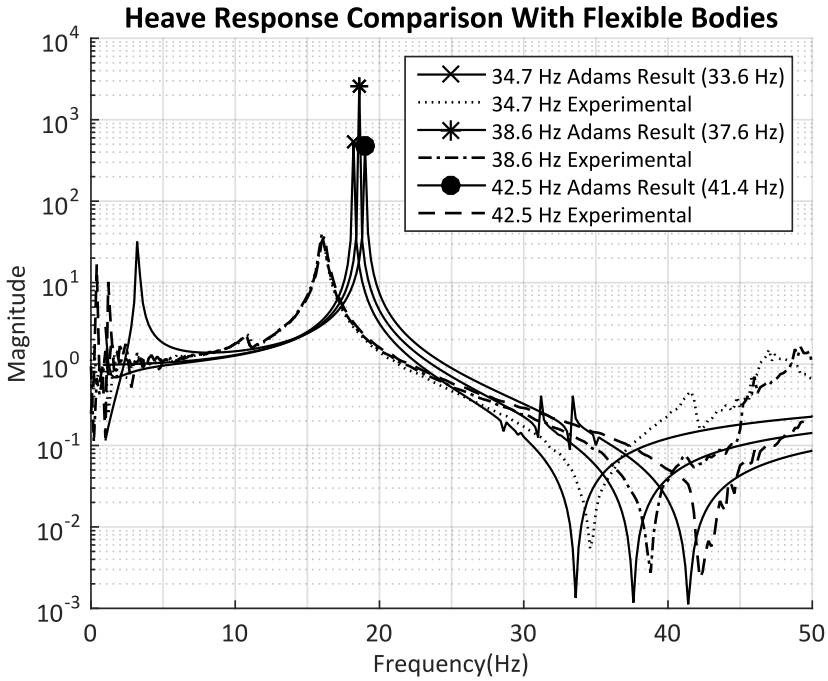

Figure 97: Transmissibility comparison of ADAMS and experimental results

vibration attenuation over the frequencies of operation. Although most commercial systems of this type will undoubtedly have elastomeric type bearings instead of actual roller bearings for reliability and robustness, which increases damping and reducing the effectiveness of the system, performances of up to 95% attenuation is easily obtainable and recorded in industry.

6.4 Visual confirmation

After reviewing the vibration data a method of visually confirming the effectiveness of the system is devised. Two small see-through containers are used, one is glued to the transmission and rotor head assembly and the other to the fuselage. Both are filled with coloured water so that disturbances to the fluid can easily be seen. At each design frequency the masses are adjusted to tune the system to the correct antiresonance frequency.

First the system is excited at $15 Hz$ where the Vibration Isolation System is inactive and represents a system as if there is no vibration isolator, then the system is excited at the antiresonance frequency. In both cases the excitation of the fluid can be seen and compared. Note the positions of the Pendulum Masses at each frequency, these are the same positions used for the three distinct frequencies when the vibration data was captured in Section 6.3 on page 71.

Figures 98 to 103 shows the vibration isolation system at each tuned frequency, first excited at $15 Hz$ and then at their respective tuned frequency.

From all the images the following conclusion is clear, at each tuned frequency when the system is excited at $15 Hz$ both the fluid on the transmission and the fuselage are visibly excited showing that the vibrations are transmitted to the fuselage from the transmission rotor head assembly.

In contrast when each system is excited at the antiresonance frequency for which it is tuned, the vibration in the transmission is clearly visible whilst the fluid on the fuselage shows almost no movement, this is visual confirmation that very little vibration is transmitted to the fuselage at the antiresonance frequency.

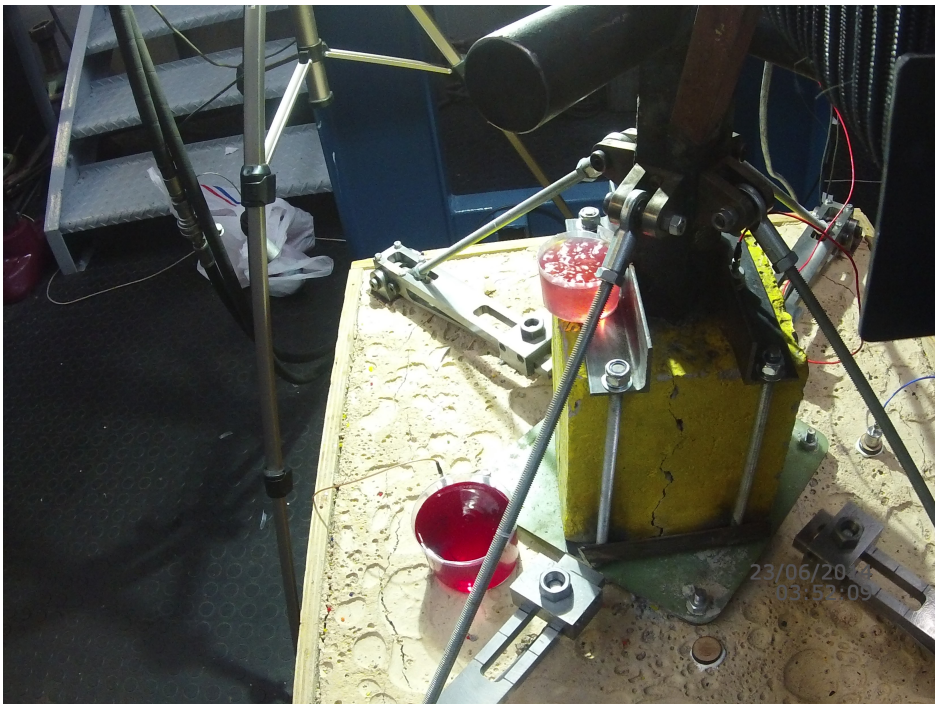

Figure 99: Tuned for 34.7 Hz antiresonance excited at 34.7 Hz

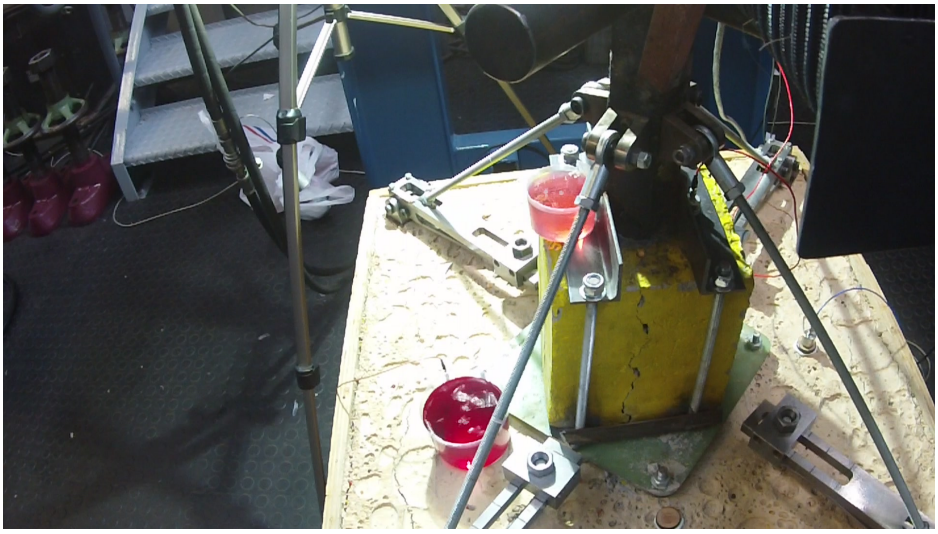

Figure 98: Tuned for 34.7 Hz antiresonance excited at 15 Hz

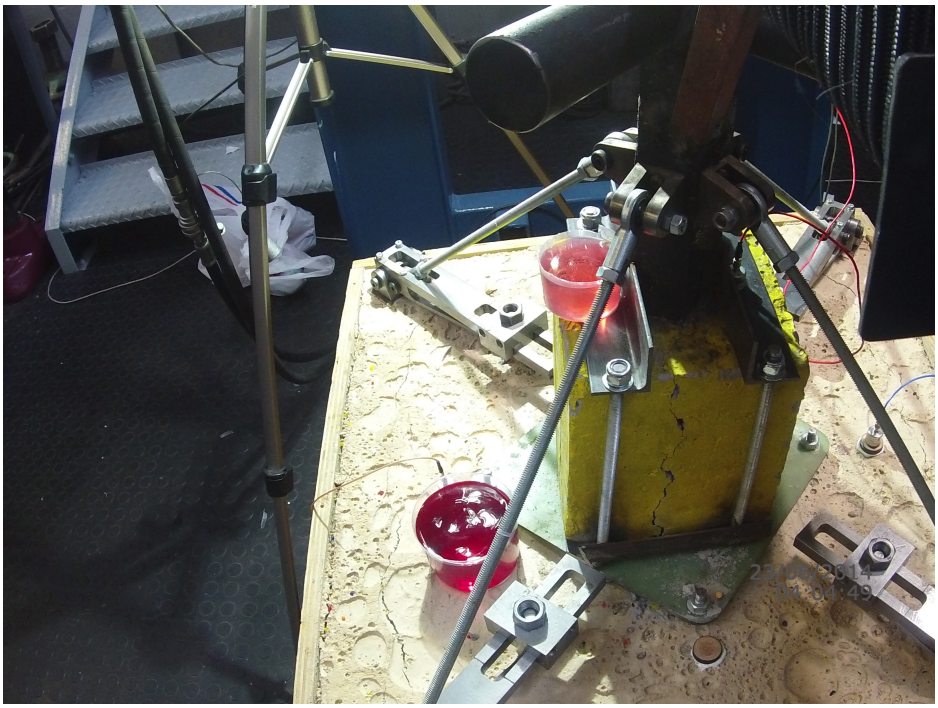

Figure 100: Tuned for 38.6 Hz antiresonance excited at 15 Hz

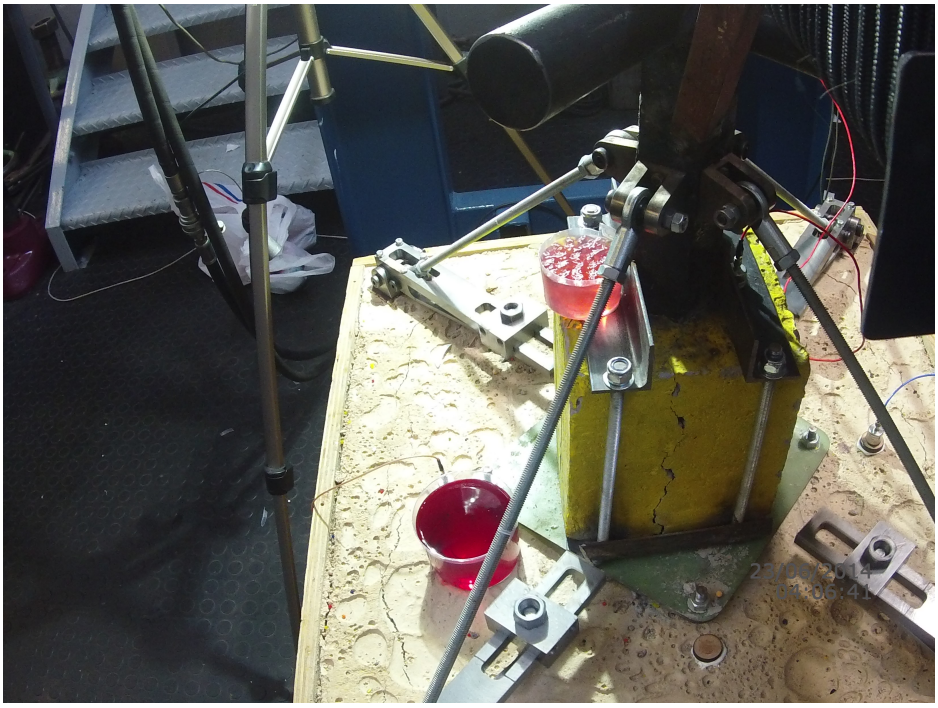

Figure 101: Tuned for 38.6 Hz antiresonance excited at 38.6 Hz

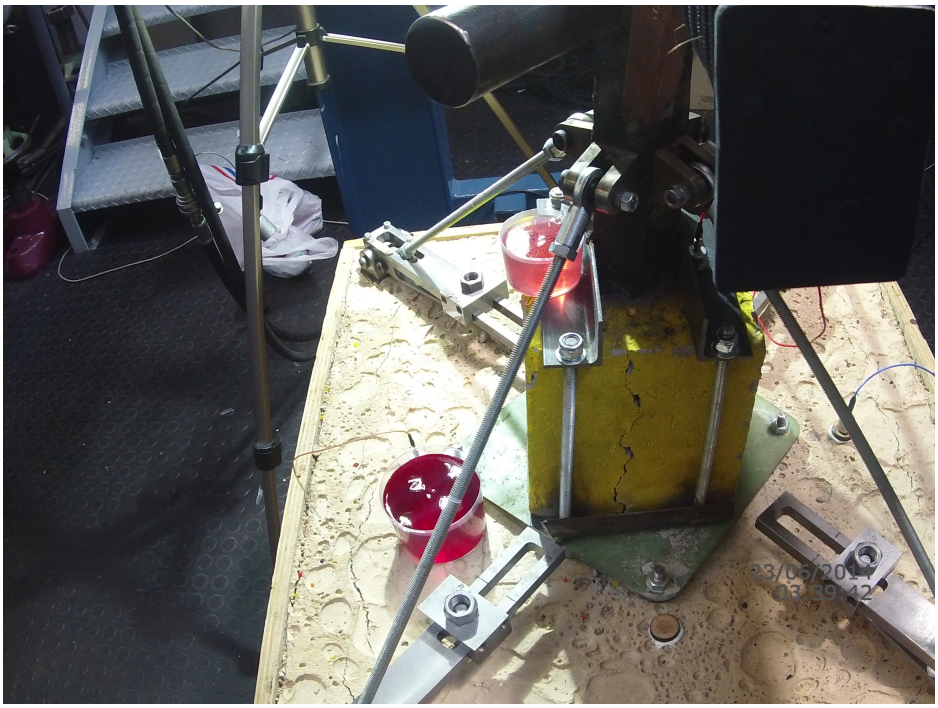

Figure 102: Tuned for 42.5 Hz antiresonance excited at 15 Hz

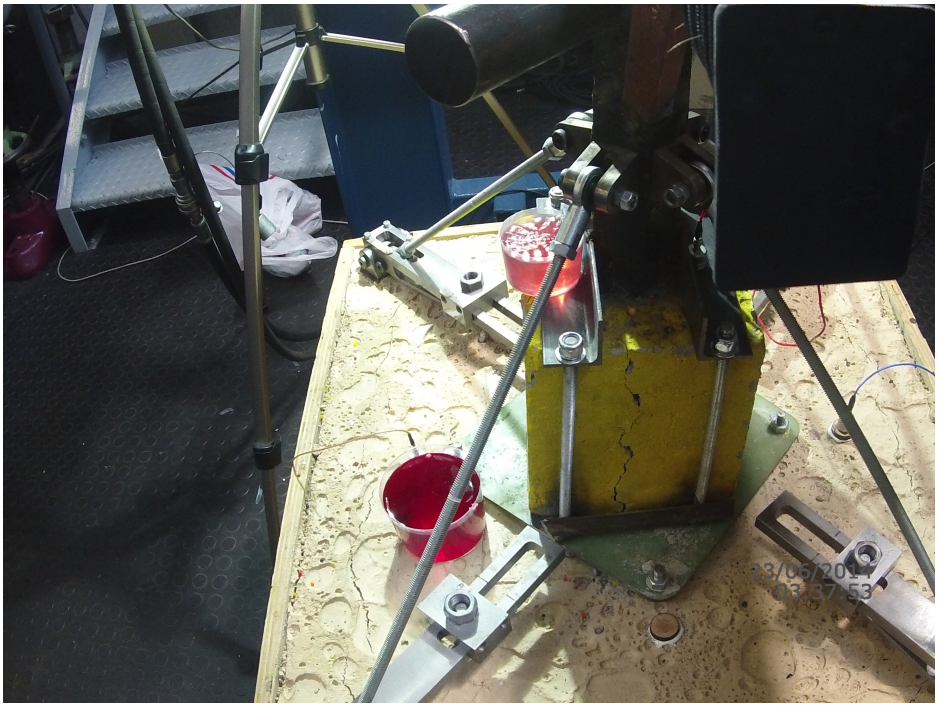

Figure 103: Tuned for 42.5 Hz antiresonance excited at 42.5 Hz

7 Conclusion and recommendations

From the experimental results there are quite a few conclusion to be made about the design, performance, pitfalls, advantages and use of a tunable antiresonance vibration isolation system.

Firstly and most importantly it is concluded that in-flight tunable antiresonance vibration isolator is most definitely achievable and has phenomenal performance.

A very interesting and undocumented characteristic of this type of system is its robustness and insensitivity to the discrepancies of individual sub-assemblies that make up the total antiresonance vibration isolation system. For example in this experiment one of the four vibration isolation systems had a stiffness 25% less than the other systems due to fabrication errors, by working with the overall system stiffness and then calculating a single mass and distance placement of said mass, used on all four sub-assemblies including the faulty assembly, the exact antiresonance frequency was still achieved, with the only side effects being strange resonance peak behaviour like the double resonance peak seen in this experiment.

Considering that these systems are designed to only be operated at the antiresonance frequency it can be argued that strange unaccounted behaviour around the resonance peaks are irrelevant as they are regions that are deliberately avoided in any case.

Following on the previous paragraphs, another robust feature of these systems is that each subsystem can be individually tuned, to the wanted antiresonance frequency, according to its own stiffness, mass and pendulum ratio and this will produce the same response as if all the subsystems were identical. In a nutshell fabrication accuracy for each subsystem is not critical as any discrepancies can easily be rectified by altering one of the system variables to retune any faulty subsystems.

The experimental to ADAMS result comparisons show that these systems can be accurately simulated with multi-body dynamic software, especially when using flexible bodies, with the simulation that had flexible bodies for the Pendulum Arms and the Leaf Springs obtaining results within 3.2% of the intended antiresonance. However, even with accurate approximations of the antiresonance frequency location, due to the extremely steep rise and fall of the antiresonance valleys, small errors in antiresonance locations will have massive performance degradations, with the mentioned 3.2% error resulting in a 21% drop in efficiency of the system if run at the estimated antiresonance frequency. Therefore, ADAMS can be used as a tool in the design of a VIS system, but the design of the system should always provide for a way of adjusting the tuning frequencies experimentally, as the predicted antiresonance frequencies will never be accurate enough to warrant the omission of an adjusting mechanism.

These systems can be both a blessing and a curse, a blessing in the absolutely unmatched vibration attenuation performance of more than 99.5% at all the design antiresonance frequencies, and a curse as they generate a resonance frequency in close proximity to this antiresonance frequency. The 34.7, 38.6 and 42.5 Hz antiresonance frequencies all have resonance peaks just 3.2, 4.6 and 5.4Hz before each of them respectively, this means that a mere 9, 11.8 or 12.7% speed reduction of the rotor in each case respectively will result in the system running into a resonance and possibly causing massive damage to the aircraft. It is therefore imperative that either fail safe systems are implemented or that the rotor speed is reliably controlled and maintained at all times.

The original prototype was intended to be tested for pitch, roll and heave performance, hence the fact that the dummy fuselage of the first prototype was full scale not only in mass but also in roll and pitch inertias. It is highly recommended that the first prototype be fixed and the roll and pitch performance experimentally tested and compared to the already created ADAMS model.

It is recommended to fundamentally come to an understanding of the friction damping stiffening phenomenon, as it is clearly visible in the experimental results but never truly understood, quantified or simulated. Understanding this phenomenon will lead to a much greater understanding of antiresonance vibration isolators. A study on the use of this friction stiffening phenomenon as a method of tuning the isolator is another interesting prospect.

A comparison between friction and normal damping and their effects on antiresonance vibration isolation systems is also a suggested study. Although this thesis proves the concept of using a shifting mass to tune a antiresonance vibration isolation system, designing and implementing an actual system that does this on the fly, with some mechanism can be a complete study in its own right.

References

[1] *Halwes, D.R., 1981. Total main rotor isolation system analysis, Bell Helicopter Textron, NASA Contractor Report No. 165667. Langley Research Center, Hampton, Virginia, June.*

[2] Jasbir Singh Arora. *Introduction to Optimum Design*. Academic Press, San Diego, second edition edition, 2004.

[3] Richard L. Bielawa. *Rotary Wing Structural Dynamics and Aeroelasticity (2nd Edition)*. American Institute of Aeronautics and Astronautics, 2006.

[4] D. BRAUN. Development of antiresonance force isolators for helicopter vibration reduction. *J Am Helicopter Soc*, pages 37--44, 1982.

[5] D. Braun. Vibration isolator particularly of the antiresonance force type, November 1 1988. US Patent 4,781,363.

[6] R.A. Desjardins, C.W. Ellis, and V. Sankewitsch. Vibration isolation system, May 9 1978. US Patent 4,088,042.

[7] R.A. Desjardins and V. Sankewitsch. Vibration isolation system, January 19 1982. US Patent 4,311,213.

[8] N.F. du Plooy, P.S. Heyns, and M.J. Brennan. The development of a tunable vibration absorbing isolator. *International Journal of Mechanical Sciences*, 47(7):983 -- 997, 2005.

[9] W.G. Flannely. The dynamic anti-resonant vibration isolator. In *22nd Annual AHS National Forum*, pages p. 152--158, Washington, 1966.

[10] W.G. Flannely. Dynamic antiresonant vibration isolator, May 30 1967. US Patent 3,322,379.

[11] W.G. Flannely. Three-dimensional vibration isolator, January 5 1971. US Patent 3,552,694.

[12] D.R. Halwes and W.A. Simmons. Vibration suppression system, December 2 1980. US Patent 4,236,607.

[13] R. C. Hibbeler. *Mechanics of Materials*. Prentice Hall, 7th edittion edition, 2008.

[14] D. J. Helicopter vibration isolation, November 5 1974. US Patent 3,845,917.

[15] Wayne Johnson. *Helicopter Theory*. Dover Publications, 1980.

[16] T. Lee, M.R. Smith, F.B. Stamps, and D.E. Heverly. Vibration isolation system, November 11 2014. US Patent 8,882,091.

[17] K. G. Lippert. Guidelines for the design of a passive vibration isolation system for helicopter rotors. Masters dissertation, University of Pretoria, 1988.

[18] V Sankewitsch. *Sankewitsch, V., 1981. Total main rotor isolation system analysis, Boeing Vertol Company, NASA Contractor Report No. 165667. Langley Research Center, Hampton, Virginia, June.*, 1981.

[19] M.R. Smith and F.B. Stamps. Vibration isolation system, January 6 1998. US Patent 5,704,596.

Figure 104: First Dummy Fuselage Modal Analysis

A Additional information on the first prototype

This appendix has a more detailed look at the design, fabrication and other analysis of the first prototype that was not used in the final experiment, it initially was speculated that the dynamics of the first fuselage had adverse influences in the test frequency range of interest.

However discoveries whilst testing the second prototype indicate that the first fuselage might actually have worked if the same changes that were made during the testing of the second prototype, to get working results, might have fixed the problem. There was unfortunately no resources or time to retest the first dummy fuselage after the excitation had been moved to the centre of the transmission and the pendulum hinges had roller bearings inserted.

A.1 Design of first prototype fuselage

The design of the first prototype is more or less as described in Section 5.2.1, however, some analysis that where not reported on is the FEA analysis to check for resonance frequencies near the test frequency range of interest. Figure 104 indicates that there is a $37Hz$ mode of vibration that is close to the test frequency range, prompting the addition of struts as shown Figure 105 to ensure that this resonance frequency is shifted away from the test frequency range. Figure 105 shows a $25Hz$ mode which is lower than the frequency range of interest.

A.2 Detailed fabrication of first prototype

First the casting boxes where machined with a CNC router see Figure 106 and assembled as seen in Figure 107, note the slots are machined for the I-beams to locate said beams in the centre of the concrete block.

Using 3D CAD models of the dummy fuselage as reference the fuselage frame was cut from I-beam sections and welded together as seen in Figure 108.

The concrete casting boxes are slid onto the ends of the I-beams and slotted into I-beam cut grooves pre-machined at the back panel of every box as seen in Figure 109, also note that weld beads are welded to the I-beams to ensure that the concrete cannot break loose from the bare smooth metal.

The bottom concrete block is originally separate from the fuselage frame and cast with its own I-beam. Figure 110 shows the blocks after the concrete has been cast and allowed to set. An electric jack-hammer drill, set to hammer

Figure 105: First dummy fuselage modal analysis after strut

Figure 106: Routing of fuselage casting boxes using CNC router

Figure 107: Assembled casting boxes

Figure 108: First dummy fuselage frame

Figure 109: Casting box on I-beams

only, is used to vibrate the boxes when the concrete was cast to ensure that air bubbles are removed from the block and a dense solid block is formed.

Finally the bottom concrete block is lifted using an engine crane, and then welded to the fuselage frame as shown in Figure 111.

Design and fabrication of the transmission-rotor assembly is well documented in Section 5.3.1, as the first prototype transmission-rotor assembly was simply modified to create the second. Both prototypes share the vibration isolation system so its design and fabrication is not repeated here.

A hole template is cut with a laser cutter to ensure correct placement of the hinge mounting holes, see Figure 112.

Beams with studs to attach the tips of the leaf springs are welded into the frame, and the frame and concrete blocks are painted as seen in Figure 113. The transmission-rotor assembly and the vibration isolation system is assembled and bolted to the fuselage frame with the final results as shown in Figure 114.

A.3 Experimental trials

The following experimental trials where experienced during testing of the first prototype.

A.3.1 Initial tests

Figure 115 shows the initial test result with a large resonance peak in the middle of the test frequency range, it is assumed that dynamics from the dummy fuselage is to blame, an experimental modal analysis at the resonance shown is done with a single accelerometer being moved from point to point whilst recording magnitude and phase data of said points.

Figure 110: Cast concrete fuselage blocks

The data is compiled in Matlab and shown in Figure 116, with the undeformed shape and the mode shape deflection shown over it. From the figure it is seen that the forward facing beam is flexing due to the concrete blocks pivoting more or less around their centres. This lead to the assumption that the fuselage was not stiff enough and this mode of vibration was dominating the response of the vibration isolator.

A.3.2 Stiffening the dummy fuselage

A multitude of attempts to stiffen the fuselage, specifically the front and rear concrete block with respect to the fuselage, lead to slight improvements as can be seen in Figures 117 to 119 as the resonance frequency moves away from the test frequency range. Drastic measured are applied in a last ditch attempt to stiffen the fuselage by welding an entire lattice box frame around the fuselage as seen in Figure 120, which finally removes the resonance from the test frequency range, however, the response shows sporadic antiresonance behaviour at almost double the designed theoretical frequency, indicating that something is causing the system to behave excessively more stiff than expected.

A.3.3 Inadequate shaker

After much debate and testing it was finally realised that the original $100N$ shaker of the first experimental setup cannot overcome the friction in the pin joints of the pendulum arm, and the dynamics seen in Figure 120 are from the friction locked pendulum arm which will considerably increase the overall system stiffness.

It is calculated that for well lubricated pins the required force to overcome the pin friction is $240N$ and if the pins have no lubrication this becomes $752.1N$, clearly the $100N$ shaker will not suffice and experimental frame is redesigned and the electromagnetic shaker replaced with a hydraulic shaker as seen in Figure 121.

Figure 111: Welding of bottom fuselage block

Figure 112: Hinge template

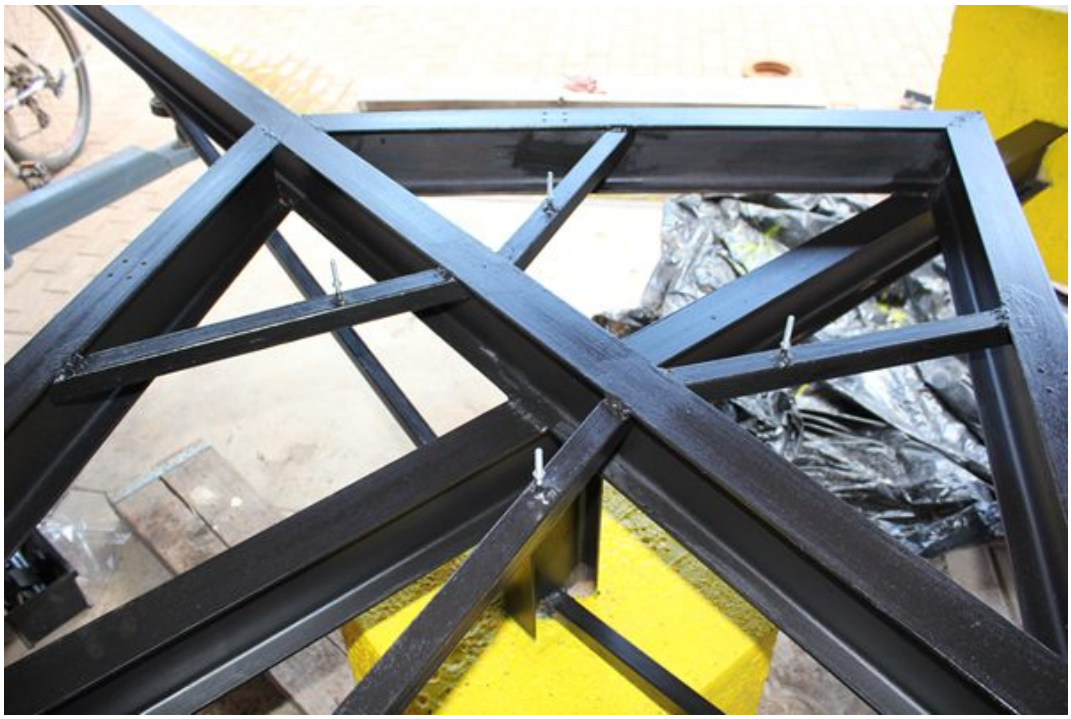

Figure 113: Leaf spring struts and painted dummy fuselage

Figure 114: Final first prototype assembly

When the experiment is run with the more powerful hydraulic shaker, the friction lock hypothesis is confirmed and the antiresonance frequencies of the fastest and slowest end states of the vibration isolator are at least within the theoretic range of the fastest and slowest antiresonances, however, they do not match the predicted slowest and fastest antiresonance frequencies as seen in Figure 122.

A.3.4 Suspected adverse effects of dummy fuselage dynamics

The system is tested in small increments of shifting the tuning mass over its whole range whilst capturing the frequency response function of the fuselage, see Figure 123, firstly the expected shape of the response did not match what is predicted for the fuselage response function, with a resonance after the antiresonance instead of before it, secondly shifting the tuning mass over the entire range did not show any considerable shift in antiresonance. This led to speculation that the dynamics of the the fuselage might still have adverse effects over the testing frequency range, it is at this point where it is decided to create the second prototype fuselage, consisting of only a solid block that rules out any structural dynamic problems while sacrificing the rotational inertia being scaled to the actual helicopter.

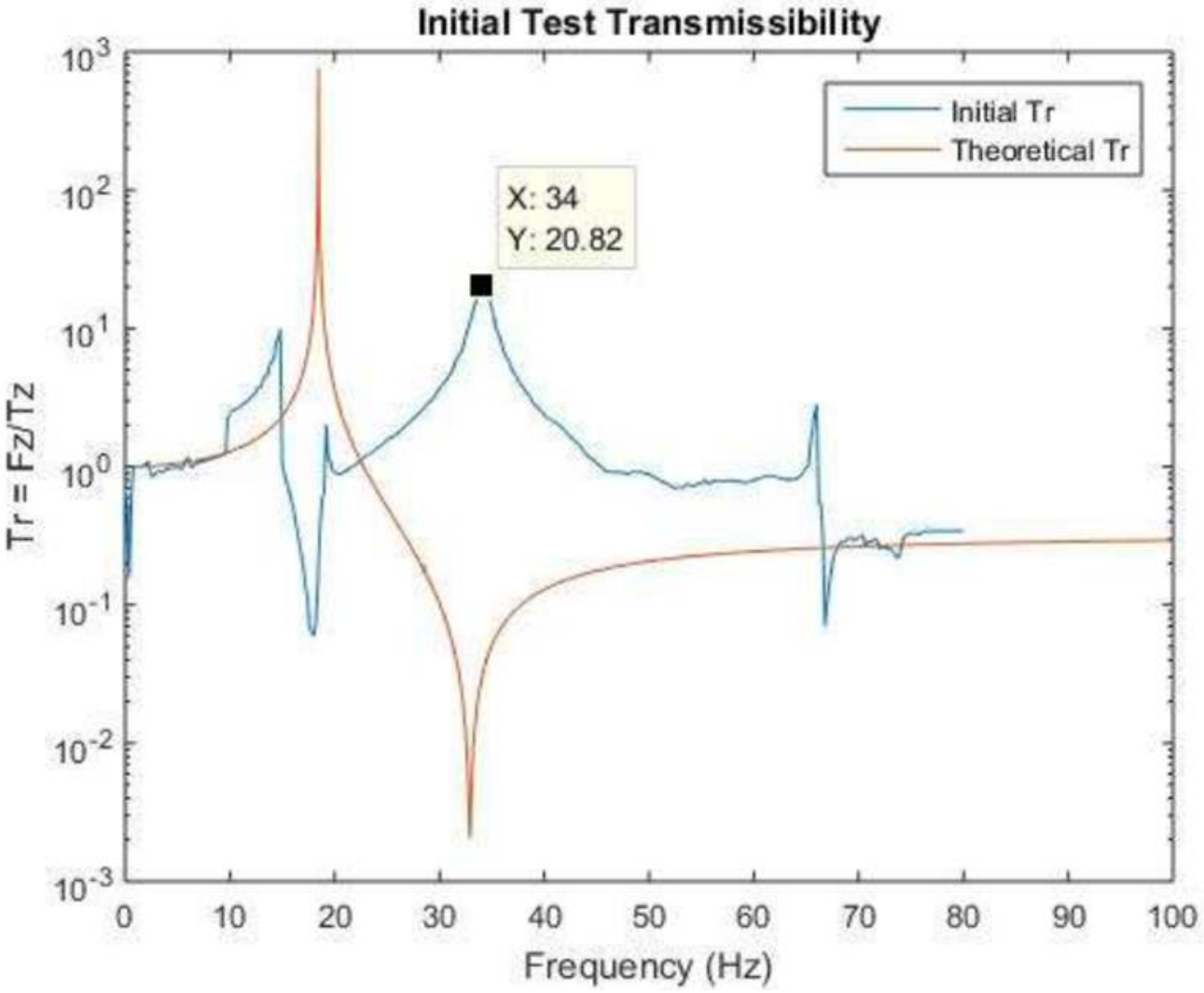

Figure 115: Initial test results

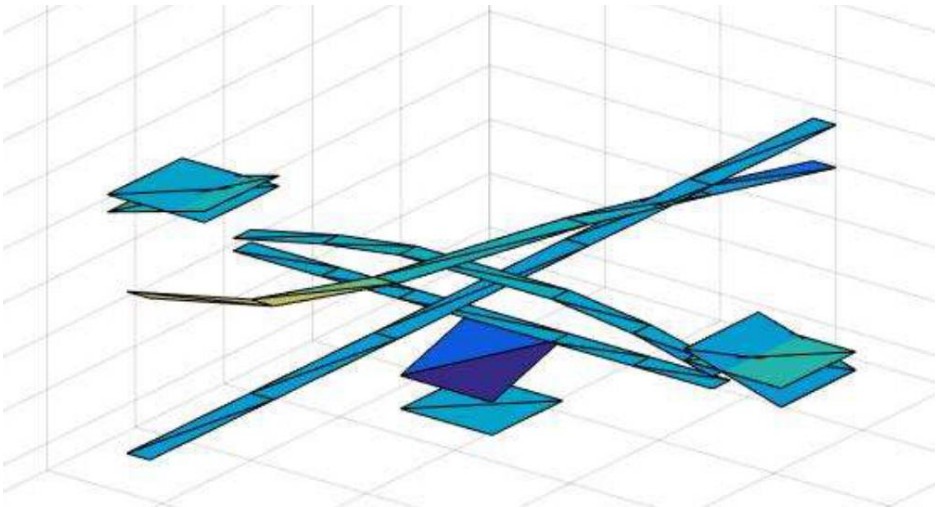

Figure 116: Experimental mode shape determination

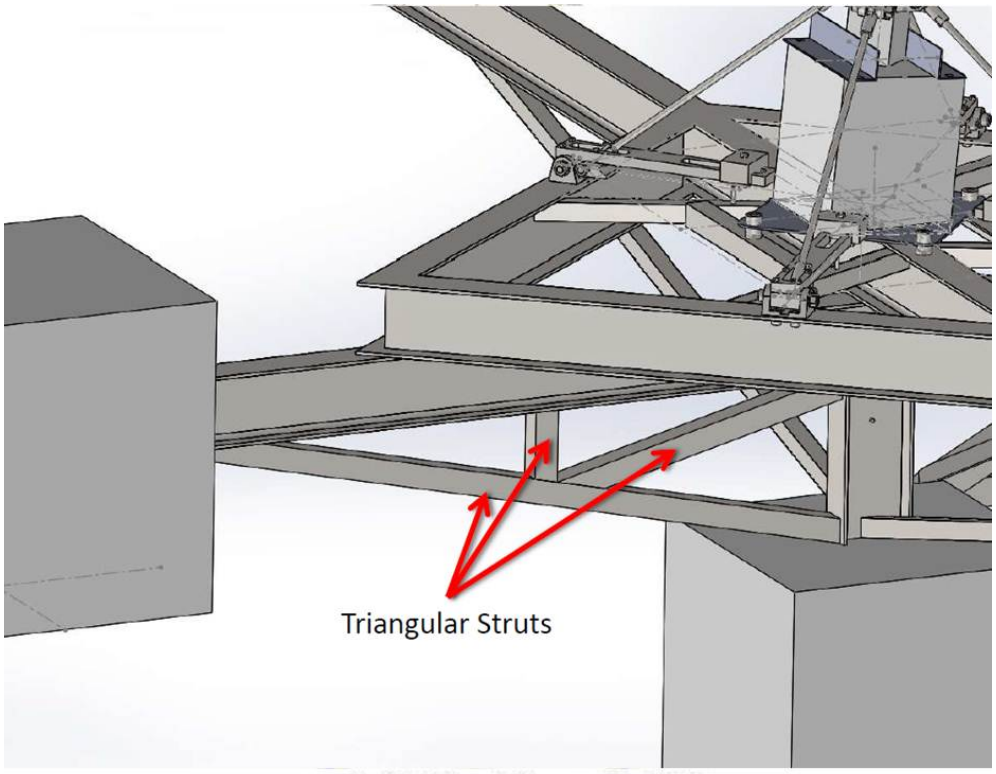

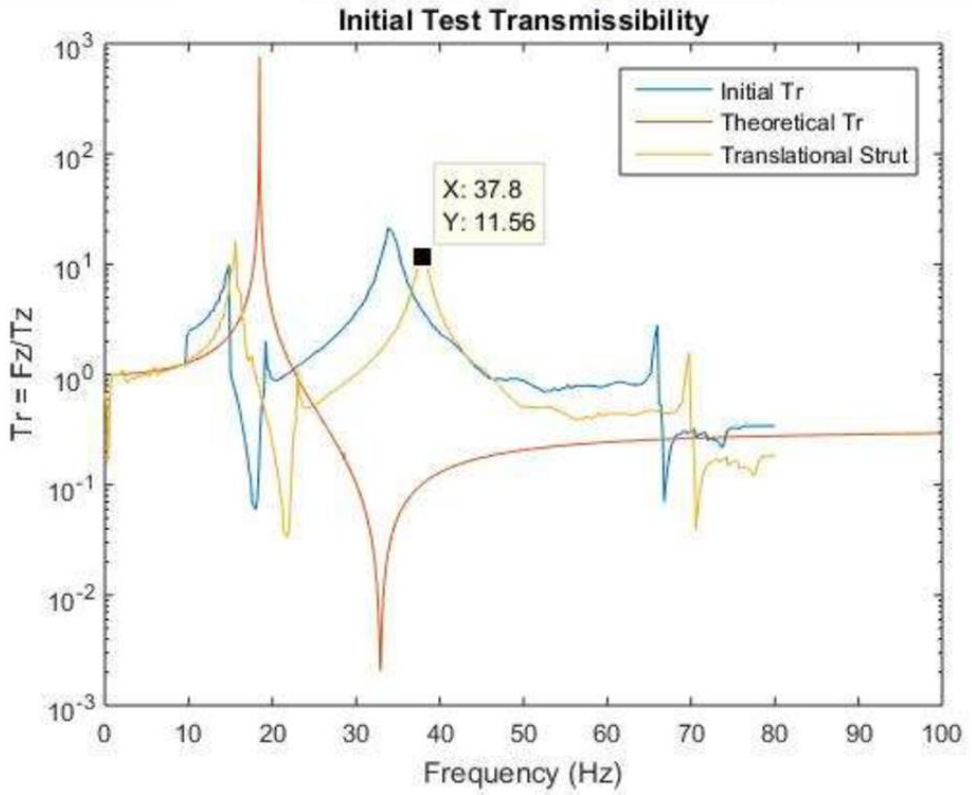

Figure 117: Triangular strut to try and stop translation from concrete blocks in the z-direction

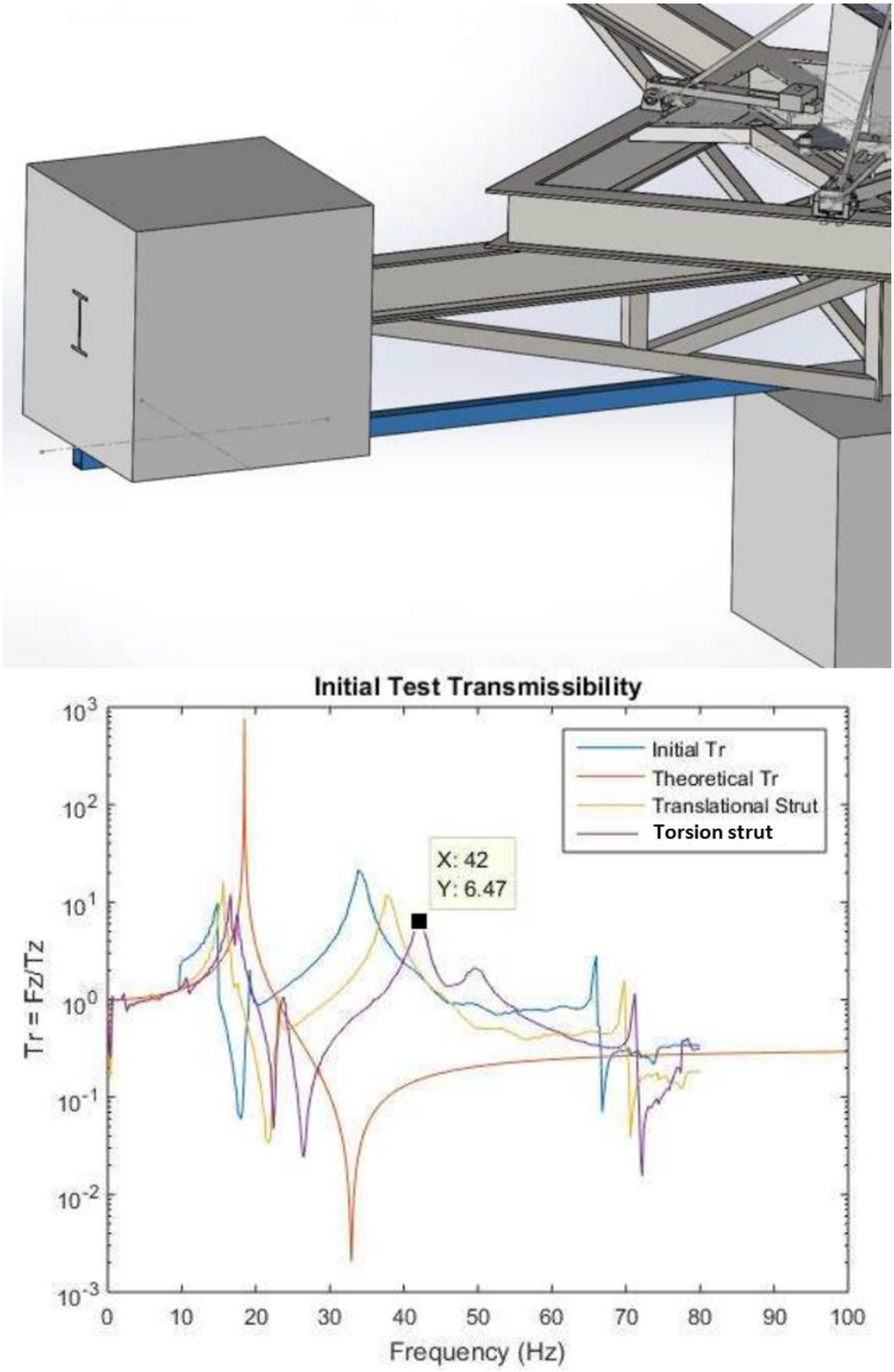

Figure 118: Torsional strut

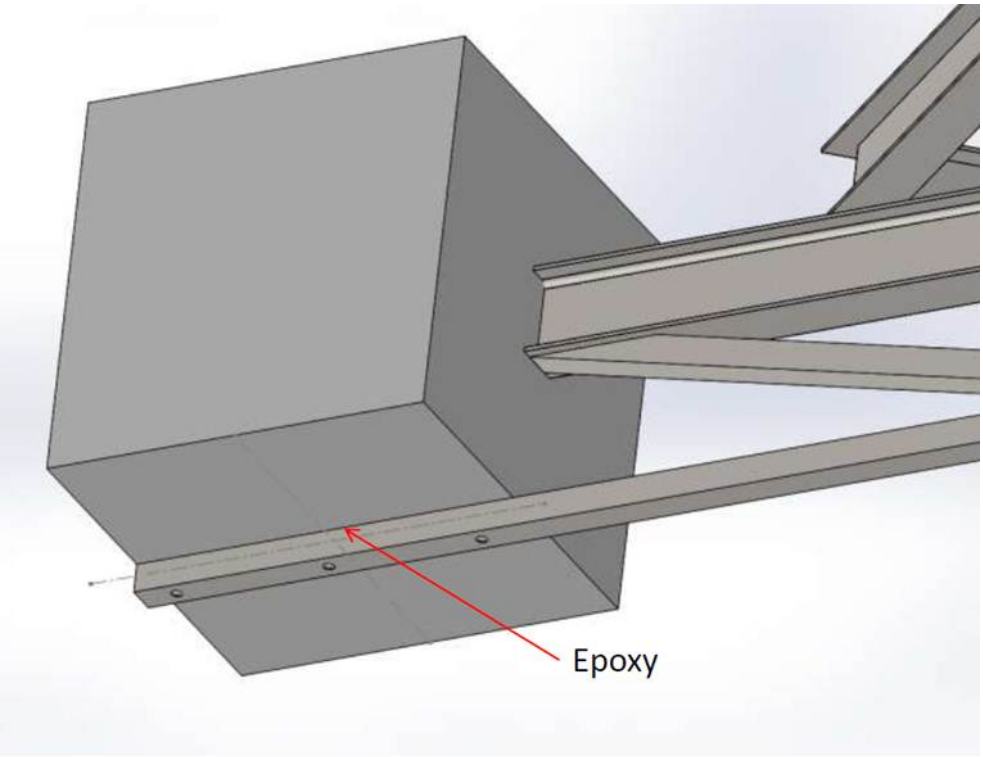

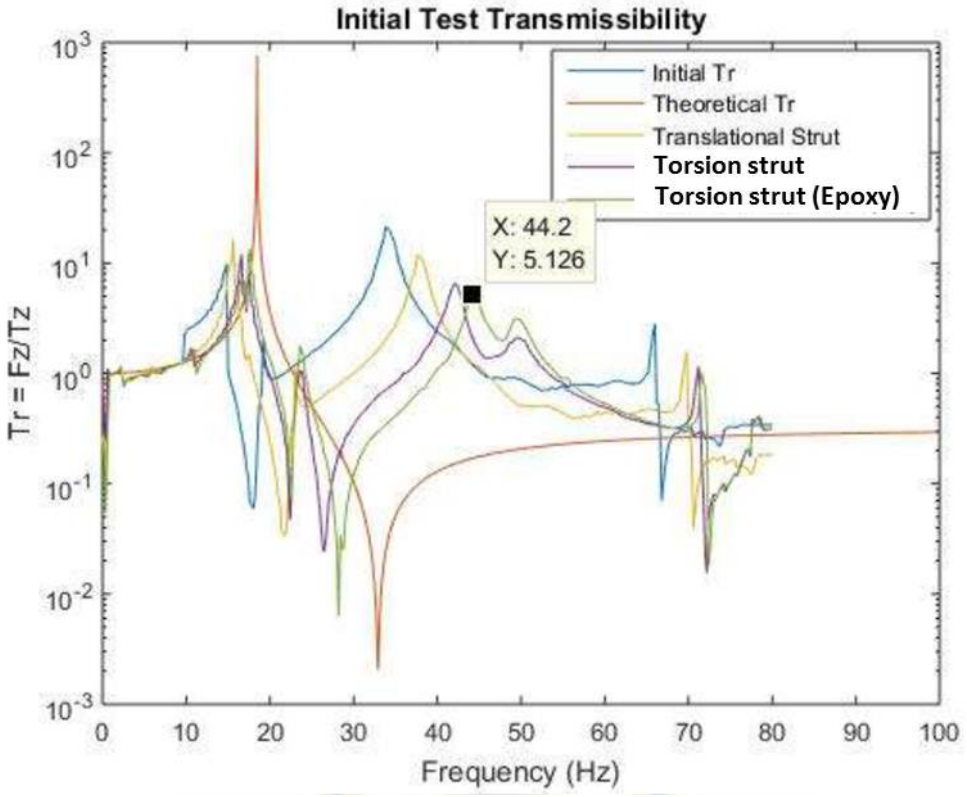

Figure 119: Torsional strut with epoxy

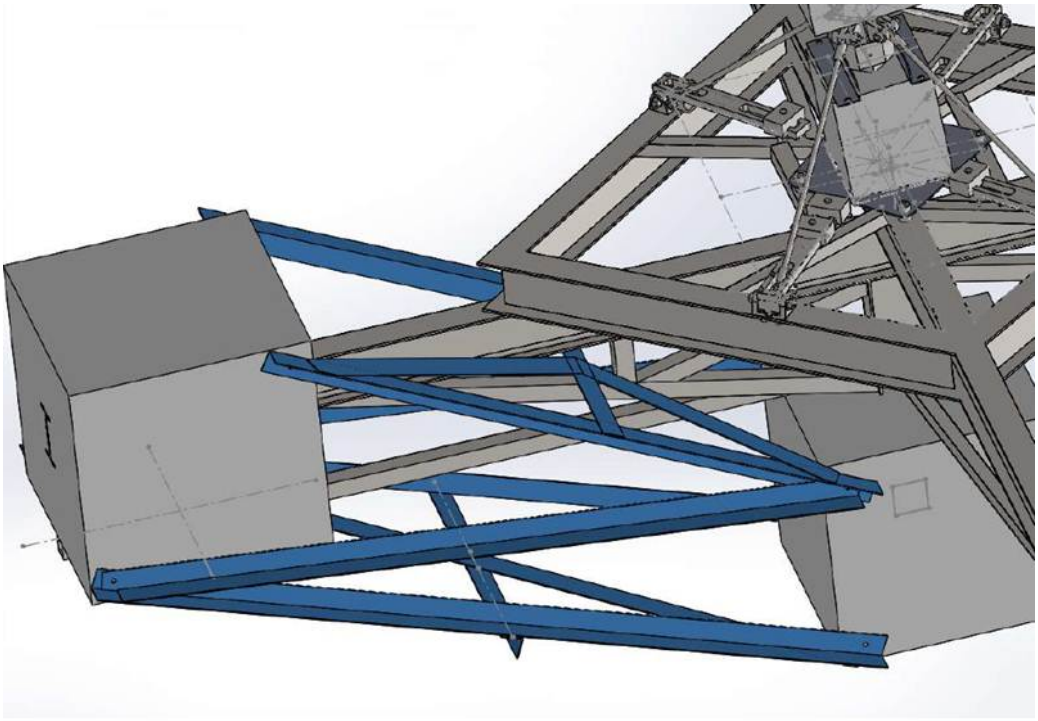

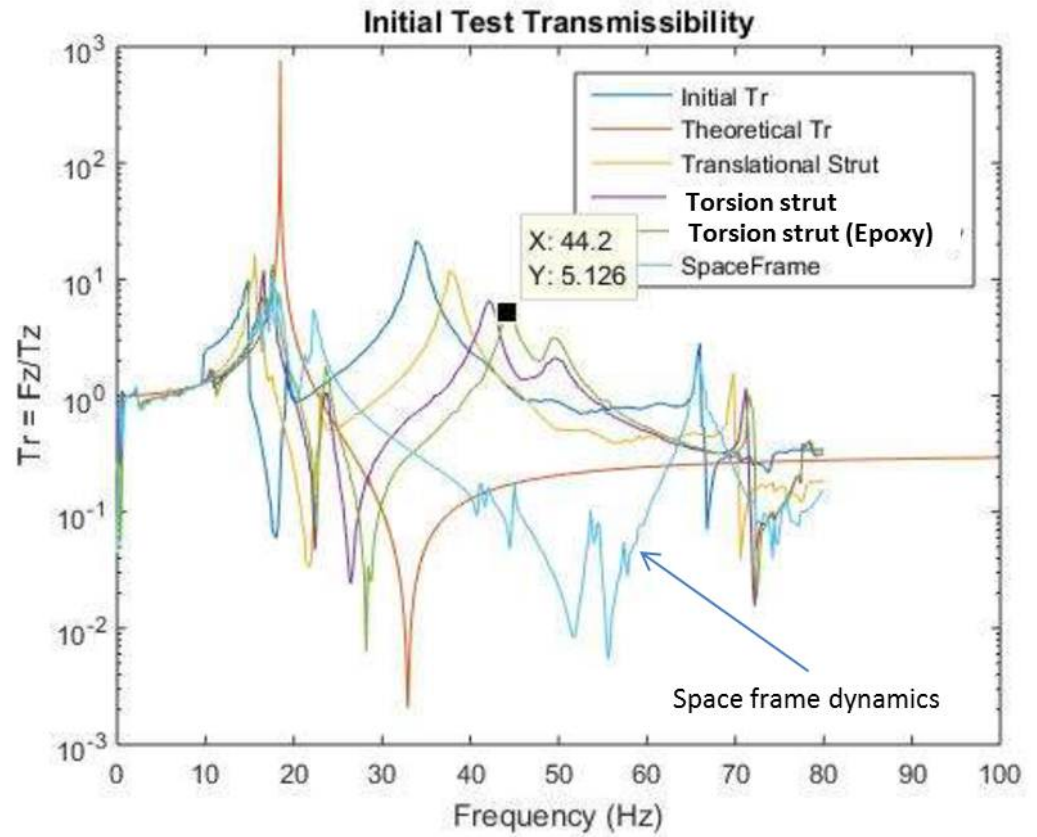

Figure 120: Lattice box frame

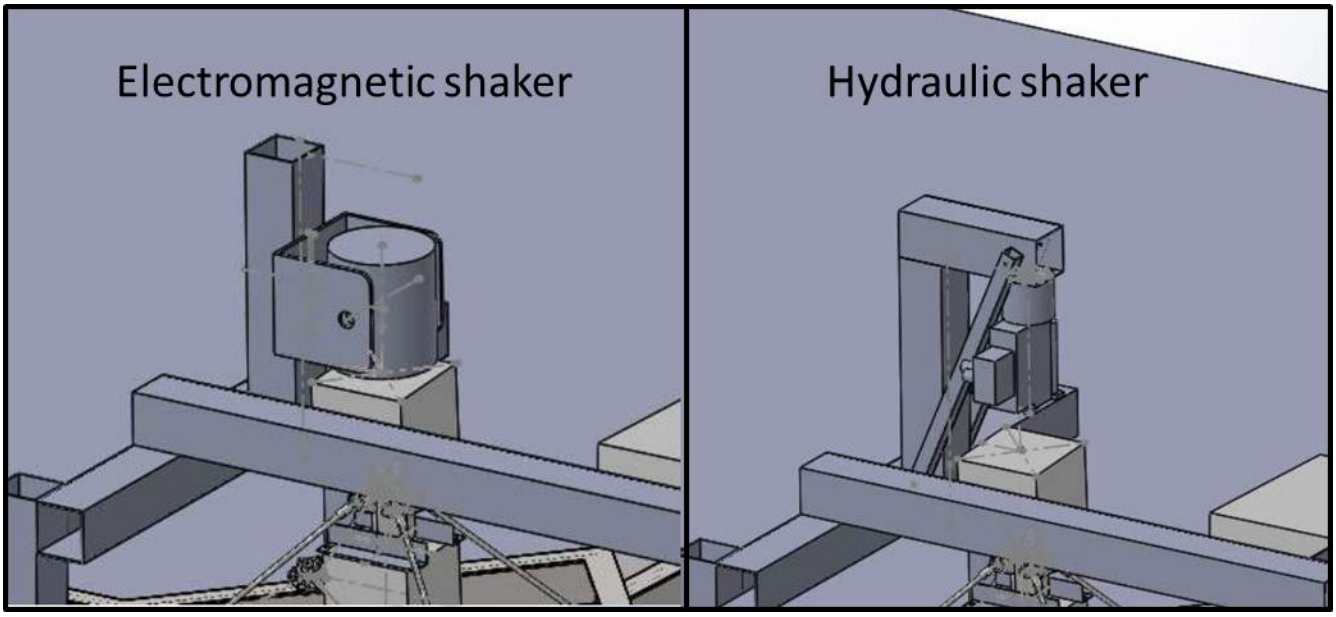

Figure 121: Hydraulic shaker

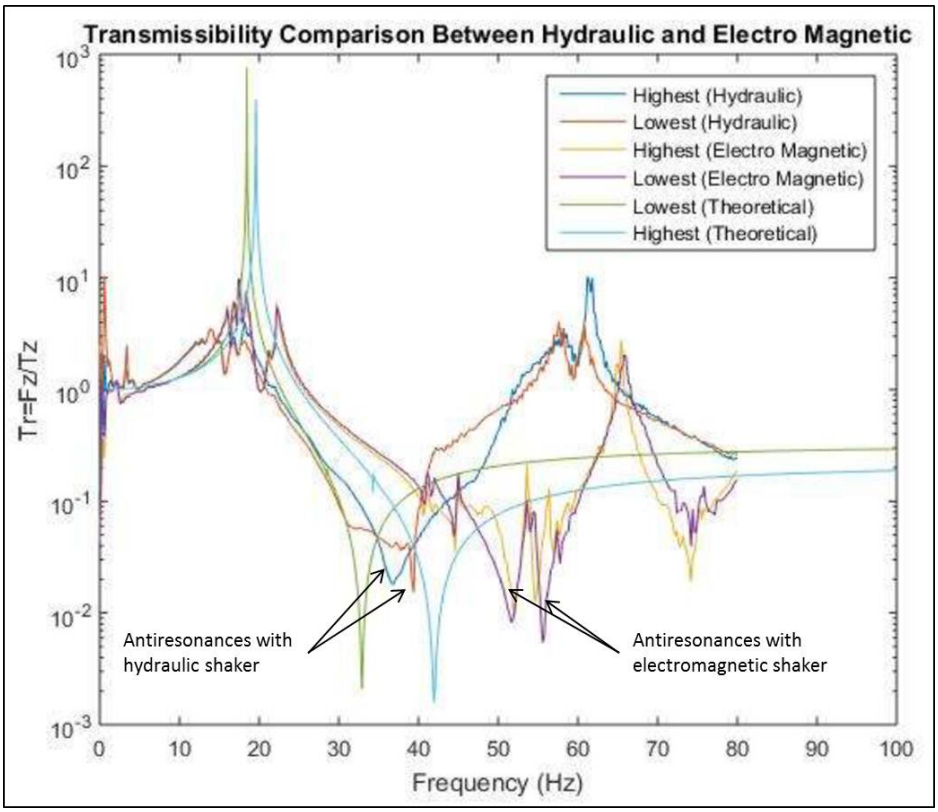

Figure 122: Hydraulic vs Electromagnetic

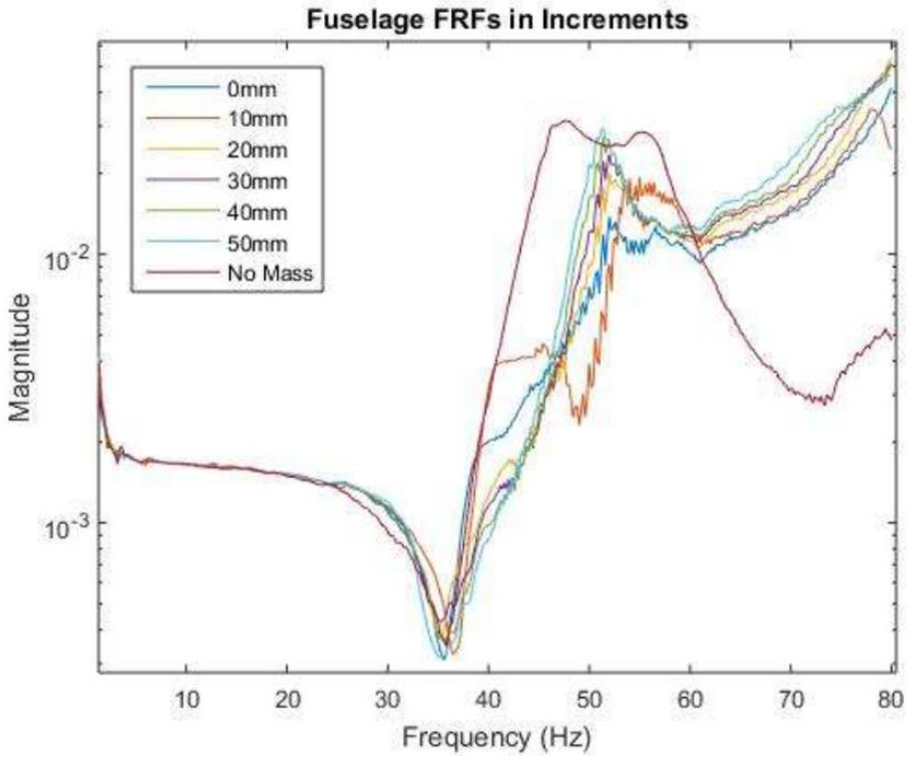

Figure 123: No antiresonance shift